Development of Novel Optical Instrumentations and Algorithms for Early Cancer Detection

by

Haoran Zhang

Department of Biomedical Engineering
Duke University

Date:_____

Approved:

_____
Adam Wax, Supervisor

_____
Ying Wu

_____
Roarke W. Horstmeyer

_____
Junjie Yao

_____
Nicholas Shaheen

Dissertation submitted in partial fulfillment of
the requirements for the degree of Doctor
of Philosophy in the Department of
Biomedical Engineering in the Graduate School
of Duke University

2023

ABSTRACT

Development of Novel Optical Instrumentations and Algorithms for Early Cancer Detection

by

Haoran Zhang

Department of Biomedical Engineering
Duke University

Date:_____

Approved:

_____
Adam Wax, Supervisor

_____
Ying Wu

_____
Roarke W. Horstmeyer

_____
Junjie Yao

_____
Nicholas Shaheen

An abstract of a dissertation submitted in partial fulfillment of the requirements for the degree of Doctor of Philosophy in the Department of Biomedical Engineering in the Graduate School of Duke University

2023

Abstract

Esophageal cancer is a very aggressive form of cancer, and in the past decade, the incidence rate of esophageal cancer is rising faster than any other malignancy in the U.S. Luckily, most precancers are preventable given timely surveillance and proper treatments. Despite the recent success of current screening methodologies, these techniques are still costly and limited. As an alternative, angle-resolved low-coherence interferometry (a/LCI) is an optical technique which enables depth-resolved measurements of nuclear morphology, a biomarker for precancer.

In this dissertation, several advances in a/LCI technology are presented. First, computational analysis of a previous clinical a/LCI dataset is used to provide design guidance for future a/LCI designs. The impact of reductions in angular range and angular sampling frequency on the diagnostic performance of a/LCI is analyzed and discussed. Next, in order to improve the clinical utility of a/LCI, a novel processing algorithm based on deep learning is presented for identifying dysplasia from depth-resolved angular scattering scans collected by a/LCI with high accuracy and speed. Future development of this algorithm may open to possibilities for real-time clinical analysis of a/LCI data, and improve the clinical utility of the instrument during in vivo clinical trials for real-time screening of the tissue.

In addition, instrumentational advances in a/LCI are also demonstrated. Development of the opto-mechanical instrumentation using a single multimode fiber is presented to overcome the limiting factor of using fiber bundles for a/LCI imaging, as

these fiber bundles are fragile, expensive, and exhibit low optical throughput. The technique is validated using microsphere phantoms, and showed excellent agreement with the actual size. This technique is also insensitive to the displacement of the fiber, and shows great potential for future endoscopic applications for medical diagnostics.

Finally, a combined a/LCI and OCT imaging platform is developed and adapted for esophageal imaging, and a clinical study is performed to determine the effectiveness of using this combined instrumentation for screening dysplasia in patients with Barrett's esophagus, a biomarker for dysplasia. Optical biopsies are taken from 50 distinct tissue biopsy sites and compared to histopathological analysis of co-registered tissue biopsies. Analysis of the a/LCI scans demonstrates perfect sensitivity (100%) for detection of esophageal dysplasia, and the increase in specificity (from 84% to 93%) compared with a previous clinical study demonstrates the ability of OCT for targeting potential diseased biopsies, suggesting that optical biopsy characterization using a/LCI nuclear morphology measurements with real-time OCT imaging guidance will aid the clinician in identifying dysplastic tissue sites in vivo, leading to improved screening protocols, and ultimately, better patient outcomes.

Dedication

For Mom, Dad, and my wife, who have given me more support than I can express.

Contents

List of Tables

List of Figures

Acknowledgements

Words cannot express my gratitude to the countless amount of people in my life who have helped, supported and encouraged me through my dissertation research. In particular, I owe an immense debt of gratitude to my Ph.D. advisor, Dr. Adam Wax for his guidance and mentorship through my graduate research. His dedication to his students is remarkable, and I am truly thankful for his exceptional support and mentorship. I would also like to thank the members of my committee who have guided and inspired me throughout this journey.

I also want to thank the BIOS lab staff and my fellow Ph.D. students for their friendship and help throughout my research projects, including Dr. Ken Chu, Dr. Sanghoon Kim, Dr. Yang Zhao, Dr. Hansang Park, Dr. Will Eldridge, Dr. Silvia Ceballos, Dr. Zach Steelman, Dr. Owen Sun, Dr. Ge Song, Dr. Evan Jelly, Dr. Wesley Kendall, Cindy Chen, Hillel Price, George Funkenbusch.

Finally, I would like to extend my love and thanks to my family, my parents, Hong Zhang and Haiying Zhang, and my wife, Yinyao Ji, for their constant love and support. None of this would have been possible without you all.

1 Introduction

1.1 Motivation

Esophageal adenocarcinoma (EAC) is a very aggressive form of cancer with 604,000 new cases and 544,000 deaths worldwide, the latter signifying that esophageal cancer is responsible for one in every 18 cancer deaths in 2020 [1]. The incidence rate of EAC has increased dramatically in the past few decades, rising faster than any other malignancy in the U.S [2]. Although a lot of clinical treatments were introduced to mitigate this situation, the 5-year mortality rate for EAC still remains 78% [3]. The current standard sampling method recommended for surveillance, also known as Seattle protocol, is naturally prone to sampling error [4], and the problematic surveillance procedure requires significant time and resources to prepare and analyze the screening and diagnostic process, which results in low adherence to the protocol in practice [5-8]. Clearly, effective endoscopic surveillance techniques are sorely needed for preventing EAC at a precancerous stage.

This need has inspired the development of several optical techniques for early detection of precancer by detecting biochemical and structural changes in the tissue [9-18]. Optical techniques are well suited for this task because optical penetration depths usually fall in the range of 0.5 to 1.0 mm, which contains the basal layer of the epithelium, where most cancer originates [19]. As an alternative to taking biopsies, infrared and near-infrared optical techniques are also non-ionizing, non-invasive, low-risk, and can provide cellular-scale spatial resolution [20].

One potential solution for precancer detection is angle-resolved low-coherence interferometry, or a/LCI. a/LCI is a non-invasive optical modality that measures angle dependent, depth-gated light scattering from tissue samples [13, 21, 22]. this light scattering profile can be analyzed to detect nuclear enlargement at the basal layer of the epithelium, which serves as a biomarker for precancer detection [23-26].

a/LCI has proven to be quite successful in early clinical trials [23-25, 27, 28], but there remain limitations that hinder the extension of the clinical viability of a/LCI. An algorithmic problem related to a/LCI is the long computational time of the inverse light scattering analysis (ILSA) algorithm for extracting nuclear morphology [26, 29]. Other methods have also been introduced to improve a/LCI processing, including continuous wavelet transform [30] and T-matrix [31] approach, but both suffer from substantial trade-offs in terms of processing accuracy and speed. Ideally, processing time should be under 1s in order to provide instant feedback to clinicians and reduce the total time of an imaging session. Also, designs of a/LCI instrumentation often are developed to compress the scattering function either by reducing angular range for better scanning ability or reducing angular sampling frequency for better SNR [26, 27]. But the diagnostic impact of these changes is unknown, presenting a significant constraint to the technological development.

Other instrumentation related limitations also present a hurdle for this technology. In most clinical a/LCI instrumentation, the critical component is the fiber bundle, or the coherent imaging bundle. It is an essential component for providing the

multiple discrete channels for transmitting the angular-scattered field to the optical engine for detection [27]. Unfortunately, commercial bundles suitable for this purpose are often not readily available, as common bundles may be fragile, multimodal, noisy, and expensive, resulting in loses in performance [32-35].

A final problem lies in the nature of this technology. a/LCI is not an imaging modality, which means that it can only detect light scattering signals but cannot provide visual guidance of the tissue. Lacking this information may result in low-quality scans. Alternatively, endoscopic optical coherence tomography (OCT) has proven effective at providing real-time cross-sectional images and identifying metaplastic changes within the epithelium tissue, but it is poor at detecting dysplasia.

To address these concerns, this dissertation presents novel a/LCI processing algorithms and instrumentations approaches. First, we analyze how various parameters influence the diagnostic impact of a/LCI and propose next generation probe designs [36]. Further, we propose a deep-learning-based algorithm as a new processing method for dysplasia detection for real-time analysis of a/LCI scans [37]. Next, in order to overcome the limitations of current probe designs, we propose an easily fabricated and robust design for collecting the scattered light by utilizing only a single multimode fiber (MMF) for measuring angular scattering distributions from cells for pre-cancer detection [38]. At last, we present design and clinical applications of a combined a/LCI-OCT system for comprehensive screening and improved detection of esophageal dysplasia. We

anticipate these improved designs will lead to more efficient a/LCI with better clinical viability for precancer screening.

1.2 Document Organization

This dissertation is organized as follows. Chapter 2 will provide general background information about esophageal and cervical dysplasia, including the epidemiology, early surveillance and diagnosis, and treatment of the diseases. After that, Chapter 2 continues to discuss basic principles of a/LCI and OCT, including the theory, instrumentation and traditional processing methods, current clinical findings, as well as limiting factors. After that, Chapter 2 ends by giving an overview of alternative optical modalities for dysplasia detection. Chapter 3 presents a comprehensive analysis of how various a/LCI parameters affect the diagnostic capabilities for dysplasia detection and discuss guidance for optimal a/LCI probe designs. Chapter 4 introduces a new processing algorithm of a/LCI signals based on machine learning for fast and accurate identification of cervical dysplastic tissues and demonstrates the generalizability of the algorithm across data collected from different a/LCI instruments. Chapter 5 presents an easily fabricated and robust design and development of an optomechanical system for collecting and reconstructing the scattered light by utilizing only a single multimode fiber (MMF), as an alternative to the coherent fiber bundles. Chapter 6 demonstrates development of a combined a/LCI-OCT system and a clinical feasibility study for comprehensive screening and improved detection of esophageal dysplasia. The base foundational design of the path-length-matched linear fiber array is

introduced as an alternative solution for the coherent imaging bundles, and further validation experiments for OCT and a/LCI are demonstrated respectively. Chapter 6 then presents the results of a clinical study of the combined system and discusses the performance of the new instrumentation. Finally, Chapter 7 summarizes the current state and outlook of these projects.

2 Background

This chapter provides background information related to the subsequent research topics in this dissertation. The first two sections cover both the esophageal and cervical dysplasia, including the progression of the disease, early surveillance and clinical treatment. Section 2.3 and Section 2.4 present background on optical coherence tomography (OCT) and angle-resolved low-coherence interferometry (a/LCI), including their system instrumentation, data processing techniques, and current clinical findings. Section 2.5 introduces alternative optical modalities for epithelial dysplasia detection.

2.1 Esophageal Dysplasia

Dysplasia, also known as precancer, is an abnormal alteration of the tissue signifying a stage that may precede the development of cancer. In the esophagus, gastroesophageal reflux disease (GERD) can cause changes of the normal stratified squamous epithelium to metaplastic columnar epithelium containing goblet cells [39]. Recurrent GERD symptoms can lead to erosive esophagitis, followed by an aberrant healing processing resulting in a metaplastic, specialized intestinal epithelium called Barrett's esophagus (BE) [40, 41].

Although BE is classified as a non-dysplastic metaplastic condition, intestinal metaplasia cells may develop progressively more abnormal features, ranging from low-grade dysplasia (LGD) to high-grade dysplasia (HGD) [42, 43]. Based on the stage of the progression, treatment strategies would be different. Moreover, the incidence rate of EAC has increased rapidly over the last 40 years in the U.S. [44]. Survival of EAC has

improved in recent years, however, the 5-year-survival rate is still estimated to be less than 20% [45]. For this reason, timely surveillance procedures become significant for intervening prior to the development of EAC.

2.1.1 Surveillance and Early Diagnosis

The metaplasia-dysplasia-carcinoma progression in BE has led to adoption of an endoscopic surveillance to detect prevalent or incident dysplasia or EAC. Current upper-endoscopic surveillance of BE follows a gold standard called the "Seattle protocol" [4, 46], where four-quadrant biopsies are taken every 1-2 cm of the BE-affected tissue.

This method has shown substantial improvement in patient survival rate in multiple studies [47-50], but there are problems associated with this biopsy standard. One significant problem is that, usually less than 5% of the affected tissues can be covered and physicians do not adhere to this recommended protocol in practice [4, 51]. Furthermore, dysplasia is not visible under endoscopy, and the distribution of dysplasia is highly variable. All of which may lead to low-coverage of at-risk tissues and sampling error [52].

There is also significant inter-observer variability among pathologists. It has long been recognized that early diagnosis across the spectrum of BE from no dysplasia to HGD/EAC is quite problematic, especially for non-dysplastic BE and low-grade dysplasia [53]. Many studies showed underinterpretation or overinterpretation in diagnosis, leading to less concordance between pathologists [52].

Another shortcoming is the cost of surveillance. Routine endoscopic surveillance could lead to substantial economic costs [54], with cost-effective ratios ranging from $10,000-50,000/quality-adjusted life-year gained [55, 56], which would not be an ideal solution for wide-scale applications for the general population. It is clear that an inexpensive and accurate diagnosis of dysplasia is critical for clinical decision making.

In recent years, a minimally invasive swallowable non-endoscopic capsule sponge device has been introduced as an alternative solution for screening BE [52]. This device consists of a capsule with a polyurethane sponge attached to a string/suture. The device is swallowed and withdrawn from the mouth, and esophageal cytology samples are collected along the esophagus. Protein marker expressed in intestinal metaplasia (trefoil factor 3 [TFF3]) or methylated DNA markers is extracted to predict the presence of BE. Sample collection can be performed by non-physician-trained providers and without sedation. In addition, the test is minimally invasive, and inexpensive. Nevertheless, the entire process could only provide negative/positive test results, but lacks indication of the disease's location. More importantly, while the sensitivity was 76%-94% and specificity was 62%-92% for detection of BE [57-59], it showed limited accuracy in detecting dysplastic BE, which is more clinically relevant [60].

2.1.2 Clinical Treatments

In recent years, esophageal eradication therapy (EET) has emerged as an effective treatment method for dysplastic BE [61], and avoids the morbidity and mortality associated with esophagectomy [62, 63]. Standard treatments include endoscopic

resection of any visible lesion, followed by ablative techniques such as radiofrequency ablation (RFA) and cryotherapy to achieve complete eradication of dysplasia (CED) and intestinal metaplasia (CEIM). During the ablation process, the ablation catheter is guided onto the affected tissue, and energy is delivered to the electrodes that are in contact with the esophageal lining that is being treated [61]. EET has proven to be a successful in eradicating dysplastic tissues, with studies showing the percentage of complete eradication ranging from 95%-98.5% after 12 months [52, 61, 64].

2.2 Cervical Dysplasia

Cervical cancer, another common epithelial malignancy, is the most common gynecologic cancer worldwide resulting in 342,000 deaths in 2020 [1]. The main etiologic factor for cervical cancer is persistent human papillomavirus (HPV) infection [65, 66], and it is estimated that HPV is the most common sexually transmitted infection in the United States [67]. The implementation of HPV vaccination programs in the United States have diminished the prevalence of HPV, dropping from 11.5% to 4.3% [68]. Despite advances in prevention, substantial regional and global disparities in the progression of cervical cancer still exists, as the vaccine access is extremely limited in many developing countries [69]. Furthermore, the vaccine uptake rates in the United States remains modest [70], as only 60% of all 13-17 year old adolescents have received 1 does of the vaccine series, and 37% had received 3 doses.[71]

In an analogous manner to esophageal dysplasia, cervical dysplasia also follows a predetermined course of progression, from low-grade squamous intraepithelial lesion

(LSIL) to high-grade squamous intraepithelial lesion (HSIL) [72], and this progression period usually occurs over a course of 5-8 years [73], leaving a wide window for interventions.

The current screening protocol uses cervical cytology (Papanicolaou smear) [74] and DNA testing for high-risk HPV as the primary initial screening tool for cervical dysplasia and cancer. Patients with abnormal tissues will receive a colposcopy examination, and histopathological analysis is used for target tissue diagnosis [75]. But colposcopy remain limited in sensitivity and specificity (0.85 and 0.69 respectively) [76, 77], and exhibits interobserver variability. There exists a need for a comprehensive screening tool for cervical dysplasia.

2.3 Optical Coherence Tomography (OCT)

2.3.1 Low coherence interferometry

The optical modalities implemented in this dissertation all utilize low coherence interferometry (LCI), for depth-resolved measurements of the sample, as analogous to ultrasound imaging. Instead of using electronic detection methods to separate the different sound waves to construct the tomogram of the sample, LCI utilizes an interferometer, such as a Michelson or Mach-Zehnder interferometer, to determine the pathlength traveled by the photons that have traveled through tissue to provide depth-resolved measurements. In a typical Michelson interferometer setup, the light is split into the reference and sample arms, where the former light beam is reflected by the mirror while the latter light beam is reflected and backscattered from the sample. Both

arms are combined at the beamsplitter, and interfere prior to detection. The interference will only occur when the optical path length (OPL) between the sample and reference arms is within the coherence length of the light source, where the coherence length is defined by,

$$\boldsymbol{L_c = \frac{2\ln(2)}{\pi}\frac{\lambda_0^2}{\Delta\lambda}} \quad \textbf{(2.1)}$$

where L_c is the coherence length, λ_0 is the central wavelength, and $\Delta\lambda$ is the bandwidth of the light source.

2.3.2 Spectral Domain OCT

OCT is a common implementation of LCI systems used for biomedical imaging. Early OCT implementations, known as "time-domain" OCT (TD-OCT), use a moving reference arm which sweeps spatially and measures the samples reflectivity at various depths. Recently, Fourier-domain OCT (FD-OCT) was introduced which provided better sensitivity and improved imaging speed [78-80].

Spectral-domain OCT (SD-OCT), a class of FD-OCT, uses a broadband light source and a spectrometer for the instrumentation setup. The signal detected by the interferometer can be described as:

$$I(\lambda) = E_s(\lambda)^2 + E_r(\lambda)^2 + 2Re[E_s(\lambda)E_r(\lambda)\cos(2k\Delta L)] \quad \textbf{(2.2)}$$

where $E_s(\lambda)$ and $E_r(\lambda)$ are the sample and reference field respectively, λ is the wavelength, $k = \frac{2\pi}{\lambda}$ is the wavenumber, ΔL is the OPL between the sample arm and the reference arm. This signal is detected by the spectrometer, which acquires an

interferogram of intensity as a function of wavelength. The detected spectrum is then interpolated and resampled into an evenly spaced function of wavenumber, and then a Fourier transform is applied to each interferogram to generate an A-scan, several of which are combined to create a B-scan (tomogram). Numerous hardware or numerical compensation techniques have been implemented to account for chromatic dispersion [81-83].

Many deterministic parameters govern the imaging performance of Fourier-domain LCI systems. One important parameter indicating the ability of the system to resolve depth-resolved features is the axial resolution, which is determined by the coherence length (Eq. 2.1). Since the depth information is encoded in the spectral frequencies of the interferogram, the spectral sampling, defined by pixels on the imaging spectrometer, will limit the imaging depth and can be characterized by:

$$\hat{Z}_{max} = \frac{\pi}{2\delta_s k} \quad \textbf{(2.3)}$$

where $\delta_s k$ is the spectral sampling interval in wavenumber units [84].

In the lateral dimension, the resolution is determined similarly to conventional microscopy, where the lateral spot size can be described as,

$$\delta_x = 0.37 \, \frac{\lambda_0}{NA} \quad \textbf{(2.4)}$$

where λ_0 is the central wavelength, and NA is the numerical aperture of the objective lenses, which also determines the field of view (FOV). So OCT exhibits a fundamental trade-off between the FOV and lateral resolution.

2.3.3 OCT for Dysplasia Detection

Endoscopic OCT devices are becoming an intriguing research tool for in vivo detection of disease because they provide high-resolution depth-resolved visualization of the tissue. An early study by Isenberg *et al.* [18] showed detection accuracy of dysplasia in BE using an endoscopic OCT. In total, they analyzed 314 biopsies from 33 patients ranging from LGD, HGD and intramucosal cancer, and classification results were compared with histology. The method showed sensitivity and specificity of 68% and 82% respectively for detecting LGD/HGD over non-dysplastic BE (NDBE), with an overall accuracy of 78% and relatively low PPV.

A similar study by Evans *et al.* collected 177 biopsies from 55 patients, where the severity of mucosal surface maturation and glandular architecture was used to distinguish EAC/HGD from LGD/squamous intestinal metaplasia [85]. The study achieved 83% sensitivity and 75% specificity, with relatively low PPV (56%). A later study from the same group developed a diagnostic algorithm to assess layered architectures and presence of epithelial glands for identifying dysplasia [86]. Finally, Qi *et al.* developed a computer-aided diagnostic algorithm based on feature extraction and selection of 96 endoscopic OCT images, yielding an accuracy of 84% for classification of non-dysplastic vs. dysplastic BE tissue [87]. Other research focuses on using optical coherence tomography angiography (OCTA) and volumetric imaging to associate microvascular features like abnormal vessel branching and heterogeneous vessel size with LGD/HGD, and achieved 94% sensitivity and 69% specificity [88].

A more recent study conducted by Osman *et al.* [89], used OCT with micromotor catheters for in vivo assessment of dysplasia in patients with BE. In total, 74 OCT datasets obtained from 14 patients were analyzed to identify irregular mucosal patterns and cross-sectional features. Although irregular mucosal patterns were observed in 100% of neoplasia (LGD, HGD, and EAC) datasets, it also appeared in 35% of NDBE datasets. Other differential features were also analyzed, resulting in limited differences [89]. Though endoscopic OCT has shown effectiveness in distinguishing between non-BE and BE, the ability to identify dysplasia is limited. We hope that the development in a/LCI, and specifically combining the two modalities later in this thesis will address these limitations, and provide an alternative non-invasive diagnostic tool for dysplasia detection.

2.4 Angle-resolved Low-Coherence Interferometry (a/LCI)

2.4.1 Principles and Instrumentation

Angle-resolved low-coherence interferometry (a/LCI) is a non-invasive optical technique which measures depth-resolved nuclear morphology (nuclear size and nuclear density), which serves as a biomarker for dysplasia. Because angular light scattering is highly sensitive to changes in scatterer properties, variations in scattering distributions are used to extract the size and relative refractive index of scattering objects such as cells, nuclei, and even smaller organelles [13, 21]. The a/LCI instrument collects elastically scattered light from the sample at a specific angular range, shown in Figure 2.1. These angular scattering profiles can be analyzed computationally by modeling the

cell nuclei using various scattering models and using inverse light scattering analysis (ILSA) algorithms to extract depth-resolved, quantitative measurements of nuclear morphology [21].

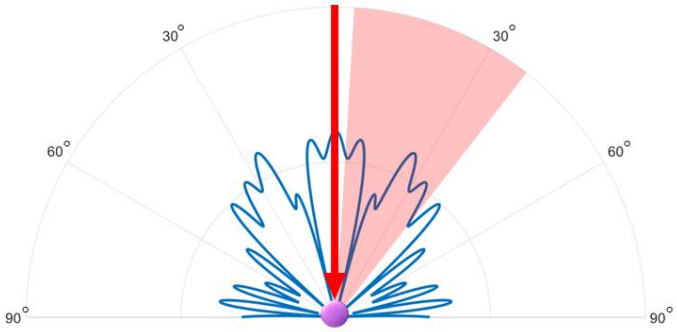

Figure 2.1 Schematic diagram showing the principle of a/LCI.

A collimated beam of light (red arrow) is incident onto the cell nuclei. Nuclei are roughly spherical, and can be modeled as a Mie scatterer. Backscattered light (blue line) is collected within the clinical a/LCI system's angular range (shaded red region).

A schematic diagram of the a/LCI instrumentation is shown in Figure 2.2. a/LCI typically uses a Mach-Zehnder interferometer setup, with an 830 nm superluminescent diode (SLD, Superlum, Moscow, Russia) as the light source. P-polarized light from the sample arm is delivered to the sample using a PM fiber, and the GRIN lens produces a collimated but off-axis beam to direct the light onto the sample at an angle. The backscattered light from the sample is then collected by the GRIN lens, and each angular component of the scattered field is mapped discretely to each channel in the coherent imaging bundle (Schott Inc., Southbridge, MA). The light then propagates to the second beam splitter and interferes with the beam in the reference arm. The interference signal

is then collected using an imaging spectrometer (SP-2150i, Princeton Instruments, Acton, MA) with a high sensitivity charge coupled device (CCD) camera (PIXIS: 100, Trenton, NJ).

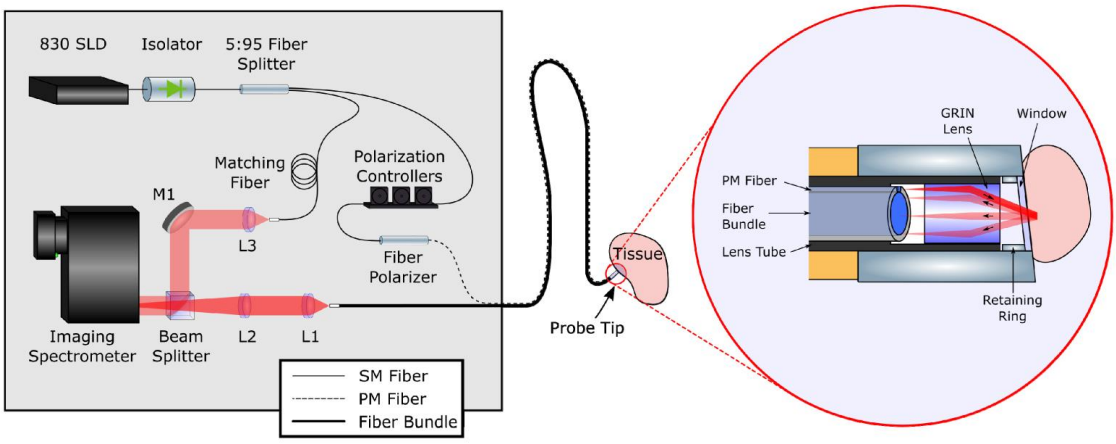

Figure 2.2 Schematic of a typical a/LCI instrument.

adapted with permission from [26]. A polarized beam is guided to the target tissue site using a polarized maintenance fiber, and the scattered light from the tissue site is collected through the fiber bundle.

2.4.2 Signal Processing

A typical block diagram for the traditional a/LCI processing method called inverse light scattering analysis (ILSA) is shown in the left of Figure 2.3, and described in detail in [13]. First an a/LCI scan is used to determine the start of the tissue, shown in Figure 2.3(B). The a/LCI data are summed across all scattering angles, and this produces a depth-resolved tissue reflectivity profile (A-scan, shown in Figure 2.3(C)). The start depth of the tissue can then be identified as the sharp increase of the intensity in the A-scan. Next, the a/LCI scan is segmented into depth bins with a 50 μm increment, down to 300 μm in tissue depth. The depth-bin from 200 to 250 μm is selected for analysis, representing the signals from the basal layer of the tissue [23, 29]. The depth-binned

a/LCI scan is then summed across all depths in the bin (shown in red regions) to produce an angular scattering profile (intensity vs. scattering angle).

Several additional steps are conducted to extract the scattering signals of the cell nuclei. First, low pass filter is applied to each angular scattering profile by applying a Fourier transform to the angular scattering profile, which represents a two-point correlation function of the sample as first described by Pyhtila *et al.* [21]. The cutoff frequency is placed after the first observed peak in this correlation function to suppress high frequency components in the scattering signal that arises from long-range intercellular correlations [21, 22]. A polynomial is fitted to the data and then subtracted to isolate the oscillations later for fitting, and remove low-frequency components arising from subcellular structures and organelles smaller than the cell nuclei.

After this, the isolated oscillatory scattering component is compared to a theoretical model to extract nuclear morphology information from the scan. Based on these, two different theoretical models have been introduced for the development of a/LCI: Mie-theory and T-matrix [21, 90, 91]. Both methods require a database of simulated angular scattering profiles computed using either Mie theory or T-matrix calculations for a range of scatterer sizes and refractive indices. The difference is that Mie theory models the cell nuclei as spherical scatterers while T-matrix models the cell nuclei as spheroidal scatterers. Thus, the T-matrix requires a larger library of profiles, and is more computationally intensive. The processed angular scattering profile is compared to the simulated dataset to find the best fit, using chi-squared (χ^2) error as the

comparing metric. Certain thresholds are set to exclude non-unique solutions. Other methods including the wavelet transform method, described in detail by Ho *et al.* [30] have been introduced to improve efficiency by trading off fitting accuracy for faster speed.

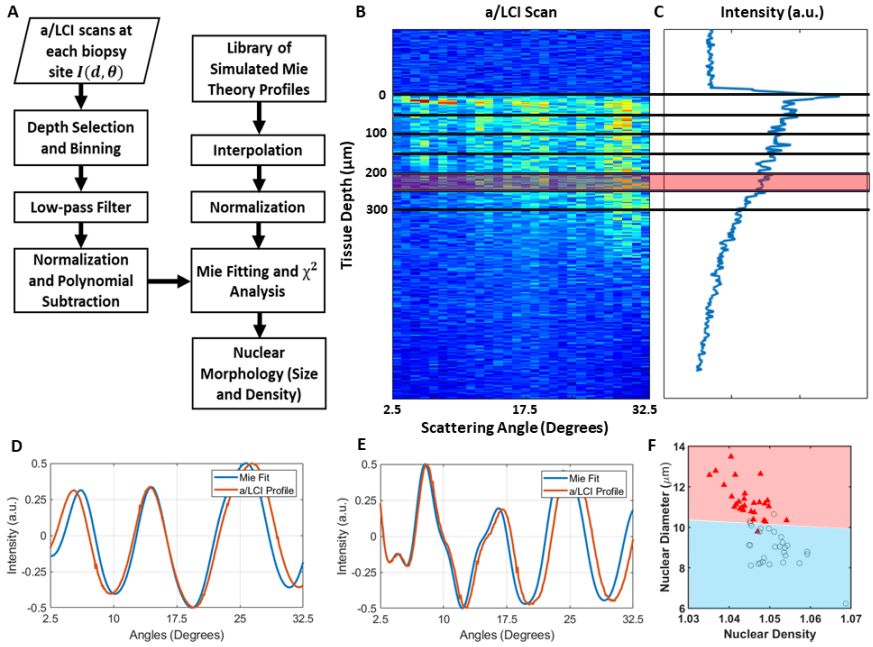

Figure 2.3 Signal processing pipeline for a/LCI. (A) Flow chart of a/LCI signal processing. (B) a/LCI scan of a healthy tissue. (B) A depth-resolved A-line of the scattering profile to find the start of the tissue. The angular scattering profile at 200-250 μm depth bin (shown in shaded red) is selected for analysis. Mie fitting results of a healthy tissue (shown in D) and a dysplastic tissue (shown in E) based on chi-squared analysis. (F) Scattering plot of all biopsy sites, where the red region shows the dysplastic biopsies, and the blue regions shows the healthy biopsies.

2.4.3 Previous Clinical Studies

Previous a/LCI clinical studies have shown substantial success in detecting dysplasia. In the esophagus, the first *in vivo* clinical study compared measurements of nuclear morphology from BE tissues with the histopathological analysis of co-registered tissue biopsies [92]. A total of 172 optical biopsies were collected from 46 enrolled

patients, and a/LCI nuclear morphology prediction was able to achieve perfect (100%) sensitivity and 84% specificity in detecting dysplasia, with an accuracy of 86% and perfect (100%) negative predictive value (NPV). A more detailed descriptions of the clinical results are summarized by Terry *et al. [92]*.

In the cervix, an *ex vivo* clinical study involving 20 patients at Duke University Medical Center achieved 100% sensitivity and 90% specificity in detecting dysplasia, along with an accuracy of 91.3% and a 100% negative predictive value (NPV) [29]. A later clinical study involving 40 patients at the University of California, San Francisco (UCSF) Gynecologic Dysplasia Clinic and the UCSF HPV cohort study showed 100% sensitivity and 97% specificity in detecting dysplasia, and 100% sensitivity and 82% specificity in distinguishing HGD from benign and LGD [27], which is often the more clinically relevant differentiation.

In the colon, a pilot *ex vivo* study of 27 patients undergoing partial colonic resection surgery was conducted to evaluate the ability of a/LCI in identifying dysplasia, and achieved 92.9% sensitivity and 83.6% specificity in detecting dysplasia, along with an accuracy of 85.2% [93].

2.4.4 Limitations

Many practical challenges hinder the abilities of a/LCI in clinical applications. One important challenge lies in the aspect of the a/LCI's technical design, where a/LCI system utilizes a coherent fiber bundle for delivering the scattered field from the tissue to the optical engine [27, 92]. Although it provides the multi-channel collection for the

angular scattered field, it remains a limiting feature of the device due to its low commercial availability, high cost, and poor performance in coherent imaging with mismatched optical path length and coherent cross talk between elements [35]. This inevitably degrades the final resolution and image quality. In this dissertation, alternative methods for clinical applications will be introduced to overcome this problem imposed by the imaging fiber bundle.

Another problem lies in the nature of this technology. a/LCI is not an imaging modality, which means that it can only detect light scattering signals but cannot provide visual guidance of the tissue, lacking instant feedback on the surface condition of the target. It presents an even more difficult challenge when screening for precancerous tissues in large surface areas, like in the esophagus [92, 94]. And in many cases, this must be done in conjunction with normal endoscopy, which causes more constraints. Also, the long computation time for the algorithm has hindered the clinical adoption of a/LCI. The collected angular scattering profile would need to traverse through a database containing thousands of profiles to find a best fit based on chi-squared analysis, and this hampers the ability to provide real-time diagnostic information during clinical trials. A portion of this dissertation will focus on a new method for extracting diagnostic information as an alternative to the ILSA algorithm.

2.5 Alternative Optical Techniques for Dysplasia Detection

Optical techniques offer significant advantages over traditional methods due to their noninvasive and nonionizing nature. This has inspired the development of other

alternative optical methods for early detection of dysplasia by detecting biochemical and structural changes in the tissue. To be concise with the other two modalities mentioned in this thesis, this section provides a survey of alternative optical techniques only for dysplasia detection.

Several traditional optical modalities based on inelastic light scattering have been introduced for dysplasia detection, including autofluorescence microscopy [9, 95, 96], fluorescence and reflectance spectroscopy [97-100], and Raman spectroscopy [101-103]. Some of these methods have advanced their technique using an endoscopic probe for spectroscopic measurements [10, 102, 104-106], but still suffer the same shortcomings as to traditional point-probe design in that they lack imaging guidance.

Other non-imaging techniques including elastic-scattering spectroscopy (ESS) [14, 107-109], which analyzes the spectrum of diffuse light scattering, and light-scattering spectroscopy (LSS) [17, 110-112], which analyzes the spectrum of single-scattered photons, have also been introduced for identifying dysplasia. In general, ESS collects the scattered photons close to the illumination spot, and directly analyzes the spectrum by extracting optical properties of the tissue, using predetermined spectral regions, or machine learning. Recent applications of ESS range from identification of peripheral lung tumors [113], skin cancer [114], colonic lesions [109], breast cancer [115], dysplasia in BE [14], oral cancer [116], and colonic polyps [15]. LSS utilizes spectral filtering to allow independent analysis of orthogonal spectral channels, and extract the photons signals that have been only scattered once or a few times in the epithelial layer

[110]. Recent work in LSS has primarily been addressed towards endoscopic applications, where the method exhibited a sensitivity over 90%, and specificity over 95% [17, 112] for detecting dysplasia. Other applications in detecting cystic lesions in the pancreas have also been demonstrated [111].

High resolution imaging techniques such as OCT (already summarized in section 2.3.3), endoscopic confocal microscopy [117-119], high resolution micro-endoscopy (HRME) [120-123] have been used to detect changes in dysplastic tissues. HRME is able to detect neoplastic progression by detecting an increase in the nucleus to cytoplasm ratio in neoplastic tissue sites, and this method have demonstrated effectiveness in detecting neoplasia in patients with BE, resulting in a sensitivity of 84% and specificity of 85% [120]. Recent clinical results of HRME presented in low-resource settings exhibited a sensitivity of 92% and specificity of 72% for identifying cervical dysplasia [121]. These high-resolution imaging methods all suffer from the need for an expert interpreter to evaluate the image, which is time-consuming and difficult to accommodate during routine clinical visits.

3 Angular range, Sampling and Noise Considerations for Inverse Light Scattering Analysis of Nuclear Morphology

3.1 Introduction

As discussed in the previous chapters, a/LCI seeks to solve the inverse problem of determining the average nuclear size and relative refractive index within tissue from light scattering data, using an inverse light scattering analysis (ILSA) algorithm based on Mie theory. Although Mie scattering from a spherical scatterer is fully defined in amplitude, phase and polarization over the total 4π solid angle [124], only a small, discretized portion of the scattering field may be acquired from the tissue in a/LCI.

During in-vivo a/LCI imaging, the acquired angular range is usually set by the numerical aperture (NA) of the objective lens or the GRIN lens [27, 125], which is typically ~0.5 and limits the range of accepted angles to 35 degrees under practical circumstances [126]. As an interferometric method, the scattered field is mixed with the reference field, and imaged onto the slit of an imaging spectrometer, where the Mie scattering profile is limited to a single line along a radial segment of the scattering sphere. Further discretization of the angular scattering profile is introduced during collection using an imaging bundle and upon detection.

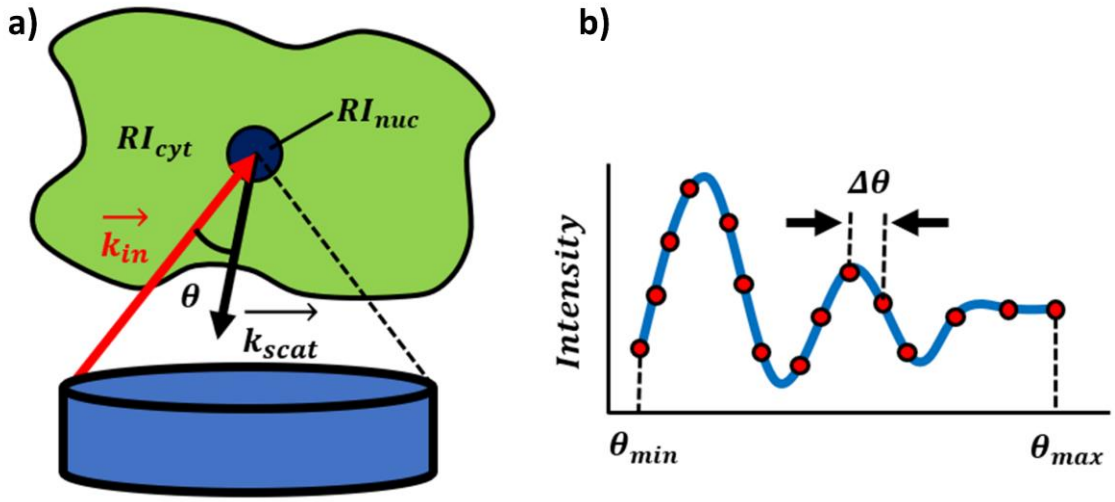

Figure 3.1 Schematic diagram of data acquisition and angular scattering spectrum, showing parameter definitions. Adapted from [36].

This collected 1D scattering function is a discrete function $I(\theta_n)$, comprised of both signal and noise, which measures the irradiance of the scattered field from tissue as a function of discretized scattering angle θ_n. The fundamental problem of a/LCI is the ill-posed inversion problem of this scattering function to obtain nuclear size and density, and it has not been established if a/LCI measurements of $I(\theta_n)$ are optimized for this. Furthermore, new a/LCI instrumentations are being developed which compress the scattering function, either by reducing angular range to create scanning capability [127] or reducing sampling frequency using modified fiber bundles or single-mode fiber arrays to improve the signal-to-noise ratio (SNR) [35, 125]. While novel a/LCI designs include attractive new features which will enhance clinical viability, the unknown diagnostic impact of these changes is a significant constraint on technological development.

Here in this chapter, a summary of a published manuscript [36], we comprehensively analyze the impact of reductions in angular range and angular sampling frequency on the diagnostic performance of a/LCI. The nuclear morphology values extracted from patients are utilized to simulate noise-free digital scattering phantoms, and quantify the sensitivity of a/LCI to deterioration of signal fidelity. These results are further applied to characterize a scanning a/LCI probe, where the diagnostic utility is analyzed with a loss in angular range. A comprehensive understanding of the diagnostic impact of alterations to the scattering function will help to guide future optical design, and encourage innovation in the field of diagnostic modalities based on tissue scattering.

3.2 Methods

3.2.1 Data Pre-processing

Detailed description of a/LCI instrumentation and the ILSA algorithm are discussed in Section 2.4. Briefly, a/LCI is based on a Mach-Zehnder interferometer, where light from a broadband light source is split into the sample arm and reference arm. In the sample arm, the light is directed onto the tissue at an oblique angle using a polarization-maintaining fiber and a gradient-index (GRIN) lens. Backscattered light from the tissue is collimated through the same GRIN aperture, as shown in Figure 3.1, and imaged onto a coherent fiber bundle, positioned at the Fourier plane of the GRIN lens. The light is then combined with the reference arm, and detected using an imaging

spectrometer. Raw data from the imaging spectrometer is interpolated to be linear in k-space, and the interference signal is Fourier-transformed line-by-line to produce an a/LCI scan, comprising a two-dimensional (2D) map of scattering intensity as a function of depth within tissue, $I(\theta, d)$.

The signal processing pipeline follows the flowchart in Figure 3.2, adapted from [36]. the a/LCI scans are first segmented into 50 μm depth bins, with a total depth range up to 300 μm. The depth bin from 200 to 250 μm is selected as the estimated basal/parabasal layer of the epithelium, which is known to be most diagnostically relevant [128]. Binning is performed over this selected depth range, producing a 1D scattering distribution $I(\theta_n)$, which is low-pass filtered and polynomial-subtracted to isolate the oscillatory component of interest.

The primary goal of this study is to elucidate the effects of compression of this scattering distribution $I(\theta_n)$ on the diagnostic capacity of a/LCI, and this is compared with the full angular range and sampling available for each profile. In this version of the study, the angular range of backscattered light is limited between $\theta_{min} = 2.5°$ and $\theta_{max} = 33.3°$, with a sampling period $\Delta\theta$ of approximately 0.45° (actual value 0.4526°, sampling frequency 2.21 degree^{-1}). The scattering distribution is altered by one or a combination of three different parameters, sampling period $\Delta\theta$, θ_{min} and θ_{max}, and then compared to a library of simulated Mie theory profiles until a best fit is found using chi-squared (χ^2) error as a comparative metric. This process is repeated for all scans with sufficient signal as determined by a quantitative threshold, and nuclear

morphology values are averaged across scans to calculate the nuclear diameter and nuclear density at a given biopsy site.

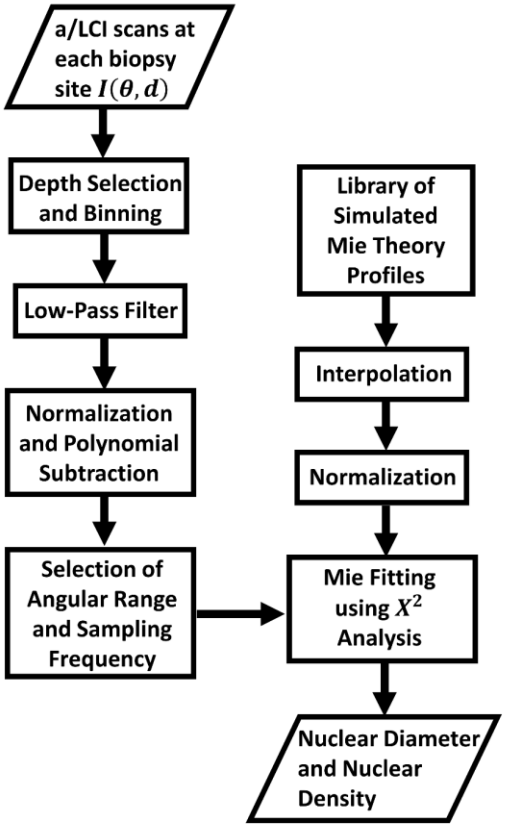

Figure 3.2 The inverse light scattering analysis (ILSA) algorithm pipeline, adapted from [36].

In the original cervix study [27], nuclear morphology values collected from 40 patients were compared with co-localized tissue biopsies, which were stained with hematoxylin and eosin and analyzed by a pathologist blinded to the a/LCI optical biopsy results. The biopsies were categorized as benign or dysplastic, with dysplasia subdivided into low and high-grade squamous intraepithelial lesions (LSIL and HSIL, respectively). Each patient was under voluntary informed consent, and the study was

approved by the Institutional Review Boards of UCSF and Duke University. A detailed description of the clinical study protocols and ethical standards is provided by Ho *et al* [27].

3.2.2 Selection of Sampling Frequency and Angular Range

The first parameter which was addressed was sampling frequency, since reducing the number of samples per unit scattering angle would also reduce instrument complexity. Sampling intervals were selected at integer multiples of the native period $m\Delta\theta$, where m = 1, 2, 3, … to avoid addition of information associated with interpolation at other sampling frequencies.

Reduction of information in the scattering function may also manifest as a reduction in angular range, which is implemented in recent advances of a/LCI allowing wide-area scanning of tissue [127]. To address this, either θ_{min} or θ_{max}, was fixed to its native value, with the opposite variable gradually obscured by intervals of $\Delta\theta = 0.9°$.

Reductions in both sampling frequency and angular range are likely to occur, and viable optical systems may involve tradeoffs between the two. To accurately assess this large parameter space, combinations of the three variables (θ_{min}, θ_{max}, and $\Delta\theta$) were also investigated. For each combination of minimum angle and maximum angle, six sampling frequencies were investigated, with the number of datasets per sampling frequency limited by the possible values of angular range for a given $\Delta\theta$. In total, independent variation of all three parameters represents a total of 130 modified datasets.

A large number of statistical and combinatoric parameters exist to quantify the performance of binary classifiers. In a/LCI, nuclear density and nuclear diameter are plotted in 2D and the color of each marker is labeled by its clinical diagnostic results, shown as left bottom of Figure 3.4. Then linear discriminant analysis (LDA) is applied to find a linear classifier that effectively classifies dysplastic from nondysplastic biopsies. This threshold is then varied to create a receiver operating characteristic (ROC) curve. Area under the curve (AUC) can then be extracted, which quantifies the probability that the linear classification value of a randomly chosen dysplastic biopsy will be greater than that of a randomly chose nondysplastic biopsy, assuming the classifier ranks dysplastic tissues higher than nondysplastic sites. Sensitivity and specificity, positive predictive value (PPV), and negative predictive value (NPV) can then be extracted using the optimal classification threshold set by the nearest point to the top left of the ROC curve. The entire processing pipeline analysis was performed using MATLAB R2017b (MathWorks, Inc., Natick, Massachusetts) with a mean computation time ranging from 30 to 90 minutes per clinical dataset, depending on the number of samples per scattering profile $I(\theta_n)$.

3.2.3 Noise Sensitivity Analysis using Digital Phantoms

A current practical concern in a/LCI is the difficulty of differentiating the scattering signal from the noise in a clinical dataset. Because a/LCI is not an imaging modality, and the scatterer properties in tissue are not known a priori, it is unclear

which portion of the collected signal constitutes Mie scattering from cell nuclei, and which components constitute scattering from subcellular organelles or extracellular matrix that is diagnostically irrelevant for identifying dysplasia. Furthermore, several other clinical sources of noise exist that degrade signal quality, including probe movement, patient movement, and blurring of the profiles due to the imaging bundle and optics. Because of this, noise-sensitivity in a/LCI has not been well characterized in the literature to date.

In order to address this issue, noise-free "digital phantoms" were generated to simulate ideal scattering objects within tissue. The scattering distributions were digitally generated using MiePlot program software, with the nuclear size and density of each biopsy site corresponding to the value calculated from the full a/LCI dataset for that biopsy after scan averaging. Gaussian white additive noise with a standard deviation ranging from 0% to 250% of the signal was then applied to each generated noise-free phantom, and ILSA was performed for each noise level. Gaussian noise was chosen as the amplitude speckle distribution for the sum of a large deterministic (Mie) periodic signal with random smaller signals. Diagnostic performance metrics (AUC, sensitivity, specificity and NPV) were reported for each case.

3.2.4 Benchtop Testing of Scanning a/LCI Probe

Here, in order to experimentally characterize the impact of this study, a scanning a/LCI benchtop was used for validation. Traditional a/LCI probes utilizes only a single gradient-index objective lens for sample illumination and scattering collection. Here, a

rotational element termed the ROTOR and a scanning mirror are used to enable 2D scanning across the tissue surface, and is described in details in [127]. For a given a usable aperture diameter *d*, defined by the clear aperture less the collimated beam diameter, NA and focal length of the objective *f*, there is a trade-off between the scanning range *s* and angular collection range θ_r:

$$s^2 = d^2\left[1 - \left(\frac{\tan(\theta_r/2)}{\tan[\sin^{-1}(NA)]}\right)^2\right] \quad \textbf{(3.1)}$$

And a diagram displaying variable definitions is displayed in Figure 3.3. By varying the spacing between the lenses in this system, three configurations with varying angular collection and scanning ranges were tested, and compared with the predicted values.

By varying the spacing between the lenses in this system, three configurations with varying angular collection and scanning ranges were tested, and their measured values compared with those predicted by equation 3.1. Scattering from a PDMS phantom containing embedded polystyrene microspheres (12 μm diameter) was analyzed for each configuration to determine the angular collection, scan range, and subsequent fitting accuracy.

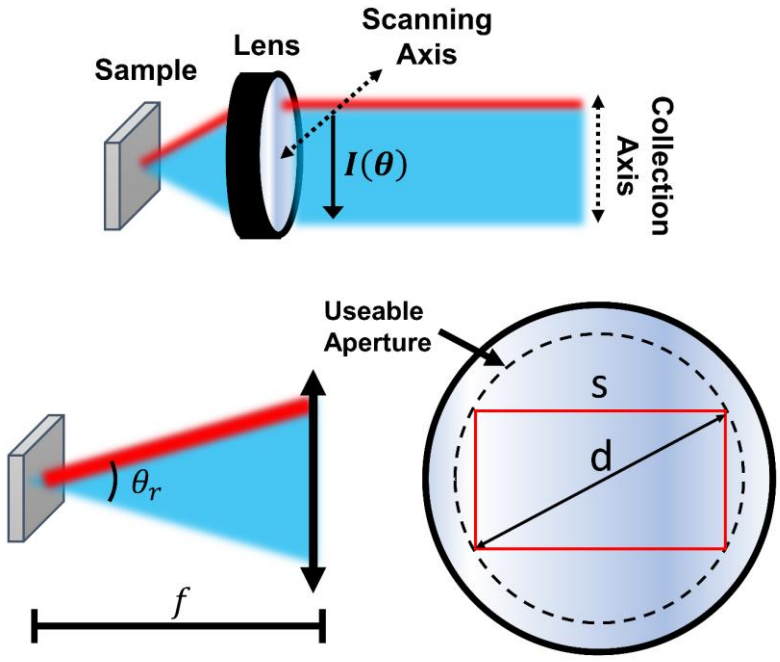

Figure 3.3 Pictorial displaying the objective lens of a scanning a/LCI system, adapted from [36].

3.3 Results

3.3.1 Angular Sampling

The baseline diagnostic performance is displayed in Figure 3.4, where we have an example Mie fitting result of an angular scattering distribution from the tissue (red curve) and its associated theoretical fit (blue curve) shown on the top of the figure. Significant separation of the dysplastic and normal biopsies is observed, shown in the right bottom of the figure, with the mean nuclear diameter significantly greater for dysplastic biopsy sites compared with normal sites (11.30 ± 1.14 vs. 8.99 ± 0.96 μm, $P <$

0.001). The sensitivity and specificity can be extracted from the ROC curve, resulting in 1.00 and 0.93, respectively. AUC of the ROC curve was 0.985, and NPV was 0.96, indicating excellent diagnostic performance. These values are slightly different from the original study [27], as we bypassed the complication of applying pair-wise binning of adjacent scattering angles. The angular range for this study was 30.8° and the angular sampling was 0.45°.

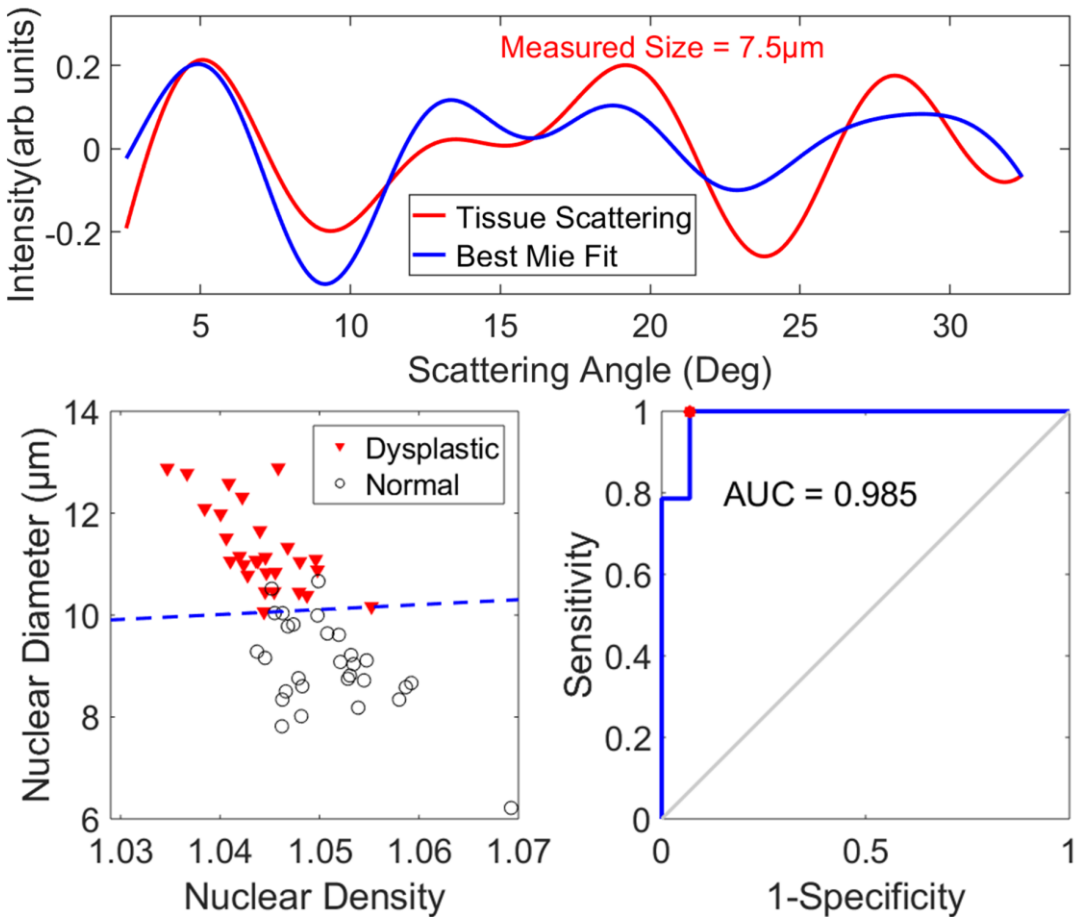

Figure 3.4 Diagnostic performance of the a/LCI instrument using the complete clinical dataset, $\theta_{min} = 2.5°$ and $\theta_{max} = 33.3°$, $\Delta\theta = 0.45°$ to form a baseline for comparison, adapted from [36].

Now, we characterize the ability of a/LCI to distinguish dysplastic from nondysplastic biopsies using reduced sampling frequency. Performance metrics for diagnostic capability were computed using modified clinical datasets, which were resampled at $\Delta\theta$ of 0.45°, 0.9°, 1.8°, 2.7°, 3.6° and 4.5°, respectively using the full angular range. Results are shown in Figure 3.5. As expected, diagnostic accuracy decreases as information is subtracted from the scattering spectrum, with the most dramatic reduction occurring between sampling periods of 3.6° and 4.5°. This trend is consistent across all four performance metrics in Figure 3.5. Interestingly, sensitivity and specificity can still maintain a high value (0.94 and 0.82) even when the angular spectrum is down-sampled by a factor of 8. This shows the capability of a/LCI to distinguish dysplastic from nondysplastic biopsy sites, even for significant reductions in angular resolution.

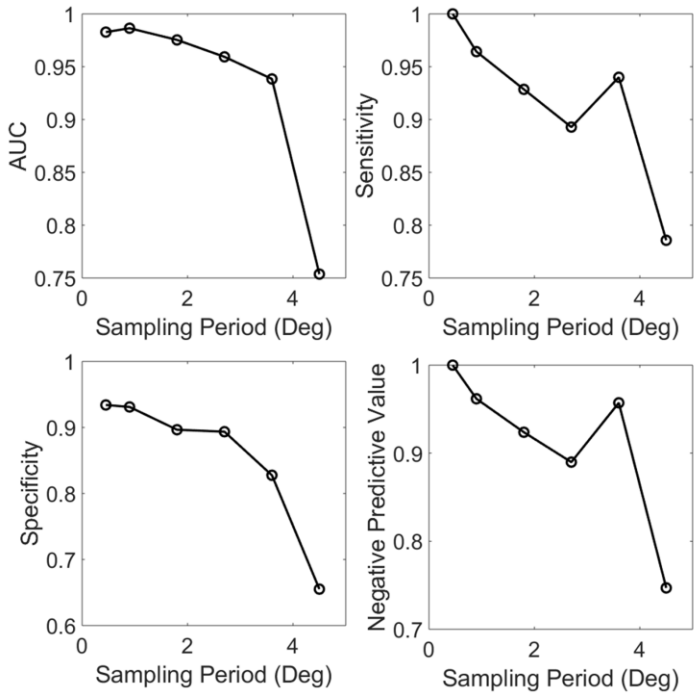

Figure 3.5 AUC, sensitivity, specificity and NPV at various sampling frequencies, using the full angular range available, adapted from [36].

3.3.2 Angular Range

Performance metrics for various angular ranges and a fixed sampling period of $\Delta\theta$ = 0.45° are shown in Figure 3.6. As expected, AUC, sensitivity, specificity and NPV expectedly decrease with reductions in angular range. However, significant diagnostic capability is preserved when θ_{min} is fixed to its lowest possible value, even for angular ranges below 25° (the sensitivity and specificity at $\theta_r = 21.7°$ are 0.89 and 0.90, respectively). Diagnostic performance drops more quickly for an equivalent reduction in angular range when θ_{max} is fixed to its maximum value of 33.3°, suggesting that lower scattering angles contain more diagnostically useful information than scattering further off-axis.

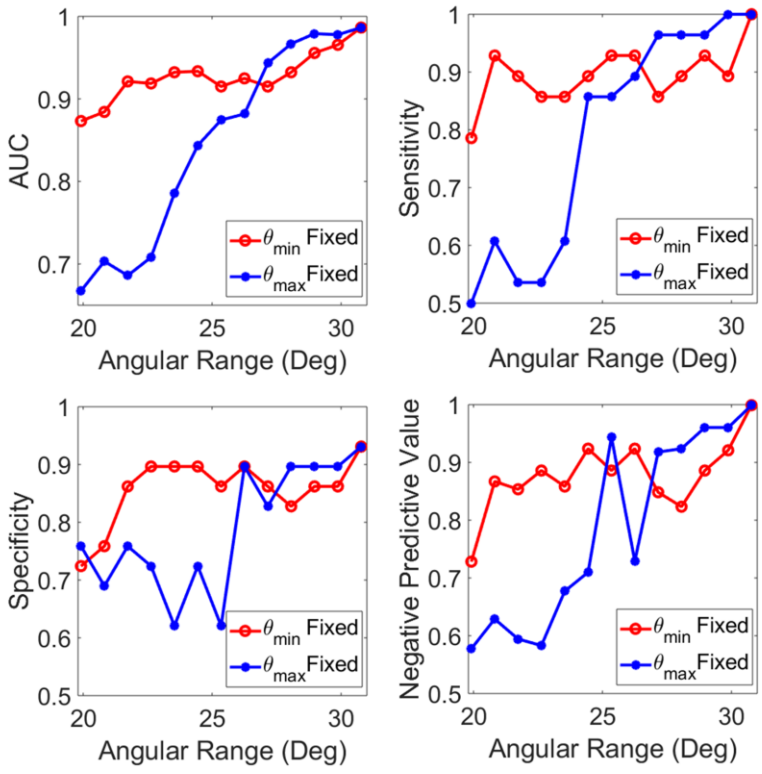

Figure 3.6 AUC, sensitivity, specificity and NPV at various angular ranges, using the native sampling period $\Delta\theta$ = 0.45°, adapted from [36].

3.3.3 Combined Angular Range and Sampling Analysis

To quantify the influence of both angular range and sampling frequency on the performance of the system, contour plots of diagnostic parameters are obtained by independently varying combinations of (θ_{min}, θ_{max}, $\Delta\theta$), with results fixing the maximum angle and adjusting the minimum angle shown in Figure 3.7 and the results fixing the minimum angle and adjusting the maximum angle shown in Figure 3.8.

Qualitatively, we observe the relative importance of scattering from lower scattering angles, as compared to wide-angle scattering, with optimal performance for all parameters occurring in a region with θ_{min}< 6° (Figure 3.7, shown in yellow). Improvements in θ_{max} offer improved specificity and NPV at most sampling frequencies, though the results are not as pronounced as improvements caused by a reduction in θ_{min} (Figure 3.8). Given an adequate (θ_{min}, θ_{max}) pair, a significant reduction in diagnostic utility is only observed when $\Delta\theta$ > 3.6°, suggesting that the native sampling period $\Delta\theta$~ 0.45 may be oversampling the scattering profile substantially, and increasing sampling period by a factor of 8 would still preserve high diagnostic accuracy. Compression of the acquired scattering profile by increasing $\Delta\theta$ has the potential to dramatically reduce instrument complexity, along with the amount of data per scan, and could potentially enable real-time processing of a/LCI optical biopsies.

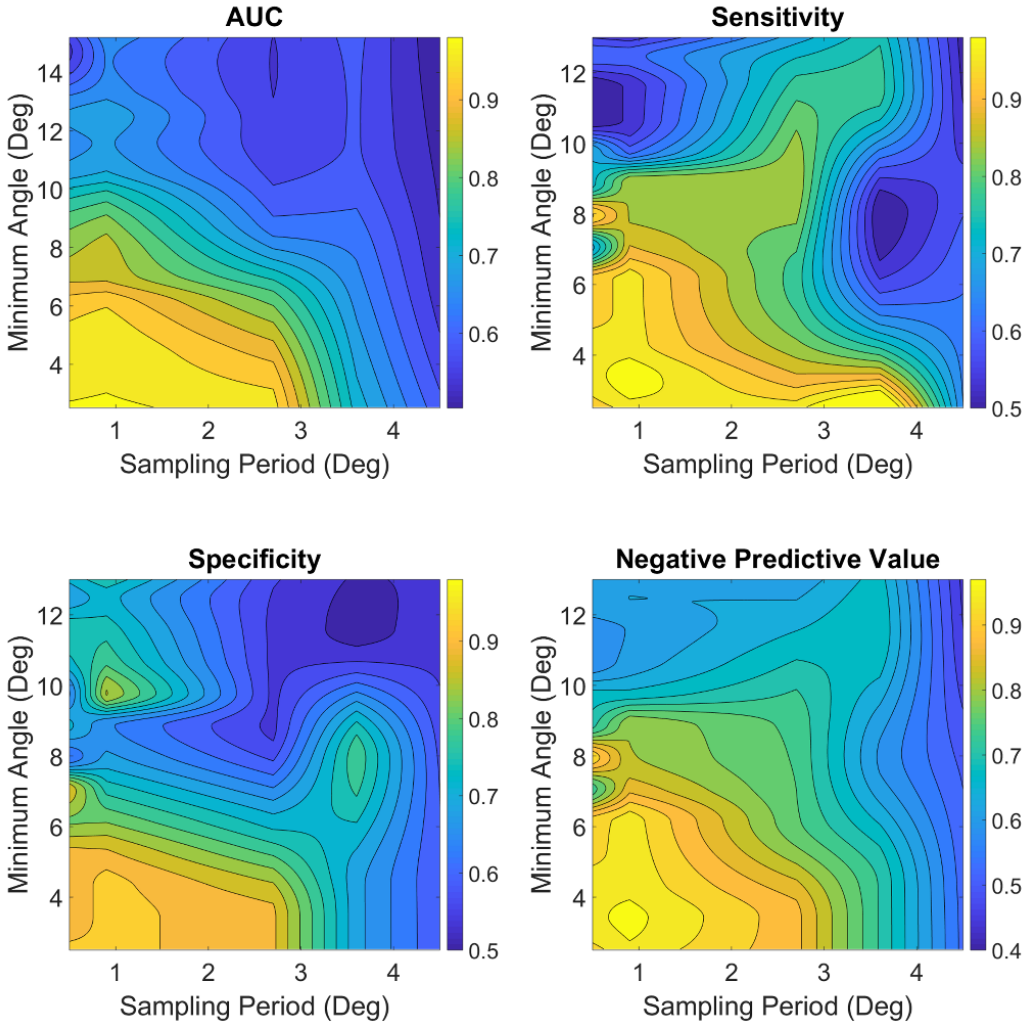

Figure 3.7 Contour plots of AUC, sensitivity, specificity and NPV at varying (θ_{min}, $\Delta\theta$) for a fixed optimal value of θ_{max}, adapted from [36].

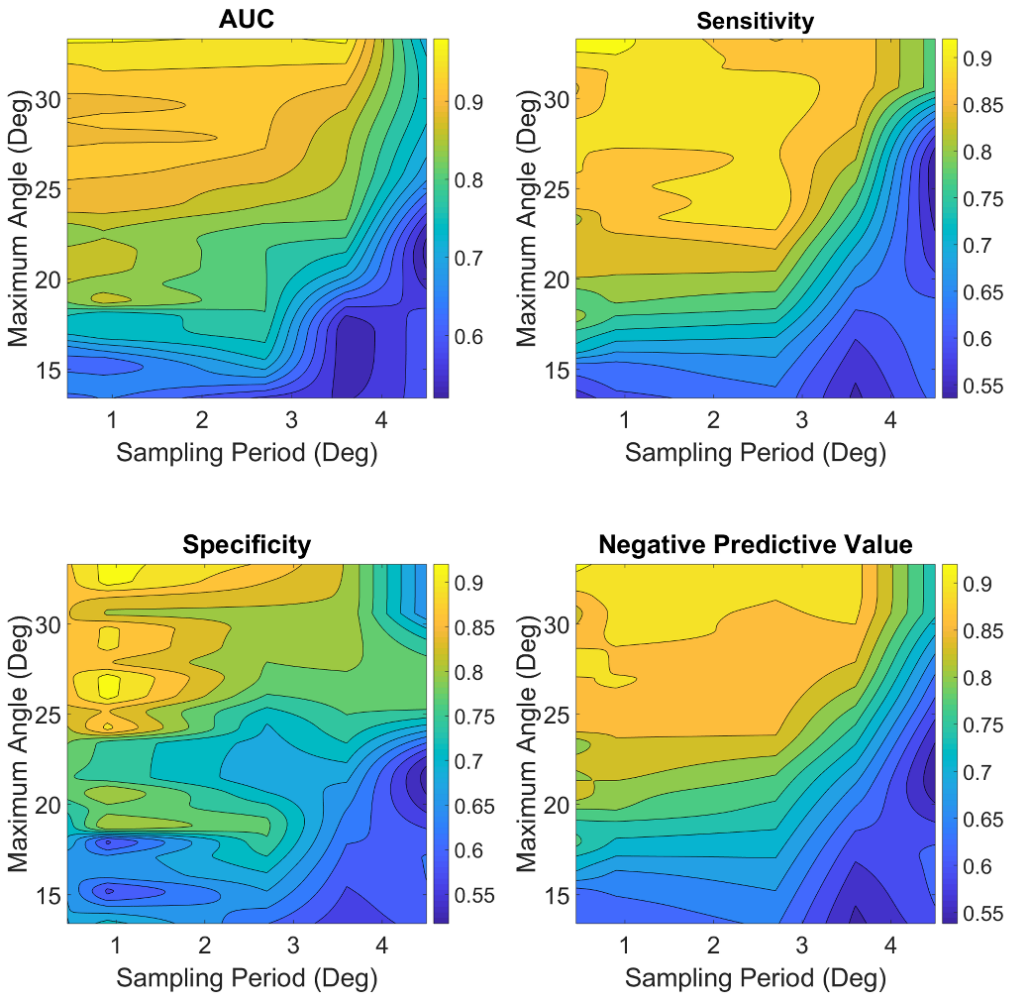

Figure 3.8 Contour plots of AUC, sensitivity, specificity and NPV at varying (θ_{max}, $\Delta\theta$) for a fixed optimal value of θ_{min}, adapted from [36].

3.3.4 Noise Tolerance Analysis

Results from the noise sensitivity analysis is shown below in Figure 3.9. Gaussian noise ranging from 0 to 250% of the signal intensity is added to the noise-free digital phantoms to investigate the noise tolerance of the ILSA algorithm. The Mie-fitting accuracy can represent how well the ILSA algorithm deals with the degradation in signal quality. The results in the figure show that the system demonstrates good noise

tolerance below 100% of additive noise to the signal, with a sensitivity, specificity and NPV of 0.89, 0.90 and 0.88 for 100% noise, respectively. Even at a substantial noise level of 250%, sensitivity, specificity and NPV are 0.79, 0.76 and 0.77, respectively, demonstrating the ability of a/LCI to quantify nuclear morphology even using extremely noisy measurements.

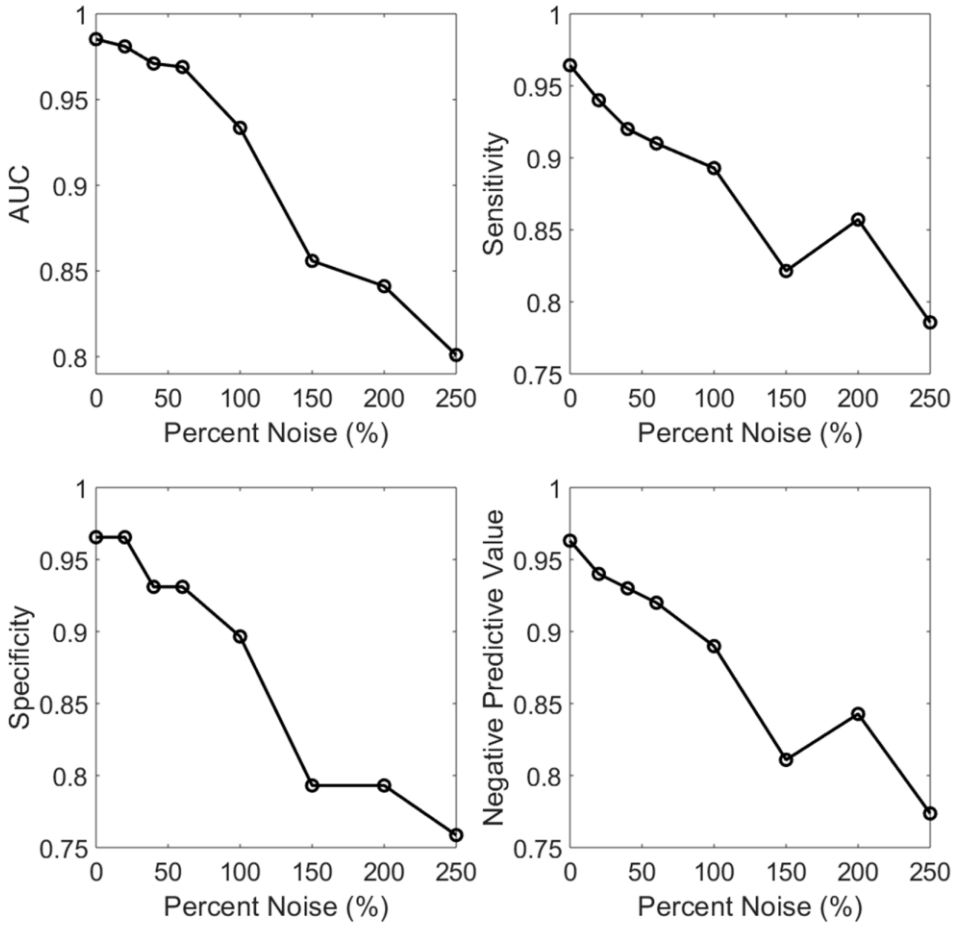

Figure 3.9 AUC, sensitivity, specificity and NPV at varying noise levels using digital phantoms at full angular range and sampling period $\Delta\theta$ = 0.45˚, adapted from [36].

3.3.5 Validation using Scanning Probe

Depth-resolved angular scattering profiles of the polystyrene bead phantom, described in section 3.2.4, were taken from the center scanning position for each configuration of the benchtop system, and displayed in Figure 3.10. For each case, the angular scattering profile extracted from 0 to 500 μm depth bin, was compared to the theoretical Mie scattering profile for 12 μm polystyrene beads in PDMS. The scanning range was determined by measuring the maximum range on the sample plane over which the illumination beam could be translated before the angular collection range was truncated by the probe aperture. To determine the fitting accuracy for each configuration, each angular scattering profile was processed using Mie Theory ILSA. Each experimental a/LCI profile was compared to a theoretical Mie scattering database calculated for varying sizes of polystyrene beads (5-18 μm diameter). The scatterer diameter was determined by the theoretical profile yielding the best fit using chi-squared minimization. The experimental angular scattering profiles and corresponding best-fit theoretical profiles are shown in the bottom row of Figure 3.10. The uncertainty in the nuclear diameter prediction is defined by the nearest theoretical scattering distribution where the chi-squared value has doubled from the minimum. For the high, medium and low angular collection configurations, the predicted scatterer diameter for a 12 μm sphere was 11.8 ± 0.4 μm, 11.6 ± 0.5 μm and 12.5 ± 0.8 μm, respectively.

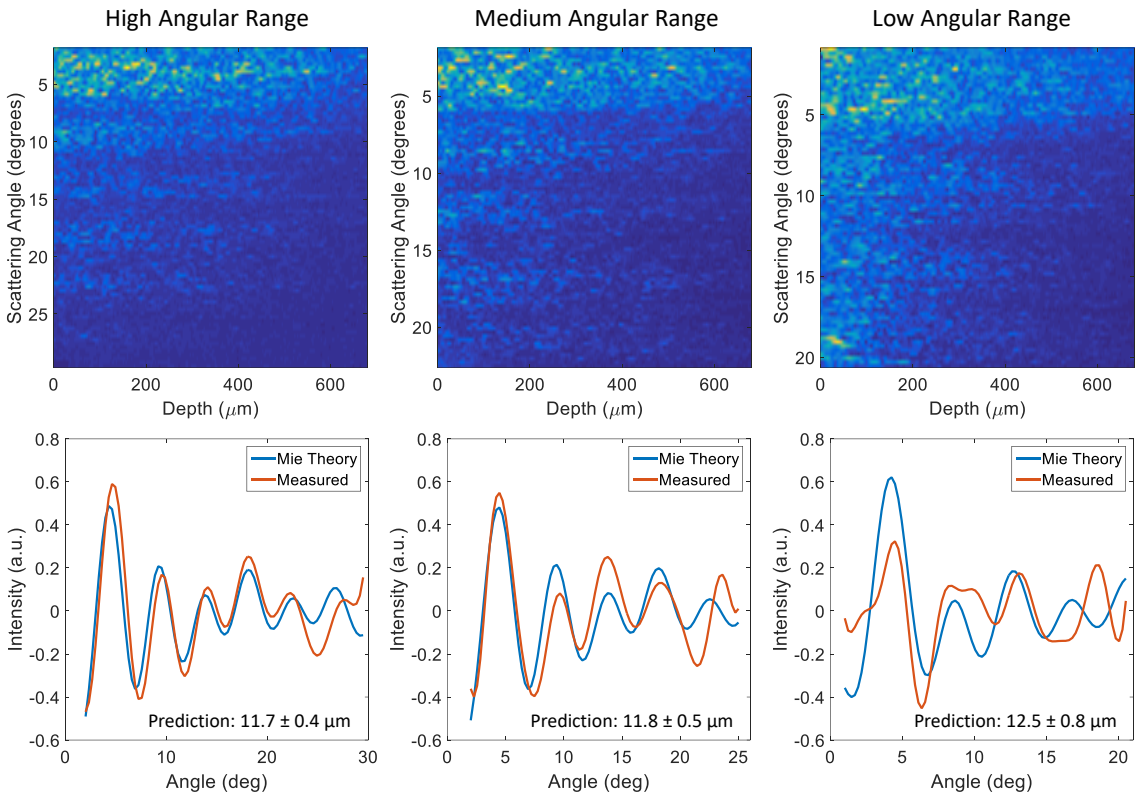

Figure 3.10 Depth-resolved angular scattering profiles (top row) taken from a benchtop scanning a/LCI system of a 12 μm polystyrene bead phantom for a high, medium and low angular range lens configuration. The corresponding angular scattering profile along with the best-fit theoretical profile shown in the bottom row, adapted from [36].

Similarly, the angular collection range was measured as the maximum angular range over which signal from the scattering phantom could be observed on the detector. The three configurations exhibited angular ranges of 27.5°, 23° and 19.5°, with corresponding scan ranges of 8.55, 11.22 and 14.17 mm, respectively. These three points were compared with the theoretically achievable angular ranges as a function of scanning range for the benchtop system (NA = 0.30, 18 mm clear aperture, 400 μm beam diameter), and plotted in Figure 3.11.

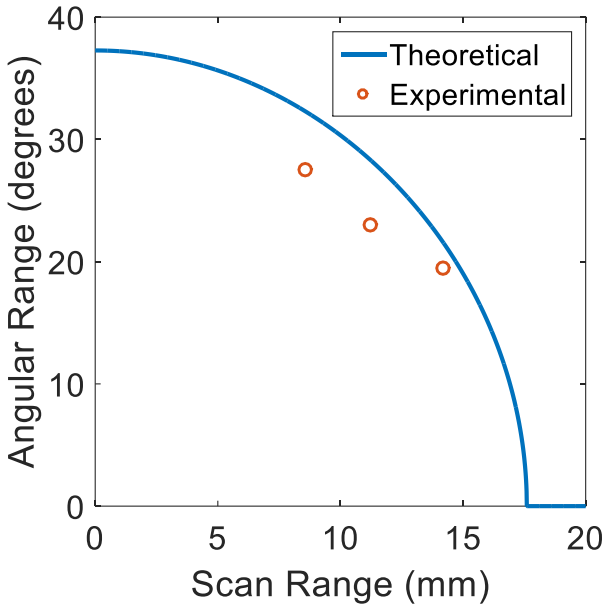

Figure 3.11 Experimentally measured angular collection and scanning ranges for the three lens configurations, along with the theoretical curve describing an ideal system, adapted from [36].

3.4 Implications on Next Generation Probe Design

The ability to distinguish nondysplastic from dysplastic tissue is crucial to the early detection of cancer. As with any diagnostic modality, various a/LCI designs exhibit tradeoffs which may influence diagnostic accuracy. Balancing detection capability with clinical utility, useful features such as scanning capability, and cost will help to create a more useful clinical instrument. The modified a/LCI probe examined in this chapter underscores the significance of this study for the development of future clinical devices. While a scanning a/LCI system would benefit from a large scanning area to provide maximum tissue coverage and surveillance, there exists an unavoidable tradeoff between scanning range on the tissue and the angular collection range of scattered light.

This work has also inspired the development of many other a/LCI systems with optimal design parameters, including 2D scanning a/LCI [28, 129], and also a path-length-matched linear fiber array (PLFA) [125] described in Chapter 6.

As we have shown, the angular range θ_r is an important parameter governing diagnostic capability, with a reduction in θ_r of ~10 (degrees) corresponding to a reduction in diagnostic sensitivity of ~0.2. Fortunately, a simple relationship exists between scanning range and angular range of detected scattering, which may be chosen according to the required diagnostic accuracy. The effects of a reduction in θ_r were apparent in analysis of the experimental measurements shown here, in which angular ranges of 27.5°, 23° and 19.5° corresponded with uncertainty in the microsphere size of ± 0.4 μm, ± 0.5 μm and ± 0.8 μm, respectively. Along with an increase in uncertainty, the accuracy of our measurement was reduced from 0.2 μm to 0.5 μm with a loss in angular range by a factor of 8, demonstrating experimentally that a reduction in angular range leads to increased error and uncertainty in the microsphere size prediction. Minimizing uncertainty in the measured nuclear diameter allows for improved discrimination between healthy and dysplastic tissue sites.

3.5 Summary

In this chapter, I have presented our investigation into modifications to the scattering function in a/LCI, using a clinical dataset of 40 patients undergoing optical and histological biopsy of the cervix. Variations in parameters such as angular range, angular sampling frequency and noise in the scattering function were investigated for

their impact on the diagnostic capacity of a/LCI. The chapter further discussed the practical implications of these findings, using a modified scanning a/LCI probe as an example. These results will lead to improved a/LCI diagnostic performance, and will further allow for clinical adoption.

4 Reconstruction of Angular Scattering Profiles through a Single Multimode Fiber

4.1 Introduction

Endoscopic coherence imaging modalities such as a/LCI utilize coherent fiber bundles, also often referred to as imaging bundles, to transmit the backscattered optical field from the sample to the optical engine. These imaging bundles consist of hundreds of different individual optical fibers stacked together, which can spatially map an optical field from the input plane to the output plane of the bundle. Unfortunately, most fiber bundles perform poorly for coherent imaging applications with mismatched optical path lengths and coherent crosstalk between elements [35]. In addition, they also exhibit low open area ratio (OAR), as OAR determines the percentage of the fiber end face that is capable of transmitting light, and typical imaging bundles have a sparse field of single-mode cores interspersed among a surfeit of space-occupying cladding, as shown in Figure 4.1.

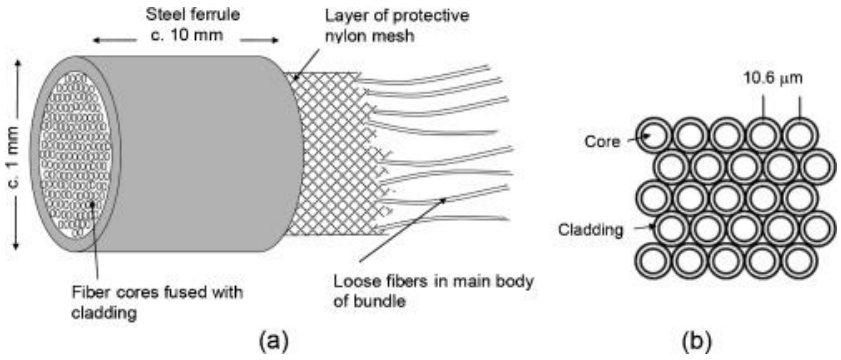

Figure 4.1 Schematic diagram of the input facet of a bare imaging bundle, adapted from [32].

An alternative solution would be to use a single multimode fiber for optical field transmission, as a multimode fiber has improved throughput, simplicity, cost and ability to support more spatial constrained applications due to its small diameter as compared to the imaging bundles. An essential parameter to describe the number of modes capable of being transmitted within the multimode fiber is the V-parameter, which is:

$$V = \frac{2\pi a}{\lambda}\mathrm{NA} \qquad \textbf{(4.1)}$$

where the core radius is a, the wavelength of light in air is λ, and the numerical aperture is $\mathrm{NA} = \sqrt{n_{core}^2 - n_{clad}^2}$. The V-parameter can approximately represent the number of modes which will propagate through the fiber, and this would be approximately $\frac{V^2}{2}$ for large number of modes. Nevertheless, an image cannot keep its original formation after transmission through a multimode fiber, instead forming a distorted image at the distal end of the fiber.

Recent advances have shown various robust image reconstruction techniques to address this multimodal reconstruction problem, including the transmission matrix (TM) method [38, 130-132], machine learning method [133-135], and compressive sensing [136-138]. These methods have proven effective for recovering spatial information computationally with a stationary fixation of the multimode fiber, but reconstruction quality degrades after moving or bending the fiber. Additional acquisition of transmission matrices or computational reconstruction are usually needed to account for the movement of the fiber.

Here in this chapter, we first explore the capabilities of the transmission matrix approach for accurately determining the size of scattering particles based on analyzing scattered light transmitted through a multimode fiber. The method is validated using polystyrene microsphere phantoms and the applicability of this approach for biological media is examined using a sample of MCF-10A human mammary epithelial cells. Then the limitation of this method is discussed, and we propose a new method for reconstructing angular backscattering profiles from the sample by exploiting azimuthal symmetry of the Mie scattering profile.

4.2 Alternative Methods

The most common technique for recovering images transmitted through multimode fibers is the transmission matrix method, where the multimode fiber is treated as a turbid medium, and the input-output response of the multimode fiber is characterized by measuring the transmission matrix for a wide array of spatial delta functions at the fiber's input facet [130-132, 139]. Other methods approach the problem similarly by illuminating the fiber facet with different plane-wave illumination to serve as the reconstruction basis [140]. Despite the success of this method, the major problem of this method is the intensive computational time needed for reconstruction, and the low tolerance to noise due to the ill-posed inverse problem [135]. Many methods tried to focus on faster acquisition of the transmission matrices using rapid-scan galvos mirrors and fast acquisition cameras to compensate for fiber movement [141]. Other methods

focused on averaging speckle pattern to improve the robustness of the reconstructions [142].

A second approach is the compressive sensing method [136-138], which applies the same basic approach as the TM technique, but uses a small subset of the transmission matrix and the assumption of a sparse sample to simplify the reconstruction. While effective and fast, compressive sensing method is limited to highly sparse samples.

Another approach is the machine learning (ML) approach [133, 134, 143, 144], where a deep learning network is introduced to learn the relationship between the original input image and the distorted output image. This method usually uses a spatial light modulator (SLM) or digital micromirror device (DMD) to project thousands of different patterns to serve as input images and collect input-output pairs to serve as the training set of the network, and has been shown to obtain robust image reconstructions. However, reconstruction fidelities degrade when dealing with images outside the training set, even with deep learning frameworks that are designed to focus on the transfer learning from one dataset to another unseen dataset [134]. Many deep learning frameworks are also introduced to generalize over mechanical perturbations of the fiber [133], or provide simultaneous illumination and imaging through deep learning [141].

4.3 Initial Experiment using Transmission Matrix Approach

Here in this section, we fully characterize the transfer function of a multimode fiber using a plane-wave illumination basis, and recover angle-resolved scattering information from the distorted output image scrambled by the multimodal propagation of the fiber. Reconstruction fidelity is validated using a Mie-theory-based ILSA algorithm on polystyrene microsphere phantoms of known sizes. To demonstrate the clinical potential of this approach, our method is further validated to determine the nucleus size of MCF-10A human mammary epithelial cell samples.

4.3.1 System Instrumentation

The system diagram is shown in Figure 4.2. Light from a helium-neon laser ($\lambda = 632.8$ nm) with a power of 7.5 mW is first spatially filtered and directed into either the calibration path (shown in the dark red in Figure 4.2 (a)) for measuring the transmission matrix, or the imaging path (shown in light red in Figure 4.2 (a)) for sample measurement. During calibration stage, a two-dimensional MEMS mirror (Mirrorcle Technologies, Inc., Richmond CA) is used to illuminate the multimode fiber (200 μm core, 0.39 NA, Thorlabs, Inc., NJ) at different input angles. While traditional transmission matrix approaches build the matrices by scanning a point along the fiber face, here we utilize a plane-wave basis by scanning a collimated beam at the fiber facet at different angles, and recording the corresponding distorted image at the distal end of the fiber. In total, 6561 images are recorded, covering an angular range of $\pm 16.2°$ in both θ_x and θ_y direction, with an angular resolution of $0.2°$. During the imaging

stage, the calibration path is blocked, and the sample is placed in the imaging path, where the backscattered photons from the sample are directed into the fiber. The distorted image at the distal end of the fiber is relayed onto the camera (Grasshopper4, Point Grey, 60FPS, 2048 x 2048 pixels/image, with a pixel size of 5.5 μm). Representative calibration images for selected illumination angles are shown in Figure 4.2 (b).

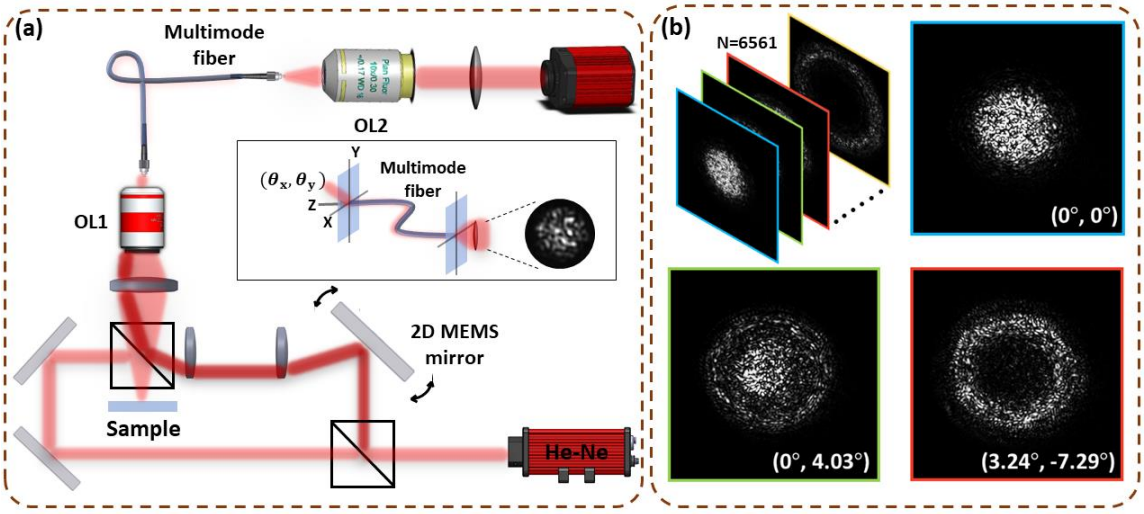

Figure 4.2 Schematic Instrumentation for measuring the transmission matrix of the multimode fiber and representative transmission matrix images, adapted from [38]. (a) Experimental setup for measuring the transmission matrix of the multimode fiber. OL1, OL2: objective lens. The embedded image is a schematic showing the illumination angle (θ_x, θ_y). (b) Representative images at different illumination angles constituting the transmission matrices. Images are displayed with enhanced contrast for clarity.

4.3.2 Transmission Matrix Method

The reconstruction process is shown with an example in Figure 4.3 (a) and (b). The distorted image after transmission through the multimode fiber, shown in Figure 4.3 (a), encodes the angular scattering profile of the microsphere phantoms with a mean diameter of 6.01 ± 0.04 μm. Through a projection operation of the distorted image onto

each angular component of the transmission matrix, the angular spectrum of the target can be retrieved using:

$$A(\theta_x, \theta_y) = \sum A_{trans}(x, y; \theta_x, \theta_y) A_I(x, y) \quad \textbf{(4.2)}$$

where $A_{trans}(x, y; \theta_x, \theta_y)A_I$ is the transmission matrix, and $A_I(x, y)$ is the speckle pattern transmitted through the fiber. A median filter is applied to the raw reconstructed image for noise reduction. Because of the azimuthal symmetry of the backscattering profiles [21], a radial integration is performed from the center of the two dimensional reconstruction to obtain a 1D angular scattering distribution. These steps help to reduce noise arising from the inversion process.

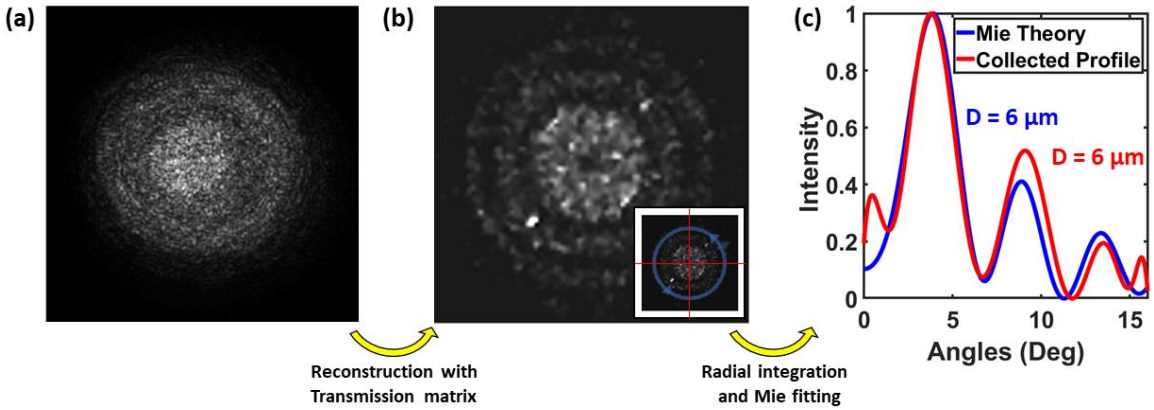

Figure 4.3 Reconstruction pipeline for Mie-theory-based ILSA algorithm, adapted from [38].

Scatterer morphology is then extracted from the reconstruction one dimensional angular scattering distribution using ILSA. A detailed description is discussed in section 2.4.2, where the 1D profile is low-pass filtered and detrended using a second-order polynomial to isolate the oscillatory component of interest. Fortunately, for this

application, this also suppresses speckle noise arising from the inversion. This extracted 1D signal, shown as the red curve in Figure 4.3 (c) is compared with a library of simulated profiles based on Mie theory to find the best fit, shown as the blue curve. This produces a scatterer size prediction for each reconstructed scattering profile.

Here, the Mie scattering library for microsphere phantoms was created using MiePlot with microsphere and medium refractive indices of 1.58 and 1.41 respectively, and including a 1% standard deviation in size distribution for the scatterers. The scatterer diameter was varied between 4 μm and 14 μm with an increment of 0.1 μm to encompass the range of scatterers measured in this chapter's work.

The Mie scattering library for cell nuclei was created similarly, with nuclear and cytoplasmic refractive indices ranging from 1.42 to 1.47 and 1.36 to 1.39, respectively, with a nuclear diameter ranging between 6 μm and 18 μm in increments of 0.1 μm and a range of size standard deviation including 1%, 2.5%, 5%, 7.5%, and 10% variability to account for heterogeneity of sizes in the sample. In total, the libraries contained 101 spectra for the technical phantoms, and 14,520 for cells.

The transmission matrix reconstruction and ILSA were performed using MATLAB R2019a (MathWorks, Inc., Natick, MA). The total time to acquire the transmission matrix was 2.8 min, which consisted of acquiring 6561 images (2048 × 2048 pixels/image) with an integration time of 12.5 ms per image and resting time between images, which allowed the MEMS mirror to settle. Image reconstruction took 12 min, with an average of 120 ms for constructing each transmission matrix. ILSA for a single

image required 290 ms of processing time on a standard desktop computer (Intel(R) Core i7-8700 processors). Statistical analysis was performed using R 3.6.3 (RStudio, Boston, MA).

4.3.3 Sample Preparations and Cell Culture Protocols

The reconstruction results are first validated using polystyrene microspheres (Thermo Fisher Scientific, Microgenics Corporation, Fremont, CA) embedded in polydimethylsiloxane (PDMS), where the polystyrene microspheres were centrifuged and dried to form a pellet, and mixed with PDMS elastomer base and curing agent (Sylgard 184, Dow Corning, Midland, MI) with a pre-mixed ratio of 10:1 by weight in a plastic dish. The samples were left overnight in a vacuum to remove bubbles, and left for 72 h at room temperature to fully cure. Microspheres of 6.0 μm, 8.0 μm, and 10.1 μm were utilized to determine the particle sizing capacity of our system. The PDMS provides a slightly lower refractive index compared with polystyrene microspheres, providing good amount of angular scattering oscillations within the aperture of the system.

To determine our system's capacity for measuring biological samples, immortalized human mammary gland epithelial cells (MCF-10A, ATCC CRL-1031) were cultured in Brugge's media (Department of Cell Biology, Harvard Medical School) consisting of DMEM/F12 (Invitrogen) supplemented with horse serum (Invitrogen), EGF (Peprotech), hydrocortisone (Sigma), cholera toxin (Sigma), and insulin (Sigma). Cells

were maintained at 37 °C with 5% CO2 and 100% humidity according to normal passaging protocols.

In order to provide strong scattering signals from the cell sample, MCF-10A epithelial cells were removed from the culture surface using 0.25% trypsin (GIBCO), which was then deactivated by adding growth media. The sample was transferred to a conical vial and centrifuged to form a dense pellet to provide strong scattering signal from the sample. The supernatant was removed, and the cell pellet was sandwiched between two glass coverslips separated by an adhesive spacer.

To validate the nuclear morphology measurements extracted from our Mie-theory-based ILSA algorithm, image analysis was conducted using fluorescence micrographs. Fluorescence microscopy was performed using a nuclear stain on a ZEISS Axiovert 200 microscope (40×). For these measurements, MCF-10A epithelial cells were plated on a dish (FluoroDish FD5040) seeded at a concentration of 6 × 105 cells/ml. The plated cells were then stained with media containing 3 μM 4′,6′-diamidino-2-phenylindole (DAPI, Thermo Fisher Scientific, Microgenics Corporation, Fremont, CA), and incubated for 10 min at 37 °C with 5% CO2 and 100% humidity. The cell culture dish was rinsed with phosphate-buffered saline (PBS) to remove the residual staining solution. Cells were covered in live cell imaging solution (Thermo Fisher Scientific) prior to imaging, and the nuclear size were measured using ImageJ.

4.3.4 Phantom Validation Study

The initial validation results of microsphere phantoms with a manufacturer verified size of 6.01 ± 0.04 μm, 7.98 ± 0.08 μm, and 10.11 ± 0.06 μm are shown in Figure 4.4. The minimization of the chi-squared error for the different sized beads are shown in Figure 4.4 (a) - (c), and the angular scattering function with the corresponding theoretical best-fit are shown in Figure 4.4 (d) – (f). The red, yellow and green points in Figure 4.4 (a) – (c) indicate that the chi-squared error is minimized at 6.0 ± 0.3 μm, 8.0 ± 0.9 μm and 10.2 ± 0.8 μm., respectively, with the uncertainty determined by the range over which the calculated minimum chi-squared value is doubled [21]. This produces a close prediction for the scatterer's diameter, showing excellent agreement with the size specified by the manufacturer. The angular range from 0° to 16.2° collected by the multimode fiber is sufficient to accurately measure the size of the scatterer, and satisfies the required resolution for diagnostic modalities such as a/LCI [36].

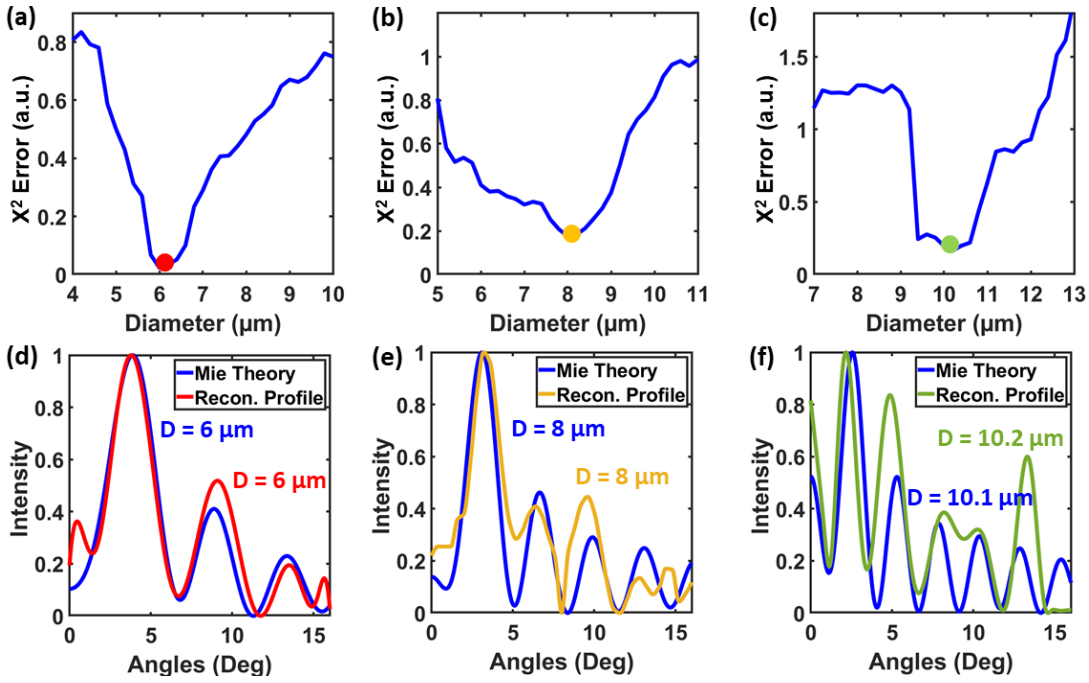

Figure 4.4 Chi-squared error and Mie fitting results for 6, 8 and 10 μm polystyrene microsphere phantoms, adapted from [38].

A calibration curve summarizing all microsphere phantom measurements is shown in Figure 4.5 to demonstrate the reliability of the reconstruction and ILSA results, where each microsphere phantom was measured six times with each measurement occurring at different sites of the phantom to avoid degenerate measurements. The 6.01 μm, 7.98 μm, and 10.12 μm microspheres are accurately measured with averages and standard deviations of 5.90 ± 0.17 μm, 7.90 ± 0.21 μm, and 10.09 ± 0.33 μm, respectively, producing an excellent coefficient of determination (R^2) of 0.964, relative to the line of perfect agreement (blue line). All the measurements fall in the range of sub-wavelength accuracy (within 0.633 μm), shown as the dashed lines in the figure, with a mean error across all measurements of only 0.26 μm.

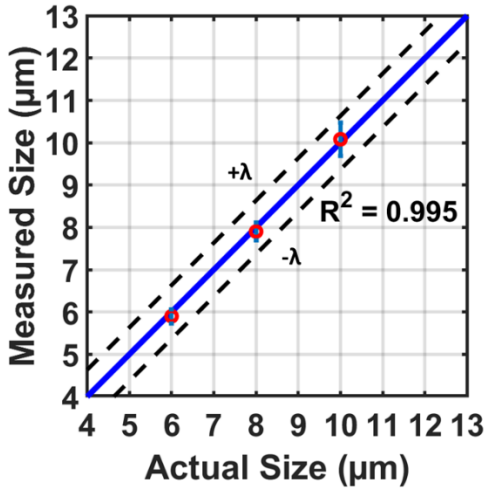

Figure 4.5 Calibration curve demonstrating scattering sizing capability of the system, adapted from [38].

4.3.5 Cell Phantom Validations

In order to demonstrate the capability of measuring nuclear morphology in biological samples, a dense pellet of MCF-10A cells was imaged, and compared with quantitative image analysis (QIA) of its DAPI-stained fluorescence micrographs. The reconstructed 2D angular scattering profile is presented in Figure 4.6 (a), where a clear azimuthal pattern is visually apparent. After locating the center of the angular scattering pattern, an azimuthal integration was applied along the radius. A low-pass filtering followed by a polynomial subtraction was applied to isolate the scattering from the nuclei using a/LCI analysis similar to the process described in previous chapters, and the averaged nuclear size and density is extracted from the best-fitted profile, shown in Figure 4.6 (b), resulting a mean nuclear diameter of 9.63 ± 1.03 μm. The results for the fluorescence micrographs are shown in Figure 4.6 (c). ImageJ (U.S. National Institutes of Health) was used to segment the nuclei, and compute an effective diameter from the cross-sectional area as $2\sqrt{Area/\pi}$. Based on the core size of our fiber and the

magnification of our lens, an averaged scattering distribution from 20 to 30 cells are estimated to be collected through each angle-resolved detection. Therefore, QIA measurements were divided into six different clusters of cells with 25 measurements in each cluster. The mean diameters from each cluster were averaged, and the equivalent diameter of the nuclei was 10.10 ± 0.71 μm, with the uncertainty given by the standard deviation across the six clusters. As seen in Figure 4.6 (d), nuclear sizing based on Mie fitting is in close agreement with the fluorescence microscopy, with a difference between the mean diameter of only 0.47 μm, and no statistical difference between the predicted diameters using a student's t-test ($p > 0.05$). A slight increase was observed from quantitative analysis of the cell measurements compared with Mie theory, which is consistent with results in our previous work.

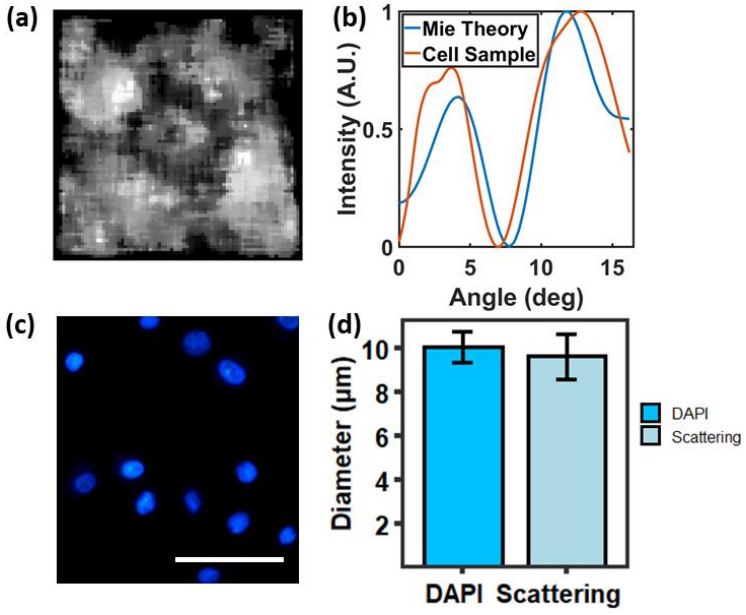

Figure 4.6 Angular scattering measurements and quantitative image analysis of MCF-10A nuclei, adapted from [38].

4.3.6 Limitations of TM approach

Although our system represents an advance for the reconstruction of the angular backscattering, some limitations remain that must be addressed prior to clinical implementation. First of all, physical movement of the fiber including fiber twisting and fiber bending is a major issue for computational imaging, since it severely alters the pre-collected transmission matrix. Our current setup pre-records the transmission matrix with an acquisition time of ~3min, which is too long to incorporate into a scheme for endoscopic surveillance Faster acquisition, reduced sampling of the transmission matrix, and compressive sensing will each help to shorten the time required.

Another limitation that hinders translation of this approach to clinical applications is the computational burden for accessing the large dataset and reconstructing the angular scattering distributions from the speckle patterns. Cameras with on-chip binning options will increase the transfer rate of the pixel data, and speed up the reconstruction process.

Another feature that we can take advantage of is the symmetries and sparsity within the angular scattering distributions. The Mie solution to the Maxwell equations describing the scattering of electromagnetic waves by spherical scatterers, takes the form of an infinite series of spherical Bessel functions, resulting in azimuthally symmetric angular scattering patterns [145]. The transmission of these spherical Bessel functions through a single multimode fiber should also be azimuthally symmetric from observations of the intensity distributions of images in Figure 4.2 (b).

Based on this, a more advanced method for reconstructing the angular scattering profile is proposed in section 4.4.

4.4 Methods

4.4.1 Azimuthal symmetry of Mie Scattering Profiles

Mie scattering theory is the generalized solution that describes the scattering of an electromagnetic wave by a homogeneous spherical medium having refractive index that is different from the medium through which the wave is traversing [124]. The Mie solution takes the form of an infinite series of spherical Bessel functions, and the solution is cylindrically symmetric around the propagation axis of the light [146], and this results in an azimuthally symmetric scattering pattern, which can treated as a superposition of various azimuthally symmetric ring patterns. The transmission of these patterns through a multimode fiber also preserves the symmetry, with an average radius proportional to the size of the input pattern, as shown in Figure 4.7. Additional compensation of the output speckles is needed to extract the input angular scattering distribution.

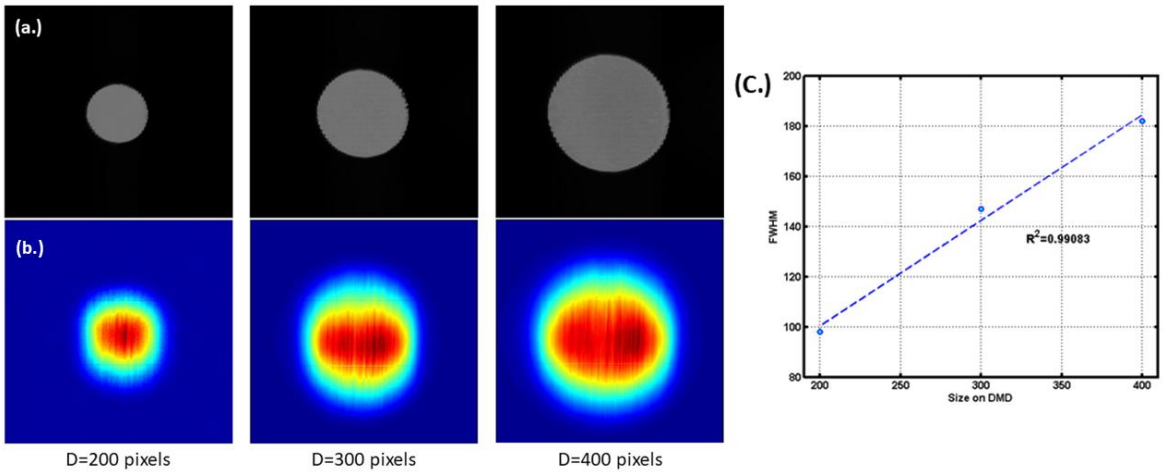

Figure 4.7 Input and output azimuthally symmetric patterns through a single multimode fiber after averaging across wavelength, and the calibration curve.

4.4.2 Instrumentation

In order to resolve the speckle issue and extract the 1D angular scattering distribution, an additional dimension of spectroscopic measurement is introduced to average out the speckles and unlock new types of analysis. The instrumentation schematic for acquiring the three-dimensional information is shown in Figure 4.8. Briefly, a superluminescent diode (Superlum, SLD-371#170095, $\lambda = 840$ nm) with bandwidth of $\Delta\lambda = 50$ nm and an optical power of 18 mW is used as the light source, and the light is first directed onto the digital micromirror device (DMD, Texas Instruments) at an oblique 34 degree illumination angle (shown in solid red lines), where azimuthally symmetric circular patterns of different sizes are displayed on the DMD, as shown in Figure 4.7 (a). The light is then reflected by the "on-state" micromirrors, and guided into the multimode fiber (200 μm core, 0.39 NA, Thorlabs)

using a microscope objective. The output speckle pattern is relayed from the multimode fiber using 4f lens relays, and detected with an imaging spectrometer (Princeton Instruments, SP-2150). The slit of the imaging spectrometer serves to collect the primary axis of the distorted pattern of the angular scattering distribution, as the slit plane is the Fourier plane of the sample. In order to acquire further data in the orthogonal dimension of the beam, a galvanometer is placed in the collection path to scan the beam across the slit of the spectrometer. A 640 × 480 CCD array (AVT, Pike F-032) is used as the sensor for the spectrometer, and synchronized with the galvanometer for near-real-time acquisition of the total spectroscopic spatial profile of the beam.

During the sample imaging stage, a motorized flip mirror (MFF101, Thorlabs, shown in black dashed lines in Figure 4.8) is flipped up to guide the light onto the center of the sample, and the backscattered light is collected and directed into the multimode fiber. The distorted image from the multimode fiber is collected using the same collection path and scanned across the slit of the imaging spectrometer.

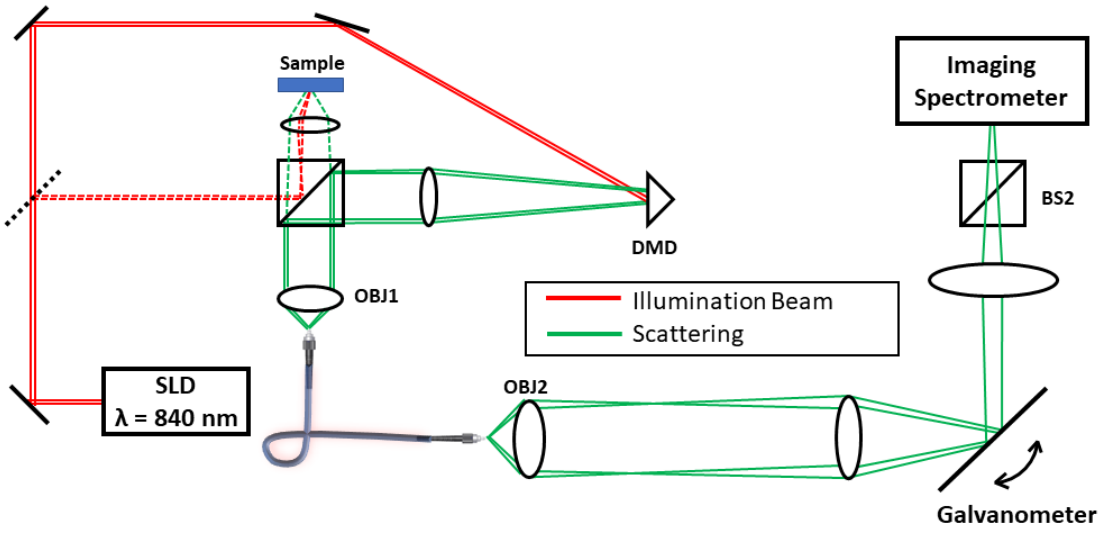

Figure 4.8 Instrumentation setup for reconstructing angular scattering profiles with spectroscopic information through a single multimode fiber.

4.4.3 Data Processing Pipeline

The processing pipeline for recovering the 1D angular scattering distribution from the scattering phantoms is shown in Figure 4.9. The distorted speckle pattern after transmission through the multimode fiber (left of Figure 4.9), encodes the angular scattering profile at different wavelength from 840 nm to 860 nm, with a sampling period of 0.4 nm. Here, speckle patterns at different wavelengths have different maximum intensities due to the spectrum of the light source and the optical throughput of the fiber, so a normalization is applied to all the 2D speckle patterns. Then, after summing across the normalized 2D speckle patterns for all wavelengths, a radial integration is implemented followed by a/LCI analysis, consisting of application of a 2nd order polynomial subtraction is applied to obtain the 1D angular scattering distribution,

shown as the red curve in Figure 4.9. The corresponding best fitting result based on Mie theory is shown as the blue curve.

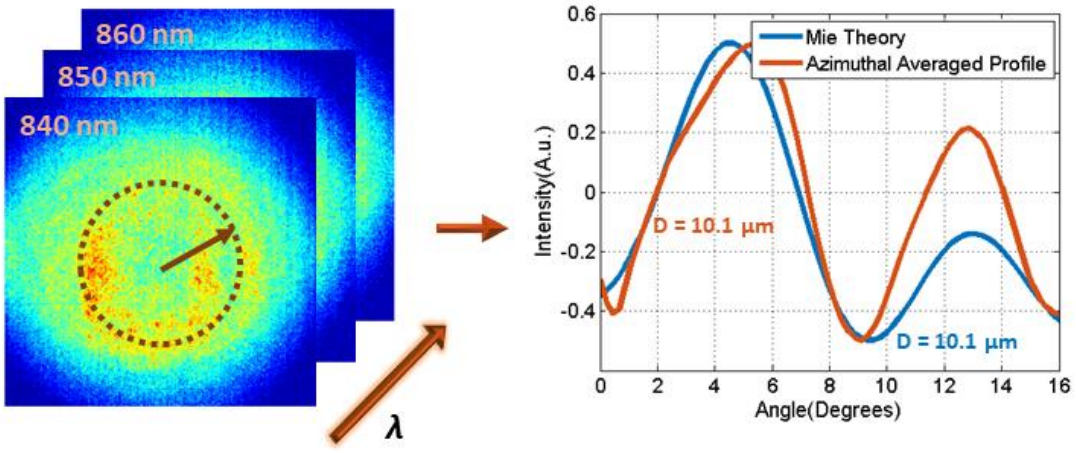

Figure 4.9 Image processing pipeline for recovering the 1D scattering profile from scattering phantoms.

The performance of the reconstruction is evaluated with measurements of two types of polystyrene microsphere phantoms. For the first type, the microspheres are placed directly on a glass dish, and dried out in vacuum. For the second type, the microspheres are suspended in a density-matching mixture of 80% water and 20% glycerol (n=1.36) to produce a liquid-medium microsphere phantom.

Here, the Mie scattering library for microsphere phantoms was created using MiePlot, where the medium's refractive index is set to either 1 or 1.36 based on the type of the phantom. The scatterers size was varied between 4 μm and 14 μm with an increment of 0.1 μm to encompass the range of scatterers measured in this chapter's work, and a 1% standard deviation in size distribution.

4.5 Results

4.5.1 Phantom Microspheres Size Determination

The initial validation results of the angular scattering functions (red curve) of microsphere phantoms in air with manufacturer verified sizes of 4.00 ± 0.04 μm, 6.00 ± 0.08 μm, and 10.11 ± 0.06 μm and the corresponding theoretical best-fit (blue curve) are shown in Figure 4.10 (a), (b) and (c) respectively. The Mie-fitting results for the three different sizes are 4.1 μm, 6.0 μm, and 10.1 μm.

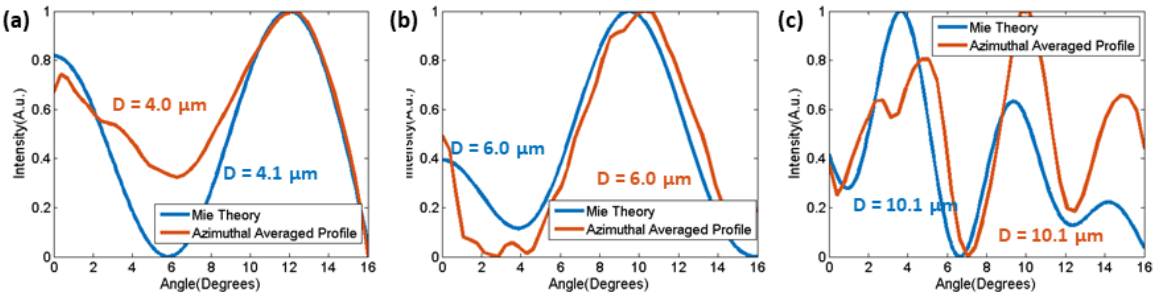

Figure 4.10 Mie fitting results of scatterers with size 4.0, 6.0 and 10.1 μm in air.

A more comprehensive analysis summarizing all microsphere phantom measurements of the two types are shown in the calibration curve in Figure 4.11, where the phantoms in air are shown in red markers, and the phantoms with a mix of water and glycerol are shown in blue markers. To demonstrate the reliability of the reconstruction and ILSA results, each microsphere phantom was measured five times with each measurement occurring at different sites of the phantom to avoid degenerate measurements, and the standard deviations are labeled as the error bar. All the

measurements fall in the range of sub-wavelength accuracy (within 0.840 μm), shown as the light blue regions of the figure.

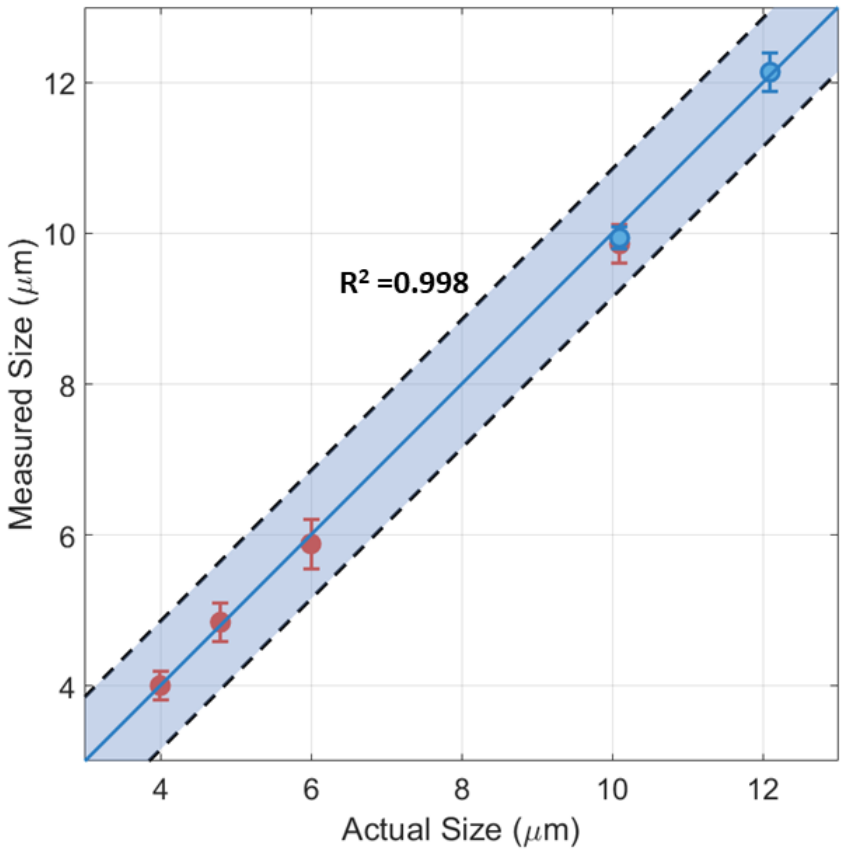

Figure 4.11 Calibration curve demonstrating scattering sizing capability of the system, where the blue symbols represent the phantoms in air, and the red symbols represent the phantoms in mixture of water and glycerol.

4.5.2 Validation of Size Determination during Fiber Displacement

To demonstrate the generalizability of this approach in dealing with fiber bending and natural fiber displacements, the 1 m long multimode fiber is taped down to a flat platform at five different displacement shapes, shown as ① - ⑤ in Figure 4.12, and five measurements were taken for each fiber position to avoid degenerate

measurements. The total variation in movement distance ranges from 10 cm to 30 cm across 5 different positions. The calibration curve showing the measurements is shown in Figure 4.12. Significantly, movement of the fiber does not reduce the accuracy of the measurement, as the mean measured size for each phantom remain in close agreement with the manufacturers size, with a small error bar within subwavelength accuracy, shown as the light blue region bounded by the two dashed lines.

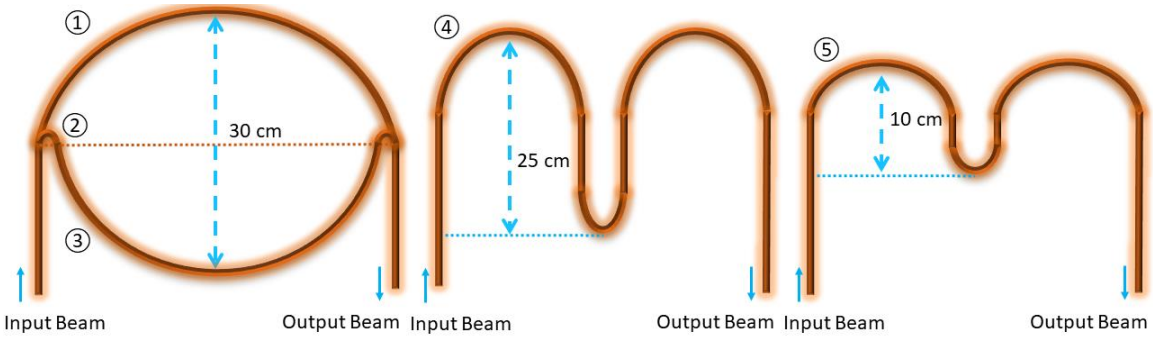

Figure 4.12 Displacement of multimode fiber during measurements of scattering distribution (up to 30cm).

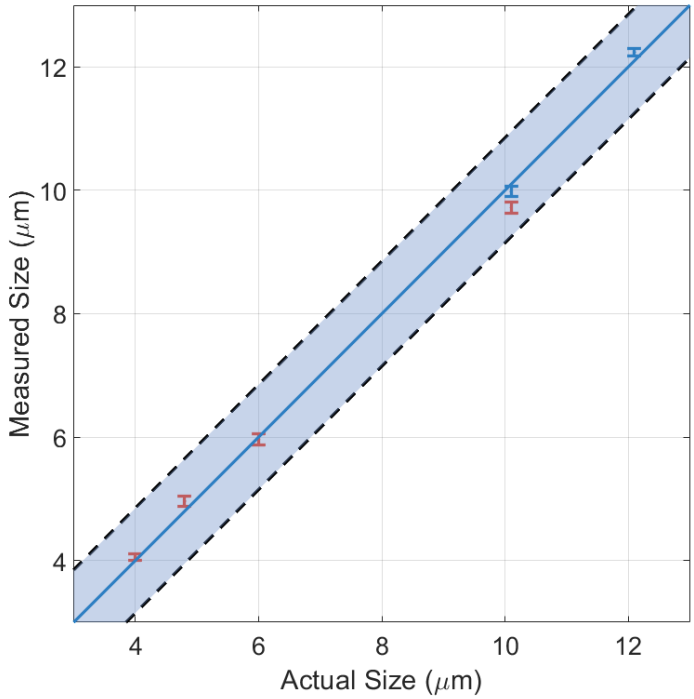

Figure 4.13 Calibration curve demonstrating generalizability across measurements with fiber bending, where the blue symbols represent the phantoms in air, and the red symbols represent the phantoms in mixture of water and glycerol. The error bars indicate the variability in fitting across 5 measurements.

4.6 Implications for Next Generation Probe Design

During the sample imaging stage, the azimuthal symmetry of the angular scattering distribution ensures that it remains static after transmission by the multimode fiber, and speckles were washed out due to the summation of the spectroscopic information and the radial integration process. In our experiment, the angular scattering distribution collected through our setup has an angular range of ±16° in both x and y direction, which is mainly due to the limited numerical aperture of the imaging setup as well as the multimode fiber. A slight blur along the radial direction was observed over the full angular range of the angular scattering field after transmitting through the

multimode fiber, suggesting there is observable crosstalk between radial modes of the multimode fiber. This radial blur is more apparent when imaging larger scatterers (>10 μm) in air, as the angular scattering distributions from larger scatterers have more oscillations within the same angular range. Because of this, 10 μm and 12 μm microspheres are suspended in a density-matching mixture of water and glycerol to produce a liquid-medium microsphere phantom, resulting in a refractive index more similar to that of the scatterer, and in turn producing lower frequency oscillations in the scattering distributions. Nevertheless, the typical angular scattering distributions that are demonstrated in this chapter usually contains two to three oscillations within the given angular range, and this is comparable to that expected from biological scatterers (cell nuclei). Using a multimode fiber with higher NA (higher acceptance angle) would diminish this problem, and thus shows potential for tissue imaging.

A multimode fiber has several advantages over the imaging bundle, including improved throughput, simplicity, cost and ability to support more spatially constrained applications due to its small diameter. This would provide better miniaturization for future a/LCI endoscopic designs, and accessibility to smaller and more constrained anatomical regions. Nevertheless, this current optomechanical optical design described in this chapter is a preliminary benchtop design, and several things need to be considered for in-vivo angular-scattering applications. First, traditional a/LCI usually uses a PM fiber to guide the illumination beam onto the tissue, and a GRIN lens to capture the angular scattering distribution from the tissue, as well as several other

optical components to map this scattering field to the individual elements on the imaging bundle. Here, for simplicity, we illuminated our sample in free space, and directed the angular scattering distribution into the fiber at the proximal end and imaged the speckle pattern at the distal end. Future work would need to focus on an optical design for illuminating and collecting the light both at the proximal and distal ends of the fiber for endoscopic applications. Another challenge is the need for accurate coupling of the angular scattering distribution into the small multimode fiber core, as slight misalignment from the center of the fiber core would result in completely different azimuthally symmetric patterns. Precise alignment and stable mounts are needed for consistency of this approach. Our future work with this approach will focus on incorporating this design into endoscopic optical designs for illumination and collecting of the angular scattering distributions for in-vivo imaging applications.

4.7 Summary

In this chapter, we have demonstrated two methods for reconstruction of angular scattering distributions through transmission of a single multimode fiber. We first utilized a transmission matrix approach and developed an optomechanical system to acquire nuclear morphology measurements using backscattered light. The results from the first study showed accurate size determinations and demonstrated the feasibility of this approach combined with Mie-theory-based ILSA to characterize the size of biological scatterers from the multimode-fiber-collected angular backscattering

distributions. In order to overcome the acquisition and computational complexities of this method, we exploited the azimuthal symmetry of the angular scattering profile to enable direct transmission through the multimode fiber, and developed a fast and accurate approach in reconstruction angular scattering distributions. An optomechanical system was developed and spectroscopic information was recorded using a scanning imaging spectrometer setup. The reconstruction results were validated using microsphere phantoms, and showed excellent agreement with the actual size. These results are also insensitive to the displacement of the fiber, and showed great potential for future endoscopic applications for medical diagnostics. It is expected that improved computational imaging schemes will enable the use of multimode fiber for simple and robust medical diagnostics.

5 Deep Learning Classification of Cervical Dysplasia using Depth-Resolved Angular Light Scattering Profiles

5.1 Introduction

Early detection of cervical cancer screens for precancerous tissue (cervical dysplasia), which ranges in severity from low-grade squamous intraepithelial lesions (LSIL) to high-grade squamous intraepithelial lesions (HSIL). Identification and staging of dysplasia are crucial in preventing the progression of malignancy and improving patient outcome, with the severity of dysplasia drastically influencing treatment strategies. a/LCI, as described in previous chapters, is a promising technique which offers unique capabilities of extracting depth-resolved nuclear morphology information at or near the basal layer of the cervical epithelium using an inverse light scattering analysis (ILSA) algorithm based on Mie theory. Although Mie theory-based ILSA is an effective technique for classifying epithelial tissue based on nuclear morphology parameters, the technique is currently limited by excessive data processing time, ~ 25 seconds per optical biopsy [27]. For proper computation, current a/LCI processing involves an iterative process in which sample data is compared to a database of known Mie scattering profiles [36]. Further, a/LCI scans using ILSA-based processing require a calibration step that involves summing the a/LCI data at all angles as a function of depth to determine the start of the epithelium in the depth scan. Not only is there a constant offset of tissue start depth that depends on the instrument's optical path, but variability in probe placement with the cervix, and the presence of overlying mucus requires minor

adjustments to be made across patient scans, adding substantially to overall processing times. Previously reported methods aimed at improving a/LCI processing include using a continuous wavelet transform [30] and T-matrix [90] based approaches, however both suffer from substantial trade-offs in terms of processing accuracy and speed respectively. Ideally, processing should take under one second to provide instant feedback to clinicians and to limit the total time of an imaging session.

In recent years, deep learning techniques have advanced the state-of-the-art for a variety of image classification tasks. One particular family is convolutional neural networks (CNNs), which implement a series of transforming layers to extract features directly from training data. CNN shows great potential in tandem with many optical imaging techniques to achieve rapid, high-accuracy classification including quantitative phase imaging, optical coherence tomography, fundus photography, and fluorescence microscopy. Recently, several machine learning methods have focused on analyzing light scattering from cells. Wan *et al.* introduced a pretrained CNN to classify label-free cell light scattering patterns [147], and achieved good classification results. Another work from Sun *et al.* developed a neural network which was trained on big-data two dimensional (2D) light scattering patterns from single cells based on microfluidic cytometry [148]. a/LCI is also well-suited for machine learning based approaches because of the abundant information provided within each depth-resolved angular scattering dataset, and the depth-resolved information can also provide better clinical utility for in-vivo diagnosis.

In this chapter, a deep learning method, adapted from [37], is introduced. The CNN was developed and trained on a/LCI angle vs. depth scattering profiles of benign, LSIL, and HSIL tissue for rapid classification of cervical epithelium. The a/LCI dataset is comprised of raw a/LCI scans from two previous clinical studies that assess cervical dysplasia in vivo: one study was designed to evaluate a point-probe a/LCI instrument and the other a multipoint scanning a/LCI instrument. Training was performed only on a/LCI scans from the point-probe a/LCI study and tested on a/LCI scans from both the point-probe a/LCI study and the scanning a/LCI study. Using a CNN-based approach for a/LCI processing, high accuracy, increased processing speeds, and generalizability across different instruments are demonstrated as a powerful tool that can improve the clinical feasibility of using a/LCI to detect cervical dysplasia.

5.2 Methods

5.2.1 Clinical Datasets

The two datasets used here consist of depth-resolved angular scattering scans of the cervical epithelium acquired during two separate clinical studies using two different a/LCI instruments [27, 28]. Each a/LCI scan is a two-dimensional map of angular scattering distribution as a function of depth within the tissue, and an example of an a/LCI scan is shown on the left of Figure 5.1. In both clinical studies, the physical locations of the optical biopsies were predetermined by the instrumentation to specific quadrants of the cervix. Colposcopy immediately followed a/LCI data collection, and co-

registration using tissue marking or white light imaging allowed for the identification of each specific site for acquisition of physical biopsy. Four separate optical biopsy sites were acquired and analyzed by a pathologist blinded to the Mie theory-based a/LCI optical biopsy results for each patient. These pathological results were set as ground truth for the CNN with possible classifications of benign, LSIL, and HSIL.

Dataset A, collected by a point-probe a/LCI, consists of 6660 individual scans collected from 40 patients, which includes 3260 scans collected from 33 benign biopsy sites, 2040 scans from 17 LSIL biopsy sites, and 1360 scans from 13 HSIL biopsy sites. Dataset B is collected via scanning a/LCI, where multiple scans were acquired in one imaging session. This device also included an onboard white light camera to visualize the cervix and enable better registration with physical biopsies. This set consists of 1600 individual scans collected from 20 patients, including 980 scans collected from 49 benign biopsy sites, 380 scans from 19 LSIL biopsy sites, and 240 scans from 12 HSIL biopsy sites. Altogether, 60 different patients were involved in this study. The scans from dataset A were cropped down from an angular range of 30.2° to 20.8° and interpolated to match the angular sampling of dataset B to match the angular range between the dataset training dataset A and the test of dataset B.

For both studies, each patient was under voluntary informed consent and approved by the Institutional Review Boards (IRB) of Duke University and either the University of California, San Francisco, or Albert Einstein College of Medicine, . A more detailed description of each clinical study's protocols and ethical standards is

provided by Ho *et al.* [27] and Kendall [28] *et al.*, respectively. The data used in this study were de-identified before analysis.

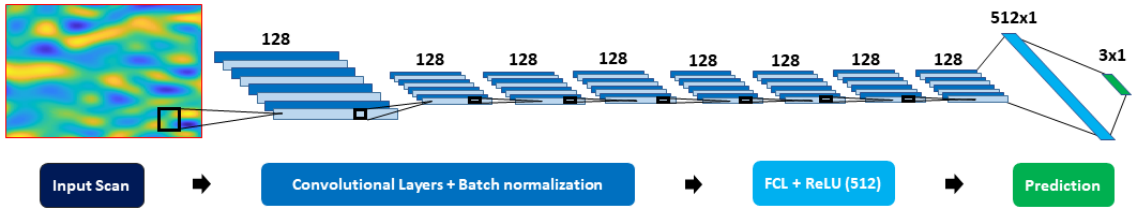

Figure 5.1 Visual representation of the convolutional neural network architecture, adapted from [37]. Raw depth-resolved angular scattering profiles are input to the networks, with layer stacks of generated feature maps notated by the number of features.

5.2.2 Convolutional Neural Network Model

The algorithm was developed using a standard CNN architecture based on eight convolutional layers, with a batch size of 50 used for training. Results were reported using Adam optimization [149] with a step size of 10^{-3}, and coefficients of $\beta_0 = 0.9$, $\beta_1 = 0.999$ and $\varepsilon = 10^{-8}$. The architecture is visually represented in Figure 5.1. Each depth resolved angular scattering scan with the size of 10×69 (depth $\times$ angle) serves as inputs of the network. Layer one and layer two use 3×3 convolutional kernels with 128 features, a rectified linear unit (ReLU) as the activation function, and a stride of two for down sampling. Layer three through eight use a 1×3 convolutional layer with 128 features, and a ReLU activation function. Layer nine is a densely connected layer with 512 neurons and RELU activation function, followed by a densely connected readout layer for the three different classifications. Training and data analysis were processed on

a desktop computer with i7-8700 CPU at 3.2 GHz, 32 GB of RAM, and a GeForce RTX 2070 Super GPU.

5.2.3 Data Processing for Deep-learning-based Algorithm and Traditional Mie-theory-based ILSA Algorithm

k-fold cross-validation (*k*=32) was first used to assess the predictive power of the CNN. Dataset A consists of 6660 different depth-resolved angular scattering scans randomly partitioned into 32 subsets, where 31 subsets were used as the training dataset to create a learned network model and the remaining subset used as a testing set to measure the network's performance. This analysis was repeated until all 32 subsets were used once as a testing set. The average performance of the model was reported using ten rounds of cross-validation with new randomly partitioned subsets to minimize variability. The classification results were then dichotomized using the two approaches used in the original study: a histologic dysplastic (LSIL & HSIL) versus non-dysplastic dichotomy based on morphological distinction and a clinical HSIL versus LSIL/benign dichotomy based on clinical treatment paths. Finally, majority voting based on all scans from each biopsy site was introduced to create an overall prediction for the given biopsy site to determine sensitivity, specificity, PPV, and NPV. The workflow of this training approach is shown in Figure 5.2.

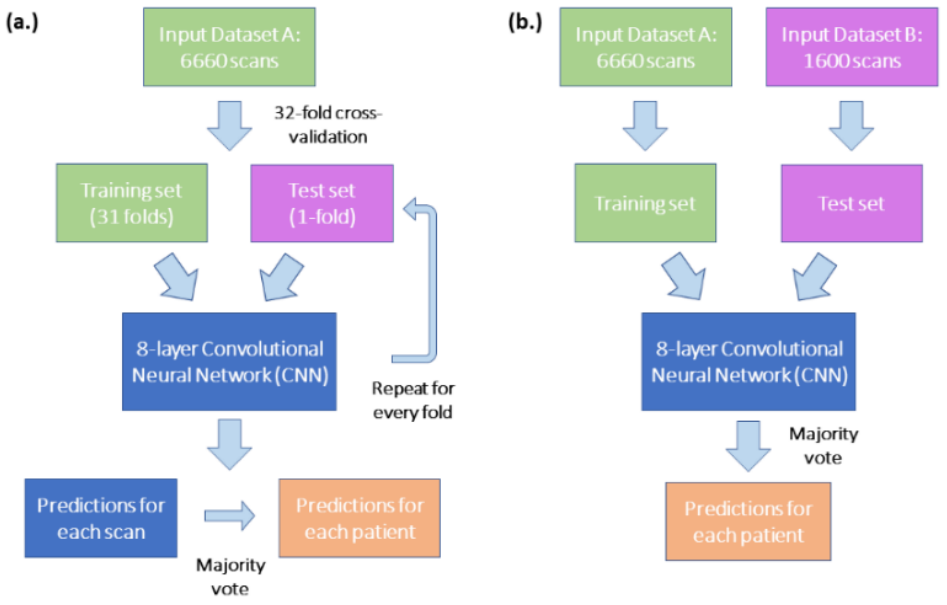

Figure 5.2 Workflow of the two CNN training approaches for the automated classification of cervical dysplasia using 8260 clinical a/LCI scans, adapted from [37]. (a.) dataset A used as the training and test set. (b.) Dataset A used as the training set and dataset B as the test set.

The scans in dataset A were cropped and interpolated to match the angular range of dataset B. Dataset A was used explicitly as training data to create a learned network model to identify dysplasia across different a/LCI instruments. Network performance was evaluated using dataset B to assess the generalizability of the network. The classification results are dichotomized using the same two approaches as above. Thresholding values for each prediction were to determine the sensitivity, specificity, PPV, and NPV of the network in identifying dysplasia (HSIL/LSIL) or HSIL for each biopsy site. The workflow of this training approach is shown in Figure 5.2.

Results of the machine learning approach were compared with the traditional ILSA approach based on Mie-theory, where the corresponding sensitivity, specificity, PPV, NPV, as well as the overall accuracy are derived accordingly.

Testing and training of the CNN were performed using TensorFlow 2 (Google Inc, Mountain View, CA). Statistical analyses were performed using MATLAB R2019A (MathWorks, Inc., Natick, MA).

5.3 Results

5.3.1 Assessment of Network's Classification Performance

Figure 5.3 summarizes the CNN classification performance for distinguishing individual benign, LSIL and HSIL angular scattering scans across ten rounds of 32-fold cross-validation. The average training time for each fold is 96.2 ± 1.2 seconds over 100 epochs. Figure 5.3 (a) shows the classification accuracies for each stage of cervical dysplasia. The histopathological analysis results were set as ground truth and represented in the left column. The prediction score for each identity is listed along the rows of the confusion matrix. The colormap of the confusion matrix is shown on the right, where the matrix elements corresponding to darker colors represent higher classification accuracies. The diagonal arrangement of the higher classifications scores highlights the correct classifications, showing that the CNN is good for distinguishing the three classes using single biopsy scans (91.96%, 89.5%, and 86.9% respectively for classifying benign, LSIL, and HSIL), with an overall scan-level accuracy above 90%. For visualization purposes, Figure 5.3 (b) presents the classification results graphically in stacked bar plots, where the three classes benign LSIL and HSIL are represented as blue, orange, and yellow-colored bars, respectively.

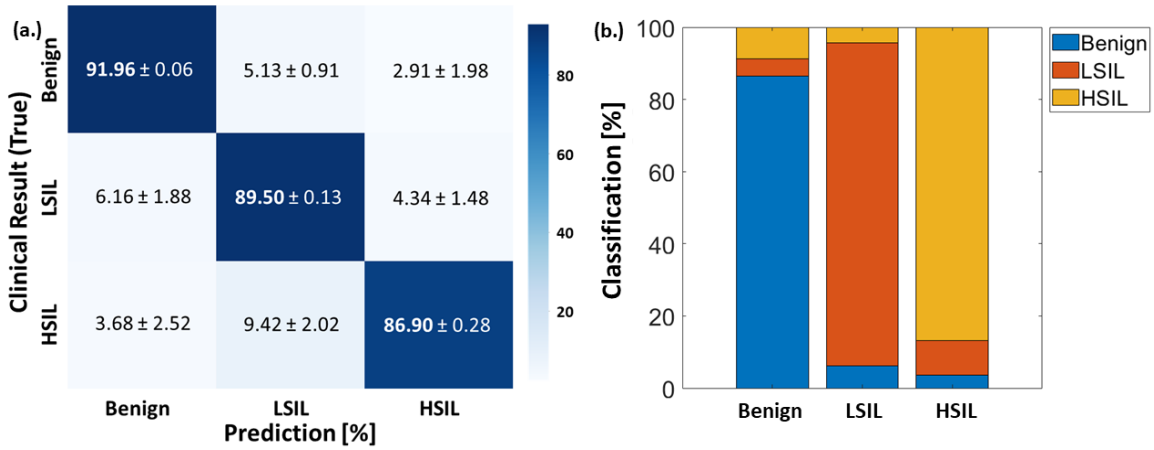

Figure 5.3 Classification performance of a CNN-based approach for the grading of cervical dysplasia using 8260 clinical a/LCI scans, adapted from [37].

The obtained predictions for each scan were then dichotomized based on histological classification and clinical classification, using the same dichotomization illustrated in [27]. The ability of the algorithm to identify dysplasia (LSIL/HSIL) and high-grade dysplasia (HSIL) based on the two approaches can be illustrated by calculating the sensitivity and specificity, shown in Table 5.1. Overall, the network offered high sensitivity and specificity for detecting LSIL/HSIL (94.8% and 92.0%, respectively) and HSIL (86.9% and 96.5%, respectively). Based on the histological classification, the high sensitivity and NPV value (94.8% and 94.4%, respectively) indicate that false-negative outcomes are rare where dysplasia or HSIL are incorrectly classified as benign. For the clinical classification, lower sensitivity and PPV (86.9% and 85.7%, respectively) were observed compared with that for the dysplastic vs. non-dysplastic dichotomization.

Table 5.1 Performance of the convolutional neural network for identifying dysplasia (LSIL/HSIL) or HSIL.

Stage (Number of scans)	**Histological Classification LSIL/HSIL (3400) *vs.* Benign (3260)**	**Clinical Classification HSIL (1360) *vs.* Benign/LSIL (5300)**
Sensitivity [%]	94.8	86.9
Specificity [%]	92.0	96.5
PPV [%]	92.5	85.7
NPV [%]	94.4	96.8

An overall prediction for each biopsy site was generated by performing majority voting of all the scan predictions at each given biopsy site to compare the machine learning algorithm's performance with the original Mie theory-based ILSA algorithm [27]. Here we first assess the ability of our machine learning approach to identify dysplastic (LSIL/HSIL) biopsy sites (Table 5.2). The network predictions based on majority voting offer high sensitivity, specificity, PPV, and NPV (100%, 94%, 94%, and 100% respectively), which is comparable to that using Mie-theory (100%, 97%, 97%, and 100% respectively). For distinguishing HSIL from benign/LSIL biopsy sites, show in the bottom of Table 5.2, the network results based on majority voting produced a sensitivity of 85%, a specificity of 90%, a PPV of 69%, and an NPV of 96%.

The major advantage is the increased data processing speed, where data processing times are calculated using 1000 depth-resolved angular scattering profiles. The average time for each profile and each biopsy site was calculated accordingly. For example, Mie theory-based ILSA required an average of 235 ms to process each profile

and approximately 23 s per biopsy site (based on averaging 100 scans from the same patient). The machine learning algorithm realized a 100-fold increase in processing speed, achieving an average processing time of 2.23 ms per profile and 0.24 s per biopsy site (based on majority voting of 100 scans from the same patient).

Table 5.2 Performance comparison between the CNN and Mie-theory based ILSA for identifying dysplasia (LSIL/HSIL) or HSIL using the point-probe a/LCI data as the test set

Dysplastic (LSIL/HSIL, n=30) *vs.* Non-Dysplastic (Benign, n=33)		
	Machine Learning Approach	Mie-theory based ILSA
Sensitivity [%]	100 (30/30)	100 (30/30)
Specificity [%]	94 (31/33)	97 (32/33)
PPV [%]	94 (30/32)	97 (30/31)
NPV [%]	100 (31/31)	100 (33/33)
Accuracy [%]	97 (61/63)	98 (62/63)
High risk (HSIL, n=13) *vs.* Low risk (Benign/LSIL, n=50)		
	Machine Learning Approach	Mie-theory based ILSA
Sensitivity [%]	85 (11/13)	100 (13/13)
Specificity [%]	90 (45/50)	82 (41/50)
PPV [%]	69 (11/16)	59 (13/22)
NPV [%]	96 (45/47)	100 (41/41)
Accuracy [%]	89 (56/63)	86 (54/63)
Processing Time: (ms/profile)[1]	**2.23**	240.7
(s/biopsy site)[1]	**0.24**	25

[1]Based on majority voting (machine learning approach) or averaging (Mie-theory-based ILSA) of 100 depth-resolved angular scattering profiles from the same patient.

5.3.2 Assessment of Network's Generalizability across Different a/LCI Instruments

To assess generalizability across systems, the approach is applied by training and testing on datasets collected from two different instruments to mirror the design of the prospective study [28]. Dataset B, obtained from the scanning a/LCI instrument [28], was tested using the network pre-trained on dataset A. ROC curves were determined based on each of the two dichotomizations, shown in Figure 5.4, where the red curves represent the ROC curve from the machine learning approach, and the blue curves represent the ROC curve from the Mie-theory-based analysis of original clinical study. For dysplastic versus non-dysplastic, the ROC analysis resulted in an area under the curve (AUC) of 0.932 (Figure 5.4 (a)) compared to an AUC of 0.884 using Mie theory-based ILSA. The optimal threshold produced sensitivity and specificity of 90.3% and 85.7%, respectively, compared to 90.3% and 81.6%, respectively, for the Mie-theory ILSA algorithm. For the machine learning algorithm to distinguish HSIL versus benign/LSIL biopsy sites, the ROC analysis produced an AUC of 0.853 (Figure 5.4 (b)), a sensitivity of 91.7%, a specificity of 77.9%, PPV 44.3%, and NPV of 98.2%. This was then compared against the Mie theory ILSA algorithm, yielding an AUC of 0.846, sensitivity of 100%, a specificity of 70.6%, PPV of 37.5%, and NPV of 100%. The full analysis for each dichotomization is presented in Table 5.3.

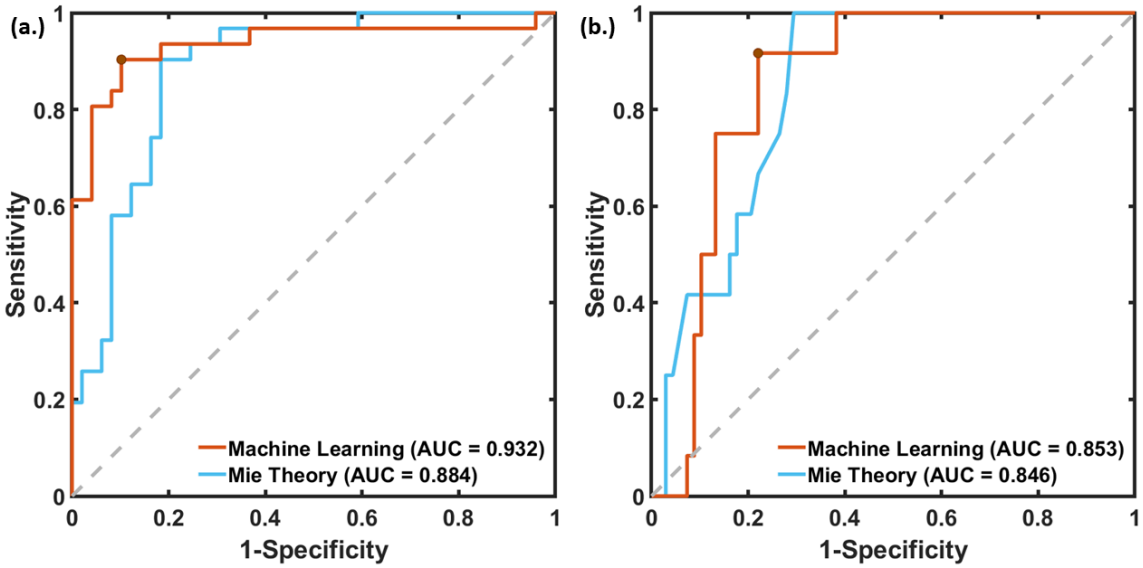

Figure 5.4 ROC curves for both the machine learning approach and Mie theory-based ILSA algorithm for biopsies dichotomized as (a.) dysplastic versus non-dysplastic and (b.) HSIL versus benign/LSIL, adapted from [37].

Table 5.3 Performance comparison between the CNN and Mie-theory based ILSA for identifying dysplasia (LSIL/HSIL) or HSIL using the scanning a/LCI data as the test set

Dysplastic (LSIL/HSIL, n=31) *vs.* Non-Dysplastic (Benign, n=49)		
	Machine Learning Approach	Mie-theory based ILSA
Sensitivity [%]	90.3 (28/31)	90.3 (28/31)
Specificity [%]	85.7 (42/49)	81.6 (40/49)
PPV [%]	80.0 (28/35)	75.6 (28/37)
NPV [%]	93.3 (42/45)	93.0 (40/43)
Accuracy [%]	87.5 (70/80)	85.0 (68/80)
High risk (HSIL, n=12) *vs.* Low risk (LSIL/Benign, n=68)		
	Machine Learning Approach	Mie-theory based ILSA
Sensitivity [%]	91.7 (11/12)	100 (12/12)
Specificity [%]	77.9 (53/68)	70.6 (48/68)
PPV [%]	42.3 (11/26)	37.5 (12/32)
NPV [%]	98.2 (53/54)	100 (48/48)
Accuracy [%]	80.0 (64/80)	75.0 (60/80)

5.4 Discussion

Using a CNN to classify the severity of dysplasia in the cervix based on a/LCI scattering data was successful with comparable performance and superior speed and generalizability compared to ILSA. The overall accuracy of the machine learning approach was high when considering only data from the point-probe study with 97% accuracy attained by the CNN in the histological (dysplastic vs. non-dysplastic) case compared to 98% from ILSA and 89% accuracy from the CNN in the treatment-based dichotomy (benign + LSIL vs. HSIL) vs. 86% from ILSA. Future work will involve adjusting initial parameters of the ROC curve to maximize clinical utility by being weighted towards higher sensitivity.

The increased generalizability of using the CNN over ILSA shows great clinical advantage. During the ILSA process, an instrument-specific low-pass filtering and recalibration of tissue start depth is required between each patient, which introduces substantial processing complexity and time. This hinders the clinical utility of a/LCI, especially if it were to be employed at scale. On the other hand, the CNN, when trained on the point-probe a/LCI data and tested on the scanning a/LCI, performed very similarly to that of the ILSA-based prospective study using scanning a/LCI, with the CNN achieving an overall accuracy of 87.5% in the histological case vs. 85% from ILSA, and an accuracy of 80% in the treatment-based case compared to 75% from ILSA. The LDA-based classification line used in the prospective ILSA-based study was also weighted to maximize sensitivity, producing similar variations in sensitivity, specificity,

PPV, and NPV compared to those observed in the point-probe a/LCI data when classified using the CNN.

The overall lower accuracy of the scanning a/LCI instrument compared to the point-probe a/LCI instrument mainly was because it was a prospective study using a previously established decision line. However, there were also differences in the patient cohort, where the scanning a/LCI was used in a patient population with a known diagnosis of dysplasia or other cervical diseases. The greater prevalence of dysplasia in the second study can produce skewed measurements where a lesion in one region of the cervix can influence the overall health of the cervix due to inflammation or the field effect of carcinogenesis [150]. The reduced performance using the scanning a/LCI instrument as seen from both the CNN classification and ILSA gives some credibility to this idea; corroboration of the CNN results with ILSA would imply it is less likely that the slightly weaker performance was due to flaws in instrumentation. Indeed, light scattering studies has observed evidence of the field-effect previously [151]. However, the comparable level of accuracy seen with the CNN, which avoids the need to individually calibrate scans between patients or instrumentation, as needed for ILSA-based analysis, points to a much greater universal application of a/LCI; future studies investigating dysplasia using a/LCI will likely use deep learning in conjunction with or even in place of ILSA for classification.

A great improvement in processing speed was observed using CNN-based methods. Traversing through the Mie library database and iteratively comparing each

theoretical Mie scattering profile to a given scan is computationally intense and amplified by the number of repeated scans generally necessary to obtain averaged nuclear morphology information at each given biopsy site. Previous methods including the hybrid algorithm method [26] were introduced to reduce the database search range and decrease computational time, resulting in a processing speed of 73.2 milliseconds per profile, which was a threefold improvement compared with ILSA with a slight trade-off of accuracy. Here, the CNN requires 2.23 milliseconds per profile to produce a classification result for each scan vs. 235.4 milliseconds using ILSA, representing an over 100-fold improvement versus ILSA processing time alone while achieving comparable accuracies. Rapid classification of tissue in conjunction with the obviation of a calibration step presents the possibility of real-time cervical dysplasia diagnosis due to a/LCI.

Although our results already show an advance for cervical dysplasia detection with increased speed and comparable accuracy, some limitations remain that must be addressed before clinical implementation. One limiting factor that would influence the clinical utility is the presence of unanalyzable scans due to low signal quality during signal acquisition. Mie theory-based algorithms overcome these by setting thresholds during the $\chi 2$ analysis step to exclude nonunique scans or the scans that have higher $\chi 2$ error than a "null-solution" scan [29]. However, these cannot be excluded in the same way using a CNN, and mislabeling an unmeaningful scan as benign or diseased would result in misclassified results during predictions. Therefore, the current study was able

to use only scans which already cleared the threshold. Another parameter that would influence the diagnostic accuracy is the angular range. For this analysis, we used an angular range of 20.8 degrees for each depth-resolved angular scattering profile. This was the physical limitation of the scanning a/LCI system, which was reduced during design to enable increased scan range in turn surveillance coverage of at-risk tissue. Future work will optimize parameters such as angular range and sampling to improve the network's classification performance [36]. Finally, diagnostics based on a/LCI in other tissue sites, such as detection of esophageal or colorectal dysplasia, will benefit from using deep learning for processing. A more general processing method that can be generalized to any a/LCI instrument and across tissue sites would significantly improve the clinical utility of a/LCI in detecting dysplasia.

5.5 Summary

The work presented in this chapter demonstrates the first use of deep learning to identify disease state of tissue using raw a/LCI light scattering data and demonstrates that its performance is comparable to that of the Mie-theory-based gold standard of inverse light scattering analysis while being faster and more generalizable across different patients or a/LCI instruments.

6 Design and Validation of a Combined a/LCI and Endoscopic OCT Device for Comprehensive Screening of Esophageal Dysplasia

6.1 Introduction

In this chapter, my work is presented on adapting and validating a clinical system that combines: wide area imaging, with optical coherence tomography (OCT) to visualize esophageal epithelial tissue with high resolution, and depth-resolved measurements of nuclear morphology, using a/LCI to provide highly sensitive and specific detection of esophageal dysplasia.

Previous chapters have shown that a/LCI can detect dysplasia with high sensitivity and specificity. However, as a standalone modality, a/LCI is somewhat limited for clinical screening of BE tissues as traditional a/LCI has only been implemented as a point modality. Even with advanced scanning techniques being implemented [28, 127], it is impossible to map the total area of the esophagus. To address this limitation, we aim to expand the clinical utility of a/LCI by incorporating image guidance using OCT to target abnormal tissue. OCT can provide micron scale, cross-sectional tissue image, and can discriminate metaplastic BE tissues from typical squamous epithelium, but with less accuracy in detecting dysplasia compared with a/LCI. In this chapter, a combined miniaturized optical probe is introduced with a rotational endoscopic OCT fiber-probe accompanied with a side-viewing a/LCI probe. As discussed in previous chapters, traditional clinical a/LCI devices which use coherent

fiber bundles suffer from problems including reduced SNR, poor optical throughput (10-20% per meter), poor mechanical stability, and relatively high cost (~$1000 per meter).

In this chapter, a novel a/LCI device is constructed using an array of pathlength-matched single mode fibers and a 3D-printed probe containing micro-lenses. The endoscopic OCT device is discussed, along with results of a pilot clinical study of 30 patients to demonstrate its effectiveness. Then, a clinical study is performed using this combined a/LCI-OCT instrument. OCT images of esophageal epithelium were acquired along with co-registered a/LCI data undergoing routine upper GI endoscopy from 31 patients. We aim to demonstrate the advances of combining real-time OCT imaging guidance with a/LCI for fast and accurate coverage of large at-risk tissue surfaces, offering improved clinical utility.

6.2 Dual-modality Paddle Probe for Combined a/LCI and OCT

In section 6.2.1, we introduce the design of a paddle-based rotational OCT device for *in vivo* human esophageal imaging, along with results of a pilot clinical study of 54 patients to demonstrate its effectiveness. In addition to this, we introduce a newly developed algorithm for segmentation of the epithelium in human esophageal OCT images, and its potential for clinical applications. Next in section 6.2.2, we introduce the design of a paddle-based a/LCI device, including the design of an array of pathlength-matched linear fiber array (PLFA), the optical design of a/LCI paddle, the optical engine, the CAD design of a paddle for the combined a/LCI-OCT system, and validation experiments on microsphere phantoms.

6.2.1 Endoscopic OCT Device

6.2.1.1 Device and Image Processing

An endoscopic OCT device was constructed based on a rotary probe design, and described in detail in [152]. Briefly, the device is based on an interferometric setup, and uses a fiber-optic rotatory junction (FORJ) to allow the optical elements within the probe to spin freely, and collect side-viewing B-scans. The probe was paddle-shaped and designed to be attached to the tip of the endoscope, as shown in Figure 6.1. The housing was 3D printed using a biocompatible dental-grade resin (FormLabs, Somerville, MA). A flexible cuff for attachment to the endoscope was 3D printed using silicone (Carbon 3D, Redwood City, CA), and an anti-reflective rectangular sapphire optical window (Guild Optics, Amherst, NH) was attached to the paddle. Inside the paddle, the probe which consists of a single-mode optical fiber inside a steel torque coil, is positioned such that the optical fiber and the associated micro-optics on the top, including a custom fabricated GRIN (GRINtech, Jena, Germany), a glass ferrule and 1mm AI coated prism, rotate freely, as shown in Figure 6.1 (c). The fiber-optic elements in the OCT probe were enclosed in an ETFE tube (Zeus, Orangeburg, SC) fixed to a threaded brass tubing connector and secured to a bulkhead. The custom fabricated optic elements eliminated the gap between the ferrule and the GRIN and brought the fiber illumination to a converging focus without need for a spacer, as compared to the previous probe designs [152]. The angle-polished interface between the GRIN and the prism, further eliminates specular reflections within the probe.

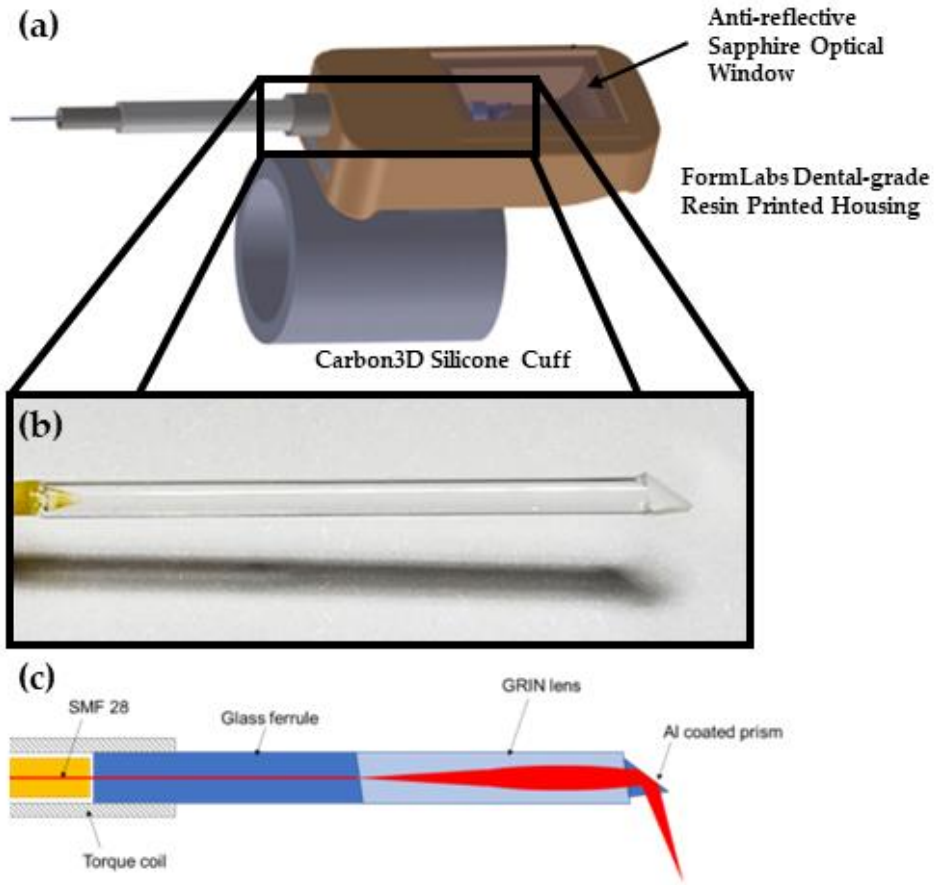

Figure 6.1 Endoscopic, rotational OCT probe used for esophageal imaging, adapted and modified from [152]. The entire device is held within a dental-grade biocompatible housing, with an attached silicone cuff for attaching the OCT probe to the endoscope, shown in (a). A single mode fiber is held within a steel torque coil and ETFE polymer sheath. A GRIN lens, spacer and prism rotate with the torque coil to scan the OCT beam radially across the tissue, shown in (c).

6.2.1.2 Image Processing

Standard spectral-domain OCT imaging processing techniques were employed to process the raw interferometric data into 2D depth profiles (B-scans), including background subtraction, k-space interpolation, and dispersion compensation [82].

Non-uniform rotational distortion (NURD) correction is then performed to compensate for the non-constant angular velocity of the rotational B-scans derived from our images [153]. First, eight key positions on the polar B-scan were defined as the fiducial markers. In a cross-sectional image, the walls of the paddle cavity and the surface of the tissue form a rectangle: four key positions are the centers of each side, and the remaining four key positions are the corners of the rectangle. Then, the true angular position of each A-line is determined by using spline interpolation with the identified A-line positions as inputs and the known angular positions of those corresponding landmarks as outputs. Finally, these A-lines are shifted to conform to a linear angular ramp and the B-scans are interpolated in the angular dimension to smoothly fill the gaps. The polar coordinate images were then remapped to x-y coordinates and cropped.

6.2.1.3 Esophageal OCT Pilot Study

A clinical pilot study was performed to assess the clinical usability of the rotational OCT device at Center for Esophageal Diseases and Swallowing (CEDAS) at UNC. Human subjects research was conducted with approval from the Institutional Review Boards at Duke University Health System (Pro0090173) and the University of North Carolina (17-3037).

To begin an imaging session, the clinician places the silicone cuff over the tip of the endoscope and navigates the probe into the esophagus under video guidance. During data acquisition of patients with suspected diseased regions, the OCT imaging window is placed against the abnormal tissue, and commencing an imaging sequence of

10 to 15 frames. Following that, at least one set of OCT scans was also acquired from a region of apparently healthy squamous epithelium. If biopsies were acquired as part of the patient's medical care from imaged regions, pathology results were obtained and added to the patient's research record to classify tissue types.

In total, 54 patients were recruited for the esophageal OCT imaging study, while one patient was withdrawn due to inadvertent enrollment. Of these, 48 patients were male and 5 were female, with the large fraction of male patients owing both to a preference for male volunteers and due to their larger esophageal lumen [154]. Of the 53 remaining, the probe was successfully delivered into the esophagus of 37 patients, of which 30 yielded adequate image sets, and 7 experienced technical failure. In total, 71 biopsy sites were imaged, resulting in 990 B-scans in this study.

An example of OCT cross-sectional images of esophageal epithelium is shown in Figure 6.2, where on the top is a squamous epithelium, showing smooth epithelial surface and consistent layered appearance, and the bottom is BE tissue, exhibiting an uneven nodular surfaces and ducts from the esophageal glands.

Table 6.1 shows the results of the classification of random-ordered deidentified OCT images by a reviewer compared with the clinical diagnosis. The OCT classification of BE was 91.5% accurate overall (65/71 image regions). Sensitivity for BE was 84.6% for BE (11/13) and specificity was 93.1% (54/58).

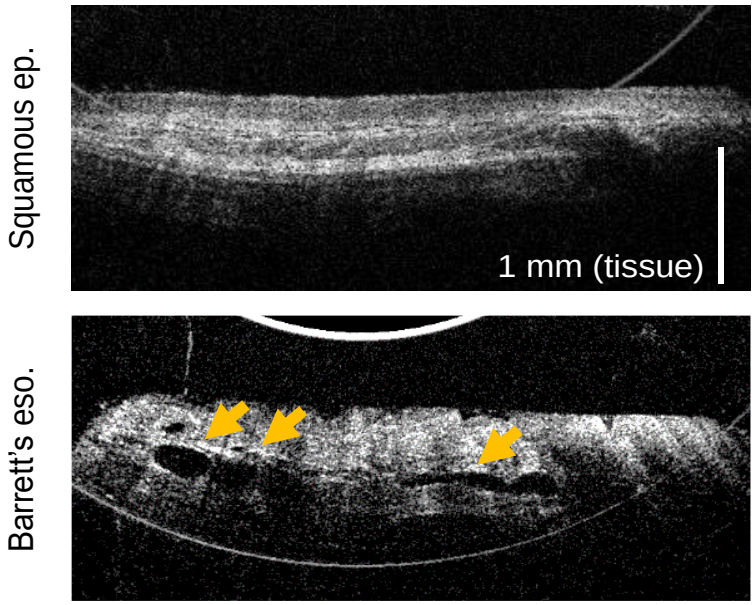

Figure 6.2 Representative OCT cross-sectional images of esophageal epithelium during the endoscopic OCT pilot study, adapted from [152]. Images from both healthy and BE tissue are displayed.

Table 6.1 Number of images classified Barrett's versus non-Barrett's by OCT image

	Clinical: Barrett's	Clinical: Non-Barrett's
OCT: Barrett's	11	4
OCT: Non-Barrett's	2	54

6.2.1.4 Layer Segmentation Based on Machine Learning

A deep learning-based segmentation algorithm was also developed for automated segmentation of human esophageal OCT images. The proposed method, connectivity-based CE-Net (Bicon-CE), defines layer segmentation as a combination of pixel connectivity modeling and pixel-wise tissue classification, and achieved good accuracy as compared to other widely used neural networks [155].

The network architecture is explained in detail in [155]. Briefly, a bilateral connectivity (Bicon-CE) network is constructed to fully model pixel connectivity along

with pixel-wise tissue classification, which contains three parts: a connectivity-based CE-Net backbone [156], a bilateral voting (BV) module and a region-guided channel aggregation (RCA) module. The CE-Net serves as the backbone, which is able to extract high-resolution features and maintain multi-scale information. To emphasize the pixel connectivity information, the output layer consists of an 8-channel FC layer and uses ground truth connectivity masks as the training labels. The bilateral voting module takes the two elements in every connectivity pair and assigns an average value to both elements. The RCA module takes the output and applies different adaptive aggregating operations and regularizes the pixels to focus on learning its connectivity with the highest likely connected neighboring pixel as well as the boundary of the segmentation [155].

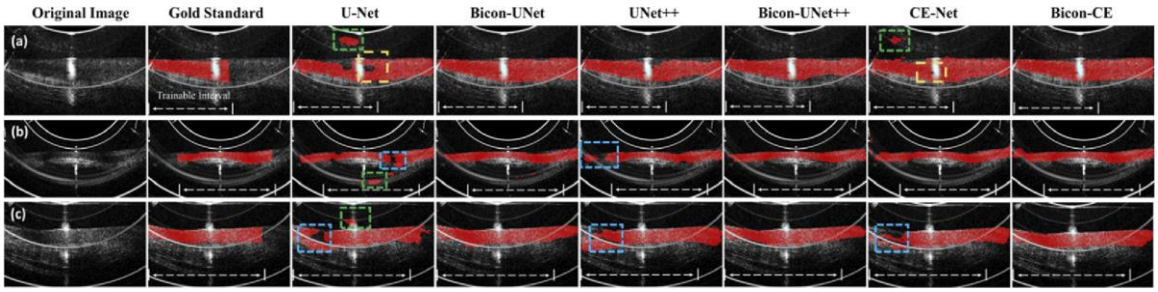

Figure 6.3 Qualitative comparisons of Bicon-CE with other state-of-the-art segmentation algorithms, adapted from [155].

The OCT data were labeled independently by an experienced grader, and the annotations served as the gold standard. The horizontal range of the annotation defines the trainable interval for each image, and during training, each OCT image are cropped based on this trainable interval before feeding into the network. In the testing phase, the

uncropped images directly serve as the network inputs, but the accuracy of the segmentation is compared within the trainable interval defined by the gold standard.

The results for Bicon-CE are compared with five other widely used medical image segmentation models, and the comparison results are shown in Figure 6.3, where the first column is the original OCT image, the second column is the segmentation mask of the gold standard, the third to seventh columns are the results of the five other segmentation models, and the most right column is the result of the Bicon-CE model. Our proposed method reduces topological problems such as outlier prediction (green box), disconnected prediction (blue box), and non-simply connected prediction (yellow box), shown in Figure 6.3. Bicon-CE produced connected and smooth segmentation of the epithelial layer of the tissue, and resulted in a dice coefficient of 0.903 ± 0.105, highest among the other segmentation models (0.866, 0.891, 0.858, 0.879, 0.859 from left to right respectively).

The segmentation algorithm also demonstrated effectiveness in detecting BE, and shows great potential in detecting BE with dysplasia. An example is shown in Figure 6.4, where the segmentation of esophageal epithelial tissue of OCT B-scans of subjects with BE (top) compared with high-grade dysplasia (bottom). There is ongoing work to conduct a detailed statistical analysis based on these segmentations, including calculating characteristic parameters (mean thickness, std thickness, etc.) and conduct multi-variable classification based on these parameters. This will definitely help identify the pathologic regions, and ultimately, provide guidance to the clinician.

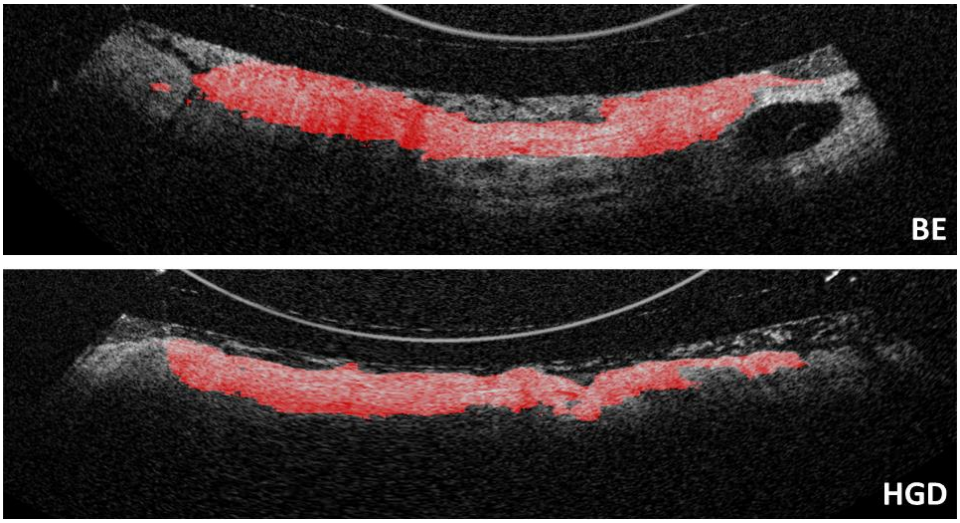

Figure 6.4 Segmentation of esophageal epithelial tissue on OCT B-Scans of subjects with Barrett's esophagus (top) and high-grade dysplasia (bottom).

6.2.2 Paddle a/LCI Device

6.2.2.1 Pathlength-Matched Linear Fiber Array (PLFA)

The first paddle a/LCI device component to be constructed is the pathlength-matched linear fiber array (PLFA) [125, 126], which will serve to transfer the scattering field from the tissue to the optical engine, substituting for the coherent fiber bundle in traditional a/LCI design.

The PLFA consists of 28 single-mode optical fibers (Thorlabs SM800G80) stacked in a linear configuration within a custom 3D-printed ferrule, and the length of each fiber is matched within a precision of ± 50 μm. This is established through a basic interferometry setup, where a pathlength-matching fiber was placed in one arm of the interferometer to serve as the pathlength standard. Then the 28 SM fibers were cut and polished to approximately 2.5 m using a razor blade, and connected into the other arm of the interferometer sequentially for optical pathlength matching. Clamp-stabilized

bare-fiber adapters (80 mm bore, Precision Fiber Products, Inc.) were used as temporal connection of the fiber to the interferometer. The fibers that are longer than the standard length were then briefly air-polished to remove a miniscule amount of optical pathlength, and polished on a mechanical polishing tower using a 6 μm grit polishing film, for ensuring a smooth surface for light transmission. The newly polished bare fiber was then inserted back into the interferometer, and the same protocol above was followed until interference signal was observed. This process is repeated for all 28 SM fibers, such that each 2.5 m fiber exhibited an error range of $\Delta L/L = 0.002\%$ (± 50 μm). The typical time for completing each SM fiber is approximately 15-20 minutes for a skilled technician, bringing the total time to obtain 28 matched fibers to between 7 and 9 hours.

The next step is to assemble the 28 SM fibers in a linear configuration by using a 3D-printed linear ferrule. This was designed in SolidWorks, and printed on a 3D printer (Form3, Formlabs) with a total outer dimension of 4.3 mm x 1.8 mm x 10 mm, slight adjustments were made compared with the initial design. In the middle, a 100 μm linear slit is formed for stacking the fibers vertically. To ensure the fibers terminated in the same plane, a glass coverslip was utilized to act as a backstop for the fibers, as shown in Figure 6.5 (a). To monitor the assembly process, a color camera with a variable zoom lens was positioned to visually monitor the fiber assembly process. To control the illumination beam's polarization incident on the tissue, a polarization-maintaining (PM) fiber (Thorlabs, HB800G) was included at both ends of the linear fiber array, with a total

optical pathlength ~30 cm longer than the SM fibers. After insertion of the PM fiber, the orientation of PM fiber's polarization axis was adjusted accordingly, as shown in Figure 6.5 (c). After all fibers were in place, a small drop of low-viscosity optical adhesive (Norland NOA 72) was injected using a syringe, and after the adhesive slowly flows into the ferrule, an UV pen (LOCTITE EQ CL32) was used to cure the optical adhesive. Epoxy was also added and cured at the connection point between the 30 fibers and the ferrule for additional protection. The fiber order was noted on the other end of the 28 SM fibers, and a second ferrule was used to construct the opposite end of the PLFA, and fiber connecters were added to the other end of the PM fibers to connect with the optical engine, as shown in Figure 6.5 (e).

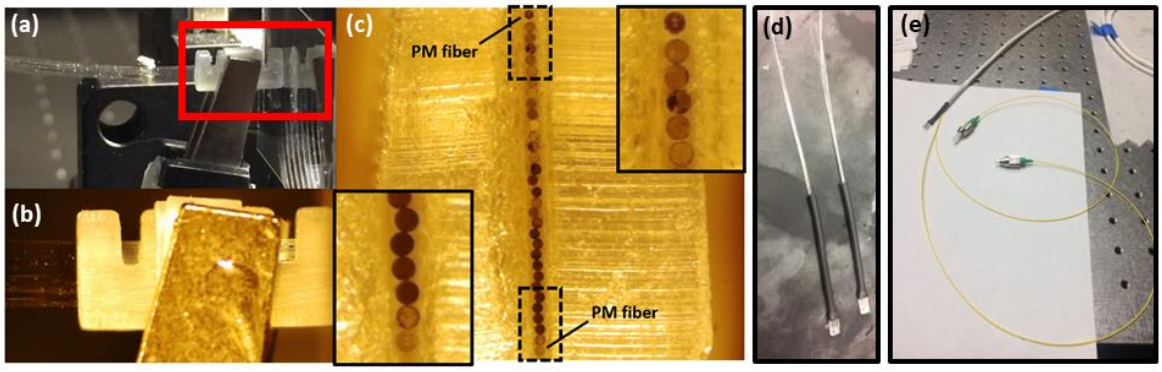

Figure 6.5 Assembly process of the pathlength-matched linear fiber array (PLFA).

6.2.2.2 Paddle Design

The second component to be constructed is the paddle for mapping distinct SM fibers to the angle-resolved scattering field from the tissue. A 4*f* imaging system was designed for relaying and demagnifying the fiber plane onto the back focal surface of the GRIN lens, as shown in Figure 6.6 (h), such that each fiber is matched to a unique

scattering angle. This optical train consists of an achromatic lens (Edmund Optics, f = 7.5 mm) and an aspheric lens (Thorlabs, f = 4.03 mm), resulting in a 0.54 magnification. For improved clinical utility, a gold-coated right-angle prism (Thorlabs, 3 mm) was placed after the 4f imaging system to enable side-viewing imaging for upper endoscopy, shown in the dashed-black box in Figure 6.6 (d). a 0.23-pitch GRIN lens (Edmund Optics, 1.8 mm diameter) was used to collimate the illumination beam onto the sample at an oblique angle, and collect the scattering field from the tissue.

The CAD model of the housing for the miniaturized optics is shown in Figure 6.6 (a) – (e). The probe was printed in two halves with sawtooth mating features for easy assembly, as shown in Figure 6.6 (a). Inside each half, the design of the grooves, shown in (d) and (f), allowed easy assembly of the optical components without the need of optical adhesives. During the trial-and-error stage of using Formlab3 with biocompatible dental resin materials, slight shrinkage of the model was observed after curing the epoxy. In order to compensate for the surface imperfections, the slots for each optical element were designed to be 100 μm larger than the actual size. To protect the coated surface of the GRIN lens, a small glass coverslip (Thomas Scientific, No. 1 thickness, 3 mm diameter) was bonded to the front of the GRIN using an optical adhesive (Norland, NOA81) and gently cured using a UV pen.

The two channels displayed in Figure 6.6 (e) represent the optical channel for OCT (top) and a/LCI (bottom) respectively. For the OCT channel, the rotating fiber-optic was guided into a polymer sheath, and inserted into the circular channel, and adhesives

were added to secure it in place. For the a/LCI channel, the ferrule was inserted into the rectangular porthole, and biocompatible epoxy was added to the interface and cured to protect the connection between the ferrule and the paddle, which is a potential mechanical failure point.

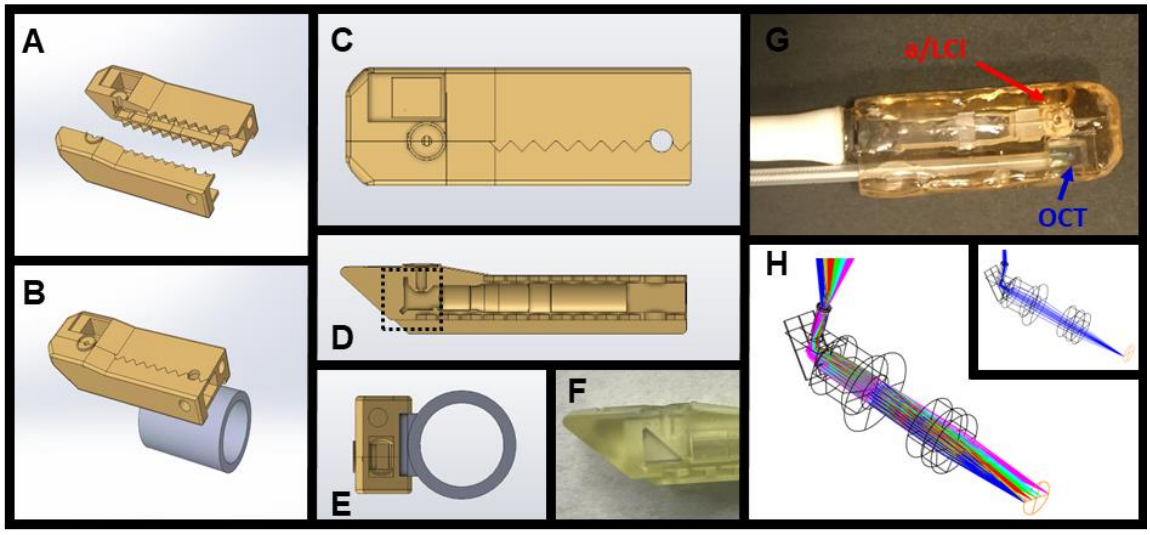

Figure 6.6 a/LCI-OCT paddle housing for both a/LCI and OCT components. The a/LCI portion consists of a 4*f* imaging system, a gold-coated right-angle prism, and a GRIN lens. The OCT portion consists of a single-mode fiber within a wound steel torque coil and ETFE polymer sheath. The whole paddle was printed with sawtooth mating features for improved bonding. A 3 mm circular glass coverslip was used to cover the a/LCI porthole, while the OCT window is covered using a rectangular sapphire window, coated for anti-reflection in the 1300 nm window.

6.2.2.3 Optical Engine

A schematic diagram of the optical engine of the combined system is shown in Figure 6.7. The a/LCI engine uses a SLD ($\lambda_0 = 830$ nm, power = 20 mW) as the light source, and the light is split into a 99:1 fiber splitter for sample and reference paths respectively. To control the polarization prior to coupling into the PM fiber of the PLFA, a three-paddle manual polarization controller (Thorlabs) was placed in the sample arm.

Light collected from the sample is imaged onto a 50 μm slit of an imaging spectrometer. A USB3 camera (Grasshopper3, FLIR, 2.3 MP, 5.86 μm pixels) was used as the detector. Two solenoid-based inductive optical shutters (DACO Instruments) were placed into the sample and reference arms of the device for acquiring four acquisitions (signal, reference, interference and background) with adequate switching time for the shutters.

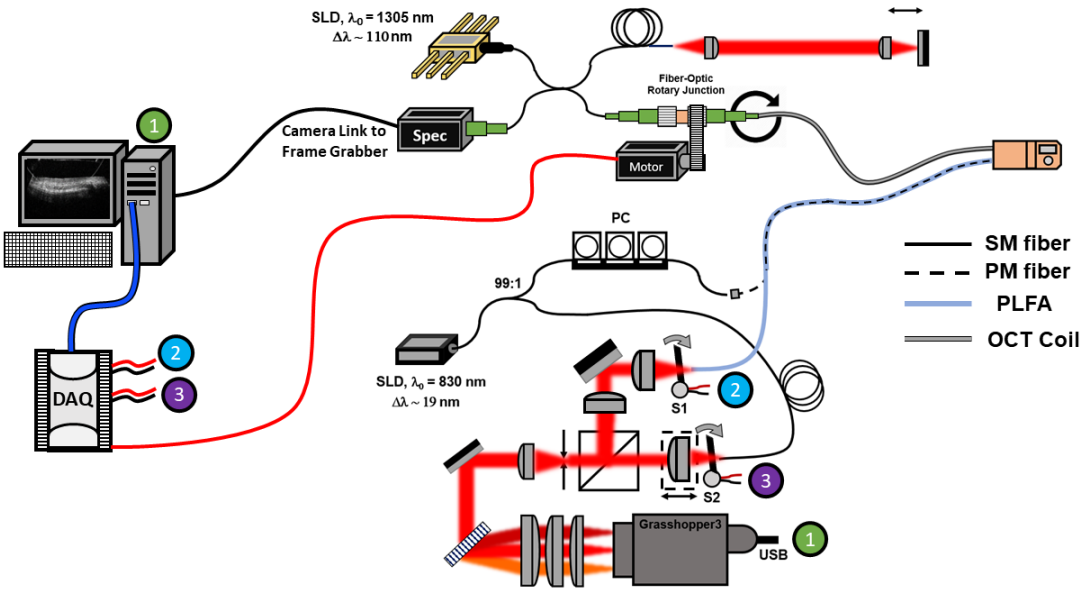

Figure 6.7 Schematic diagram of the optical engine of the combined system, adapted from [125, 126]. A superluminescent diode (λ = 830 nm, $\Delta\lambda$ = 19 nm) is polarization-controlled and coupled into the PM fiber of the probe. The backscattering profile collected from the tissue is imaged onto the slit of a custom designed imaging spectrometer along with the combined pathlength-matched reference field.

6.2.2.4 Validations using Microsphere Phantoms

a/LCI processing has been described in detail in Chapter 2. Briefly, each interferogram is background subtracted to isolate the interference only term from the collected signal. Dispersion compensation is applied digitally, and a one-dimensional

Fourier transformation is performed along the spectral domain to recover the depth-encoded information. Pixel rows containing the scattering information are selected, and the slight variability in optical pathlength between each fiber is adjusted based on developed peaking finding and adjustment algorithm. The completed scan then represents a two-dimensional map of intensity as a function of scattering angle and depth.

Then, the a/LCI device was validated using polystyrene microsphere phantoms of size 6, 8, 10 and 12 μm, similar to the method from previous chapters, and the calibration curves are shown in Figure 6.8. The scatterers were correctly sized at 6.06 ± 0.07 μm, 8.02 ± 0.05 μm, 9.96 ± 0.12 μm, 12.02 ± 0.09 μm, respectively, with a mean error of only 93 nm, showing the effectiveness of our device in characterizing the size of small scattering objects.

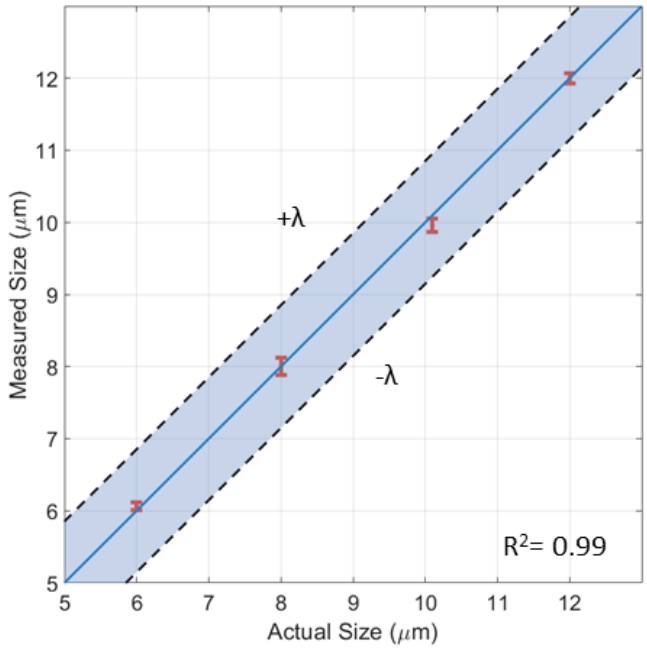

Figure 6.8 Calibration curve of the a/LCI device for characterizing the size of polystyrene microsphere phantoms of size 6, 8 ,10, and 12 μm.

6.3 *Clinical Study Design*

A photograph of the developed clinical mobile cart for the combined a/LCI-OCT system is shown in Figure 6.9. The system is controlled by a desktop computer, which controls the a/LCI and OCT systems through a custom developed LabVIEW software. The a/LCI probe easily attaches to the engine using a cage mount. Slight misalignment could be adjusted using the translation stage in the sample arm. A physical ENABLE/DISABLE switch was included for the rotational OCT's stepper motor circuitry for prevention of rotation of the probe prior to the clinical trial. A typical setup procedure takes around 5 – 10 mins.

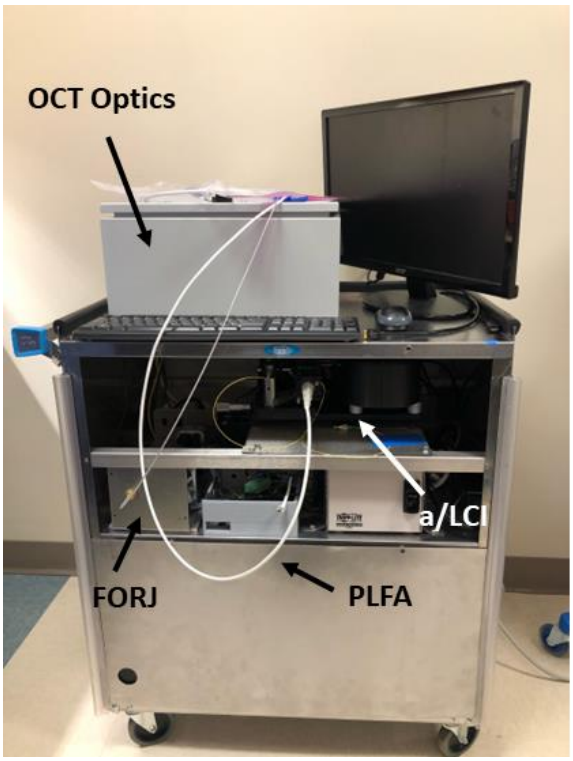

Figure 6.9 Photograph of the clinical combined a/LCI-OCT system.

This clinical study was conducted at the Center for Esophageal Diseases and Swallowing (CEDAS) at University of North Carolina. We enrolled a total of 37 patients, including 37 male and 8 females, with the large fraction of male patients owing both to a preference for male volunteers due to their larger esophageal lumen [154], and a higher incidence of BE and BE-related conditions in adult males [157]. Table 6.2 summaries the patient enrollment, as well as the patients that are successfully imaged, with a total of 50 biopsy sites imaged using this combined instrument. After voluntary informed consent, each patient was interviewed to obtain demographic and behavioral characteristics. During the imaging session, the clinician places the silicone cuff over the tip of the endoscope and navigates the probe into the esophagus under video guidance. After the probe reaches the imaging site, the ENABLE switch was turned on, and 100 repeated

optical a/LCI scans (40 milliseconds each) were collected (total of 4s), along with 10 – 15 OCT scans. After this, the doctor then directs the biopsy forceps and takes co-registered esophageal biopsies at the imaging site.

Table 6.2 Patient enrollment summary

Category	Successfully Enrolled	Successfully Imaged
Total Number	37	31
Male	29	24
Female	8	7
Mean Age	65.3 years	64.7 years
Age Range	47 – 78 years	47 – 78 years

The tissue biopsy specimens were then sent to a clinical laboratory and analyzed by a pathologist blinded to the a/LCI-OCT optical biopsy results and categorized as either no BE (benign), non-dysplastic BE (NDBE), BE with low-grade dysplasia (BE w/LGD), or BE with high-grade dysplasia (BE w/HGD). This study was conducted with approval from the Institutional Review Boards at Duke University Health System and the University of North Carolina.

6.4 Data Processing

Each a/LCI scan was processed using the methods described in Chapter 2 and section 6.2.2.4. The a/LCI scans were then processed by segmenting each scan into 50 μm depth bins, and the mean nuclear size and average nuclear density for the basal

epithelial layer (200-300 μm depth segment) was used as a biomarker for dysplasia. Prior to determining the nuclear morphology, the a/LCI A-scans were analyzed to exclude scans with insufficient signal, mainly due to poor signal quality including patient movement, probe movement, or poor tissue contact with the probe. Each OCT scan was processed using the methods described in section 6.2.1.2., and was used as a reference for determining the start of the epithelium for analyzing each a/LCI scan. After analyzing both the a/LCI and OCT data, the results are compared to histopathological classification.

Statistical analysis was performed based on a prospective decision line from our first-in-human pilot study of a/LCI to detect precancerous lesions in the esophageal epithelium of BE patients [92]. In that study, the histopathology results were dichotomized by dysplastic (LGD/HGD) vs. non-dysplastic (No BE, and NDBE), and the optimal point was determined on a receiver operating characteristic (ROC) curve. Here, statistical analysis was performed directly using the prospective decision line place at 11.84 μm, and comparisons of the two groups were conducted using two-sided t-test, and sensitivity, specificity, NPV, and PPV values are calculated accordingly. Statistical analyses were performed using MATLAB, R2021a (MathWorks, Inc., Natick, MA) and R (RStudio, Boston, MA).

6.5 Results

We obtained a/LCI and OCT scans of sufficient quality for analyses from 60 distinct esophageal biopsy sites (NoBE, n = 39; NDBE, n = 4; Bew/LGD, n = 4; Bew/HGD, n = 3; Uncertain, n = 10), of which co-registered biopsies were not acquired at 10 biopsy sites during the imaging sessions.

The main achievement of this study was the implementation of co-registered a/LCI measurements with OCT imaging. Example data from the combined a/LCI and OCT platform are shown in Figure 6.10. The left shows example OCT images of BE patients with and without dysplasia. In the center the corresponding angle-resolved depth scan of light scattering from the tissue are shown, and on the right the angular scattering distributions at the basal layer of the epithelium, and its corresponding best-fit Mie theory solutions (red-lines) are shown. Previous studies have shown that overlying mucus or the presence of air (shown as the red arrow in Figure 6.10) can be a confounding influence when trying to determine the tissue layers in a/LCI measurements [158]. Here, OCT images can serve as "depth markers" and are used to register a/LCI measurements to the basal layer of the epithelium.

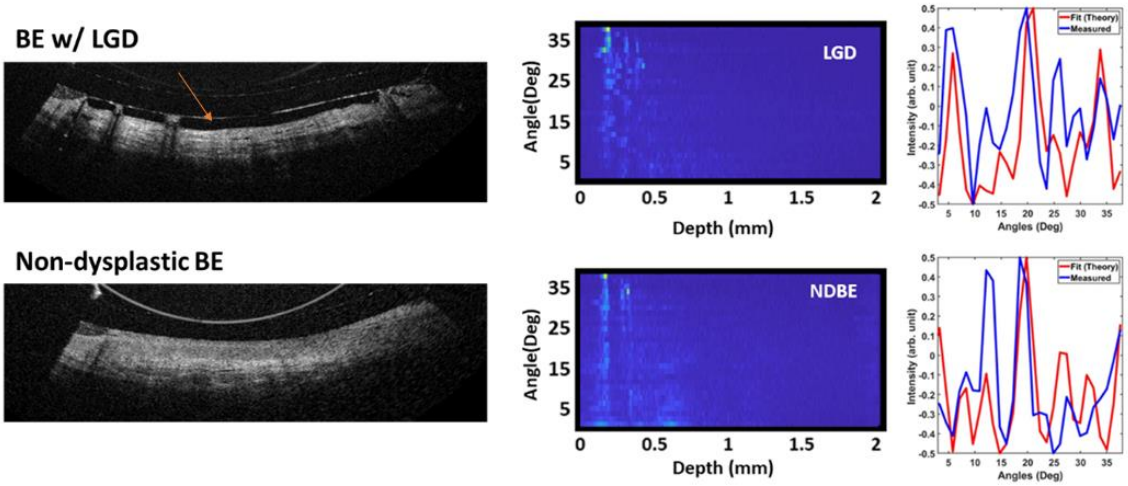

Figure 6.10 Typical data from the combined a/LCI and OCT platform. (Left) OCT images from BE patients with and without dysplasia (Center) Angle-resolved depth scan of light scattered from tissue. (Right) Example angular scans for 2 tissue types (blue line) with best-fit Mie theory solutions (red line).

The ability of the system to distinguish dysplastic biopsy sites was then analyzed by comparing the results between dysplastic (LGD, HGD) vs. non-dysplastic (No BE, NDBE) tissue dichotomization shown in Prospective study results: Scatter plot with each biopsy plotted as a function of its nuclear size and density, as measured by the a/LCI system, and categorized by its pathological diagnosis. Dashed black line indicates decision line from previous study, resulting in 100% sensitivity/93% specificity.

Table 6.3. Using Mie theory ILSA, a significantly greater mean nuclear diameter was observed for the dysplastic biopsy sites compared to the non-dysplastic biopsy sites, with a mean diameter of 13.56 μm compared with 8.65 μm ($p \ll 0.001$). In addition, a significantly lower mean nuclear density was observed for the dysplastic biopsy sites compared to the non-dysplastic sites (1.051 versus 1.061, $p < 0.001$) at this basal layer of the tissue. A scatterplot of the Mie theory ILSA predicted nuclear morphology for the biopsy sites is shown in Figure 6.11. A prospective decision line (placed at 11.84 μm, shown in dashed black line) acquired from a previous clinical study was used as the classification line in distinguishing dysplastic from non-dysplastic tissue sites, resulting in a sensitivity of 1.00 (7/7) and specificity of 0.93 (40/43) respectively. There is a statistically significant improvement in specificity (current 0.93 compared with previous 0.84), suggesting that the use of OCT guidance improves the ability to target biopsies. The corresponding negative predictive value (NPV) and positive predictive value (PPV) are 1.00 (40/40) and 0.70 (7/10) respectively, and the overall accuracy of this classification is 0.93 (47/50). Full statistical analysis of these results is presented in Table 6.3.

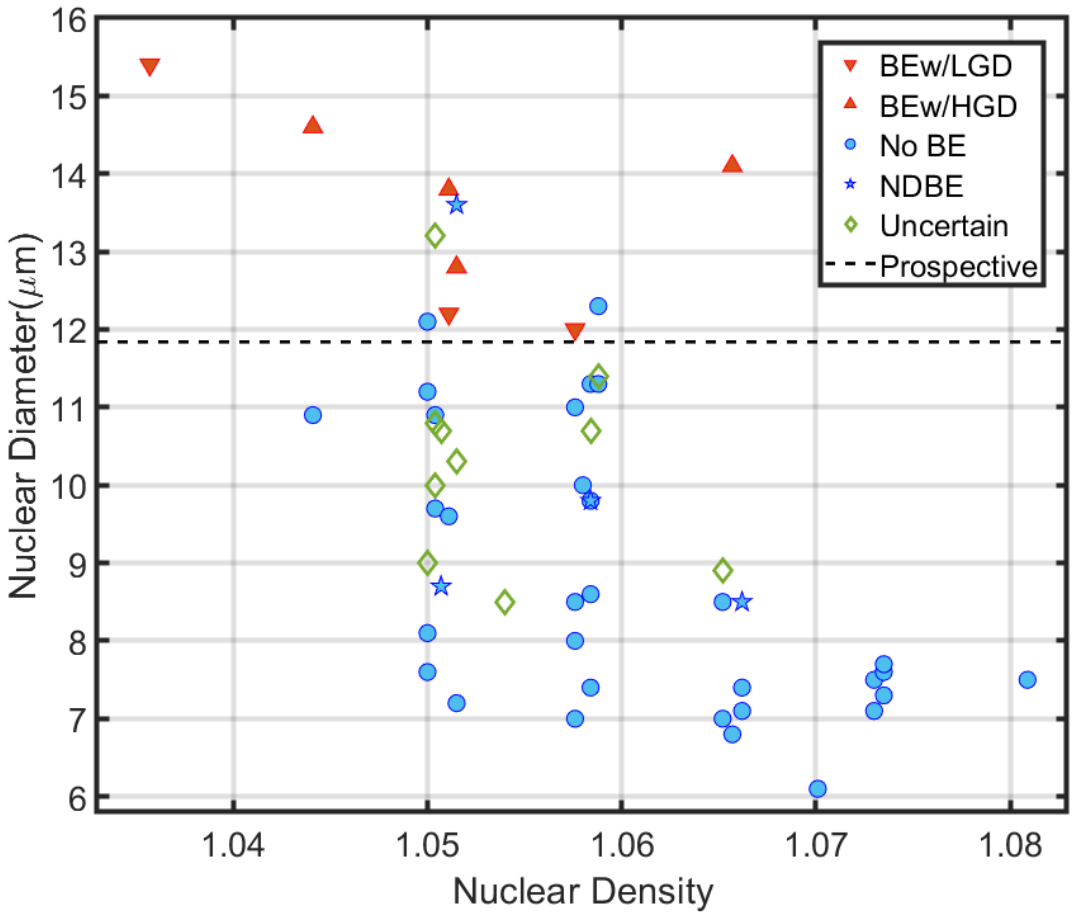

Figure 6.11 Prospective study results: Scatter plot with each biopsy plotted as a function of its nuclear size and density, as measured by the a/LCI system, and categorized by its pathological diagnosis. Dashed black line indicates decision line from previous study, resulting in 100% sensitivity/93% specificity.

Table 6.3 a/LCI optical biopsy results

Category	Mie-theory ILSA
Dysplastic (LGD/HGD) vs. Non-Dysplastic (NDBE and No BE)	
Nuclear Diameter (μm, mean ± SD)	
Dysplastic (n = 7)	13.56 ± 1.27
Non-dysplastic (n = 43)	8.65 ± 1.83
p-value	$p \ll 0.001$
Nuclear Density (mean ± SD)	
Dysplastic	1.051 ± 0.010
Non-dysplastic	1.061 ± 0.009
p-value	$p < 0.001$
Sensitivity [a]	1.00 (7/7)
Specificity [a]	0.93 (40/43)
NPV [a]	1.00 (40/40)
PPV [a]	0.70 (7/10)
Accuracy	0.94 (47/50)
Data Processing Time (ms/Profile)	200.1

[a] Sensitivity, specificity, NPV and PPV based on a prospective decision line from a previous clinical study **[92]**

For determining the data processing time, 1000 angular scattering profiles were analyzed using the ILSA algorithm, the average time per profile was calculated, resulting in an average processing time of 200.1 ms. This corresponds to approximately 2 seconds for processing each optical biopsy.

6.6 Discussion

The combined a/LCI and OCT platform detected a statistically significant increase in nuclear diameter at the basal layer for dysplastic tissue sites compared to non-dysplastic tissue sites. This is consistent with results from the previous clinical a/LCI study on BE which also found nuclear enlargement at the basal layer of the esophageal epithelium, and were associated with an increased likelihood of having dysplasia [92]. Using the decision line from the previous study, the overall accuracy of the measurements improved from 86% to 94%, a statistically significant increase. While the 100% sensitivity was consistent with the previous study, a significant increase of specificity was found (from 84% to 93%), suggesting the use of OCT guidance improves the ability to target biopsies.

The results from this study also demonstrate the promising clinical utility of this combined a/LCI and OCT platform as an optical biopsy tool to supplement traditional biopsy screening. In particular, the high NPV of the method may allow the clinician to avoid taking a biopsy when presented with a normal nuclear morphology measurement from the optical biopsy and better locate dysplastic tissue sites.

Another major development is the implementation of the co-registered a/LCI measurements with the real-time OCT imaging guidance. The previous clinical study exhibited a high rejection rate of a/LCI scans due to low signal intensity, mainly because of probe movement, insufficient contact of the probe with the tissue and poor tissue appositions. In this study, the visual guidance of OCT helped orient a/LCI measurements by ensuring good tissue apposition such that layered structures are even across the field of view and depth resolved scattering information can be retrieved. Previous studies have also shown that overlying mucus can be a confounding influence when trying to determine the start of the tissue directly from the a/LCI measurements. The OCT tomograms provided an optimal solution, as they can help avoid acquiring unmeaningful information due to the presence of air or mucous, as well as registering a/LCI measurements at the basal layer of the epithelial tissue.

Future work will first focus on upgrading the a/LCI instrumentation platform. A new a/LCI fiber probe will be designed based on the advances presented in Chapter 4. The MMF-based probe would provide improved robustness, mechanical stability, and reduced construction complexity compared with the fabrication of the PLFA. Another limitation of the current system is the reduced passage rate of the probe into the esophagus compared to previous a/LCI probes based on coherent fiber bundles. Future work will also focus on refinement of the current paddle design for improved clinical utility. In addition, future work will also include implementation of real-time processing software based deep learning and real-time software for automated analysis. Current

ILSA algorithm takes approximately 2 seconds for processing each optical biopsy. Ideally, processing should take under one second to provide instant feedback to clinicians for rapid screening of the disease. Future work will focus on developing deep learning techniques similar to Chapter 5 for fast and accurate diagnosis.

6.7 Summary

This clinical study has demonstrated the feasibility of applying the combined a/LCI and OCT platform to the esophageal epithelium and collecting a/LCI measurements with OCT tomograms during routine upper endoscopy. The combination of the two optical engines was demonstrated, including the construction of the clinical cart to house all opto-mechanics and electronics, and the optical design. The design of the PLFA for a/LCI instrumentation led to improved optical throughput as well as reduced cost, and the miniaturization of the paddle allowed easier passage of the probe for in vivo human esophageal imaging. Further, the parallel side-viewing design of the a/LCI and OCT channel provided co-registered real-time OCT imaging guidance, which demonstrated the ability of OCT for targeting potential diseased biopsies as well as registering a/LCI measurements to the basal layer of the epithelium.

Analysis of the a/LCI data confirmed a strong relationship between nuclear enlargement at the basal layer and the presence of dysplasia in histological analysis. The use of the combined a/LCI-OCT system led to improved overall accuracy of the measurements when compared to histology, suggesting that optical biopsy characterization using a/LCI nuclear morphology measurements with real-time OCT

imaging guidance would aid the clinician in identifying dysplastic tissue sites in vivo, leading to improved screening protocols, and ultimately, better patient outcomes.

7 Conclusions

The work presented in this dissertation describes the development of novel optical technologies to diagnose epithelial dysplasia, a venture which will ultimately lead to improved screening, improve patient outcomes, and reduce mortality. Advanced instrumentation designs as well as new algorithms were introduced for improving a/LCI technology.

The initial effort discussed in Chapter 3 focused on a theoretical analysis of the effect of different modifications to the scattering function in a/LCI. It outlines a computational study which analyzes a full a/LCI clinical dataset of 40 patients undergoing optical and histological biopsy of the cervix, while modifying its angular sampling, angular range and other parameters. This chapter provides guidance for instrumentation designs in the following chapters, including the development of the multimode fiber setup for collecting angular scattering profiles discussed in Chapter 4 and the PLFA design discussed in Chapter 6. Most of this chapter will also be useful for guiding future a/LCI prototyping.

While a/LCI has already proven to be an effective diagnostic tool in biological tissues to diagnose dysplasia, one limiting factor of a/LCI is the excessive data processing time of the Mie-theory-based ILSA algorithm. The need for real-time nuclear morphology measurements led to the development of a deep learning algorithm to identify disease state of tissue using raw a/LCI light scattering data, mentioned in Chapter 5. The performance of the algorithm is comparable to that of the Mie-theory-

based gold standard of inverse light scattering analysis while being faster and more generalizable across different patients or a/LCI instruments.

Another limiting factor of a/LCI is the use of fiber bundles as these fiber bundles are fragile, expensive, and exhibit low optical throughput. This motivates the development of the opto-mechanical instrumentation using a single multimode fiber in Chapter 4, and the development of the combined a/LCI-OCT platform for detecting esophageal dysplasia in Chapter 6.

Chapter 4 introduces a novel opto-mechanical instrumentation setup for reconstruction of angular scattering distributions through a single multimode fiber. The use of a single multimode fiber would provide increased optical throughput and robustness as well as significant reduction in cost. In order to overcome the acquisition and computational complexities, we utilized the azimuthal symmetry of the angular scattering profile as it transmits through the multimode fiber, and developed a fast and accurate approach in reconstruction angular scattering distributions. Our results are also insensible to the displacement of the fiber, and showed great potential for future endoscopic applications for medical diagnostics.

Finally, in Chapter 6, a combined a/LCI and OCT system was presented for improved screening of BE tissue in vivo. The clinical study demonstrated the feasibility of applying the combined a/LCI and OCT platform to the esophageal epithelium and collecting a/LCI measurements with OCT tomograms during routine upper endoscopy. This system can provide accurate optical biopsy characterization using a/LCI nuclear

morphology measurements with real-time OCT imaging guidance, and lead to improved screening protocols, and ultimately, better patient outcomes. A future clinical feasibility study will be conducted on a larger patient population to validate the performance of an advanced a/LCI instrumentation based on a single multimode fiber. Further refinement and optimization of this combined a/LCI and OCT system has the potential for a fully automated coherence imaging platform for detecting esophageal dysplasia.

Reference

1. Sung, H., et al., *Global cancer statistics 2020: GLOBOCAN estimates of incidence and mortality worldwide for 36 cancers in 185 countries.* CA: a cancer journal for clinicians, 2021. **71**(3): p. 209-249.

2. Pohl, H., B. Sirovich, and H.G. Welch, *Esophageal adenocarcinoma incidence: are we reaching the peak?* Cancer epidemiology, biomarkers & prevention, 2010. **19**(6): p. 1468-1470.

3. Morgan, E., et al., *The global landscape of esophageal squamous cell carcinoma and esophageal adenocarcinoma incidence and mortality in 2020 and projections to 2040: new estimates from GLOBOCAN 2020.* Gastroenterology, 2022. **163**(3): p. 649-658. e2.

4. Abrams, J.A., et al., *Adherence to biopsy guidelines for Barrett's esophagus surveillance in the community setting in the United States.* Clinical Gastroenterology and Hepatology, 2009. **7**(7): p. 736-742.

5. Shaheen, N.J., et al., *ACG clinical guideline: diagnosis and management of Barrett's esophagus.* Official journal of the American College of Gastroenterology| ACG, 2016. **111**(1): p. 30-50.

6. Das, D., et al., *Management of Barrett's esophagus in the UK: overtreated and underbiopsied but improved by the introduction of a national randomized trial.* Official journal of the American College of Gastroenterology| ACG, 2008. **103**(5): p. 1079-1089.

7. Wani, S., et al., *Endoscopists systematically undersample patients with long-segment Barrett's esophagus: an analysis of biopsy sampling practices from a quality improvement registry.* Gastrointestinal endoscopy, 2019. **90**(5): p. 732-741. e3.

8. Rubenstein, J.H. and N.J. Shaheen, *Epidemiology, diagnosis, and management of esophageal adenocarcinoma.* Gastroenterology, 2015. **149**(2): p. 302-317. e1.

9. Drezek, R., et al., *Autofluorescence microscopy of fresh cervical-tissue sections reveals alterations in tissue biochemistry with dysplasia¶.* Photochemistry and photobiology, 2001. **73**(6): p. 636-641.

10. Georgakoudi, I., et al., *Trimodal spectroscopy for the detection and characterization of cervical precancers in vivo.* American journal of obstetrics and gynecology, 2002. **186**(3): p. 374-382.

11. Mahadevan-Jansen, A., et al., *Near-infrared Raman spectroscopy for in vitro detection of cervical precancers.* Photochemistry and photobiology, 1998. **68**(1): p. 123-132.

12. Drezek, R., et al., *Light scattering from cervical cells throughout neoplastic progression: influence of nuclear morphology, DNA content, and chromatin texture.* Journal of biomedical optics, 2003. **8**(1): p. 7-16.

13. Wax, A., et al., *Cellular organization and substructure measured using angle-resolved low-coherence interferometry.* Biophysical journal, 2002. **82**(4): p. 2256-2264.

14. Lovat, L.B., et al., *Elastic scattering spectroscopy accurately detects high grade dysplasia and cancer in Barrett's oesophagus.* Gut, 2006. **55**(8): p. 1078-1083.

15. Rodriguez-Diaz, E., et al., *Endoscopic histological assessment of colonic polyps by using elastic scattering spectroscopy.* Gastrointestinal endoscopy, 2015. **81**(3): p. 539-547.

16. Gomes, A.J., et al., *In vivo measurement of the shape of the tissue-refractive-index correlation function and its applicationto detection of colorectal field carcinogenesis.* Journal of Biomedical Optics, 2012. **17**(4): p. 047005-047005.

17. Qiu, L., et al., *Multispectral light scattering endoscopic imaging of esophageal precancer.* Light: Science & Applications, 2018. **7**(4): p. 17174-17174.

18. Isenberg, G., et al., *Accuracy of endoscopic optical coherence tomography in the detection of dysplasia in Barrett's esophagus: a prospective, double-blinded study.* Gastrointestinal endoscopy, 2005. **62**(6): p. 825-831.

19. Blanpain, C., *Tracing the cellular origin of cancer.* Nature cell biology, 2013. **15**(2): p. 126-134.

20. Troy, T.L. and S.N. Thennadil, *Optical properties of human skin in the near infrared wavelength range of 1000 to 2200 nm.* Journal of biomedical optics, 2001. **6**(2): p. 167-176.

21. Pyhtila, J.W., R.N. Graf, and A. Wax, *Determining nuclear morphology using an improved angle-resolved low coherence interferometry system.* Optics Express, 2003. **11**(25): p. 3473-3484.

22. Pyhtila, J.W. and A. Wax, *Rapid, depth-resolved light scattering measurements using Fourier domain, angle-resolved low coherence interferometry.* Optics Express, 2004. **12**(25): p. 6178-6183.

23. Wax, A., et al., *Angle-resolved low coherence interferometry for detection of dysplasia in Barrett's esophagus.* Gastroenterology, 2011. **141**(2): p. 443-447. e2.

24. Zhu, Y., N.G. Terry, and A. Wax, *Angle-resolved low-coherence interferometry: an optical biopsy technique for clinical detection of dysplasia in Barrett's esophagus.* Expert Rev Gastroenterol Hepatol, 2012. **6**(1): p. 37-41.

25. Terry, N.G., et al., *Detection of intestinal dysplasia using angle-resolved low coherence interferometry.* Journal of biomedical optics, 2011. **16**(10): p. 106002.

26. Ho, D., et al., *Evaluation of hybrid algorithm for analysis of scattered light using ex vivo nuclear morphology measurements of cervical epithelium.* Biomedical optics express, 2015. **6**(8): p. 2755-2765.

27. Ho, D., et al., *Feasibility of clinical detection of cervical dysplasia using angle-resolved low coherence interferometry measurements of depth-resolved nuclear morphology.* International Journal of Cancer, 2017. **140**(6): p. 1447-1456.

28. Kendall, W.Y., et al., *Prospective detection of cervical dysplasia with scanning angle-resolved low coherence interferometry.* Biomedical Optics Express, 2020. **11**(9): p. 5197-5211.

29. Brown, W.J., et al., *Review and recent development of angle-resolved low-coherence interferometry for detection of precancerous cells in human esophageal epithelium.* IEEE Journal of Selected Topics in Quantum Electronics, 2008. **14**(1): p. 88-97.

30. Ho, D., et al., *Wavelet transform fast inverse light scattering analysis for size determination of spherical scatterers.* Biomedical optics express, 2014. **5**(10): p. 3292-3304.

31. Amoozegar, C., et al., *Experimental verification of T-matrix-based inverse light scattering analysis for assessing structure of spheroids as models of cell nuclei.* Applied optics, 2009. **48**(10): p. D20-D25.

32. Ford, H.D. and R.P. Tatam, *Characterization of optical fiber imaging bundles for swept-source optical coherence tomography.* Applied optics, 2011. **50**(5): p. 627-640.

33. Reichenbach, K.L. and C. Xu, *Numerical analysis of light propagation in image fibers or coherent fiber bundles.* Optics express, 2007. **15**(5): p. 2151-2165.

34. Risi, M.D., et al., *Analysis of multimode fiber bundles for endoscopic spectral-domain optical coherence tomography.* Applied optics, 2015. **54**(1): p. 101-113.

35. Steelman, Z.A., et al., *Comparison of imaging fiber bundles for coherence-domain imaging.* Applied optics, 2018. **57**(6): p. 1455-1462.

36. Zhang, H., et al., *Angular range, sampling and noise considerations for inverse light scattering analysis of nuclear morphology.* Journal of biophotonics, 2019. **12**(2): p. e201800258.

37. Zhang, H., et al., *Deep learning classification of cervical dysplasia using depth-resolved angular light scattering profiles.* Biomedical Optics Express, 2021. **12**(8): p. 4997-5007.

38. Zhang, H., et al., *Reconstruction of angle-resolved backscattering through a multimode fiber for cell nuclei and particle size determination.* APL Photonics, 2020. **5**(7): p. 076105.

39. Haggitt, R.C., *Barrett's esophagus, dysplasia, and adenocarcinoma.* Human pathology, 1994. **25**(10): p. 982-993.

40. Souza, R.F., K. Krishnan, and S.J. Spechler, *Acid, bile, and CDX: the ABCs of making Barrett's metaplasia.* American Journal of Physiology-Gastrointestinal and Liver Physiology, 2008. **295**(2): p. G211-G218.

41. Winters Jr, C., et al., *Barrett's esophagus: a prevalent, occult complication of gastroesophageal reflux disease.* Gastroenterology, 1987. **92**(1): p. 118-124.

42. Hvid-Jensen, F., et al., *Incidence of adenocarcinoma among patients with Barrett's esophagus.* New England Journal of Medicine, 2011. **365**(15): p. 1375-1383.

43. Wani, S., et al., *Risk factors for progression of low-grade dysplasia in patients with Barrett's esophagus.* Gastroenterology, 2011. **141**(4): p. 1179-1186. e1.

44. Thrift, A.P., *Global burden and epidemiology of Barrett oesophagus and oesophageal cancer.* Nature reviews Gastroenterology & hepatology, 2021. **18**(6): p. 432-443.

45. Codipilly, D.C., et al., *Epidemiology and outcomes of young-onset esophageal adenocarcinoma: an analysis from a population-based database.* Cancer Epidemiology, Biomarkers & Prevention, 2021. **30**(1): p. 142-149.

46. Sharma, P., et al., *Standard endoscopy with random biopsies versus narrow band imaging targeted biopsies in Barrett's oesophagus: a prospective, international, randomised controlled trial.* Gut, 2013. **62**(1): p. 15-21.

47. Incarbone, R., et al., *Outcome of esophageal adenocarcinoma detected during endoscopic biopsy surveillance for Barrett's esophagus.* Surgical Endoscopy And Other Interventional Techniques, 2002. **16**: p. 263-266.

48. Ferguson, M.K. and A. Durkin, *Long-term survival after esophagectomy for Barrett's adenocarcinoma in endoscopically surveyed and nonsurveyed patients.* Journal of gastrointestinal surgery, 2002. **6**(1): p. 29-36.

49. van Sandick, J.W., et al., *Impact of endoscopic biopsy surveillance of Barrett's oesophagus on pathological stage and clinical outcome of Barrett's carcinoma.* Gut, 1998. **43**(2): p. 216-222.

50. Peters, J.H., et al., *Outcome of adenocarcinoma arising in Barrett's esophagus in endoscopically surveyed and nonsurveyed patients.* The Journal of thoracic and cardiovascular surgery, 1994. **108**(5): p. 813-822.

51. Roumans, C.A., et al., *Adherence to recommendations of Barrett's esophagus surveillance guidelines: a systematic review and meta-analysis.* Endoscopy, 2020. **52**(01): p. 17-28.

52. Shaheen, N.J., et al., *Diagnosis and management of Barrett's esophagus: an updated ACG guideline.* The American Journal of Gastroenterology, 2022. **117**(4): p. 559-587.

53. Montgomery, E., et al., *Reproducibility of the diagnosis of dysplasia in Barrett esophagus: a reaffirmation.* Human pathology, 2001. **32**(4): p. 368-378.

54. Moriarty, J.P., et al., *Costs associated with Barrett's esophagus screening in the community: an economic analysis of a prospective randomized controlled trial of*

sedated versus hospital unsedated versus mobile community unsedated endoscopy. Gastrointestinal endoscopy, 2018. **87**(1): p. 88-94. e2.

55. Gerson, L.B., P.W. Groeneveld, and G. Triadafilopoulos, *Cost-effectiveness model of endoscopic screening and surveillance in patients with gastroesophageal reflux disease.* Clinical Gastroenterology and Hepatology, 2004. **2**(10): p. 868-879.

56. Inadomi, J.M., et al., *Screening and surveillance for Barrett esophagus in high-risk groups: a costutility analysis.* Annals of internal medicine, 2003. **138**(3): p. 176-186.

57. Januszewicz, W., et al., *Safety and acceptability of esophageal cytosponge cell collection device in a pooled analysis of data from individual patients.* Clinical Gastroenterology and Hepatology, 2019. **17**(4): p. 647-656. e1.

58. Fitzgerald, R.C., et al., *Cytosponge-trefoil factor 3 versus usual care to identify Barrett's oesophagus in a primary care setting: a multicentre, pragmatic, randomised controlled trial.* The Lancet, 2020. **396**(10247): p. 333-344.

59. Benaglia, T., et al., *Health benefits and cost effectiveness of endoscopic and nonendoscopic cytosponge screening for Barrett's esophagus.* Gastroenterology, 2013. **144**(1): p. 62-73. e6.

60. Ross-Innes, C.S., et al., *Risk stratification of Barrett's oesophagus using a non-endoscopic sampling method coupled with a biomarker panel: a cohort study.* The lancet Gastroenterology & hepatology, 2017. **2**(1): p. 23-31.

61. Shaheen, N.J., et al., *Radiofrequency ablation in Barrett's esophagus with dysplasia.* New England Journal of Medicine, 2009. **360**(22): p. 2277-2288.

62. Swisher, S.G., et al., *Effect of operative volume on morbidity, mortality, and hospital use after esophagectomy for cancer.* The Journal of thoracic and cardiovascular surgery, 2000. **119**(6): p. 1126-1134.

63. Wani, S., et al., *Endoscopic eradication therapy for patients with Barrett's esophagus–associated dysplasia and intramucosal cancer.* Gastrointestinal endoscopy, 2018. **87**(4): p. 907-931. e9.

64. Shaheen, N.J., et al., *Durability of radiofrequency ablation in Barrett's esophagus with dysplasia.* Gastroenterology, 2011. **141**(2): p. 460-468.

65. Bosch, F.X., et al., *Prevalence of human papillomavirus in cervical cancer: a worldwide perspective.* JNCI: Journal of the National Cancer Institute, 1995. **87**(11): p. 796-802.

66. Walboomers, J.M., et al., *Human papillomavirus is a necessary cause of invasive cervical cancer worldwide.* The Journal of pathology, 1999. **189**(1): p. 12-19.

67. Weinstock, H., S. Berman, and W. Cates Jr, *Sexually transmitted diseases among American youth: incidence and prevalence estimates, 2000.* Perspectives on sexual and reproductive health, 2004. **36**(1): p. 6-10.

68. Markowitz, L.E., et al., *Prevalence of HPV after introduction of the vaccination program in the United States.* Pediatrics, 2016. **137**(3).

69. Cohen, P.A., et al., *Cervical cancer.* The Lancet, 2019. **393**(10167): p. 169-182.

70. Castle, P. and M. Maza, *Prophylactic HPV vaccination: past, present, and future.* Epidemiology & Infection, 2016. **144**(3): p. 449-468.

71. Hirth, J., *Disparities in HPV vaccination rates and HPV prevalence in the United States: a review of the literature.* Human vaccines & immunotherapeutics, 2019. **15**(1): p. 146-155.

72. Richart, R.M. and B.A. Barron, *A follow-up study of patients with cervical dysplasia.* American Journal of Obstetrics and Gynecology, 1969. **105**(3): p. 386-393.

73. Schlecht, N.F., et al., *Human papillomavirus infection and time to progression and regression of cervical intraepithelial neoplasia.* Journal of the National Cancer Institute, 2003. **95**(17): p. 1336-1343.

74. Naucler, P., et al., *Human papillomavirus and Papanicolaou tests to screen for cervical cancer.* New England Journal of Medicine, 2007. **357**(16): p. 1589-1597.

75. Cuzick, J., et al., *Overview of the European and North American studies on HPV testing in primary cervical cancer screening.* International journal of cancer, 2006. **119**(5): p. 1095-1101.

76. Hirth, J.M., et al., *Completion of the human papillomavirus vaccine series among insured females between 2006 and 2009.* Cancer, 2012. **118**(22): p. 5623-5629.

77. Kester, L.M., et al., *A national study of HPV vaccination of adolescent girls: rates, predictors, and reasons for non-vaccination.* Maternal and child health journal, 2013. **17**: p. 879-885.

78. Choma, M.A., et al., *Sensitivity advantage of swept source and Fourier domain optical coherence tomography.* Optics express, 2003. **11**(18): p. 2183-2189.

79. Leitgeb, R., C. Hitzenberger, and A.F. Fercher, *Performance of fourier domain vs. time domain optical coherence tomography.* Optics express, 2003. **11**(8): p. 889-894.

80. De Boer, J.F., et al., *Improved signal-to-noise ratio in spectral-domain compared with time-domain optical coherence tomography.* Optics letters, 2003. **28**(21): p. 2067-2069.

81. Fercher, A.F., et al., *Numerical dispersion compensation for partial coherence interferometry and optical coherence tomography.* Optics express, 2001. **9**(12): p. 610-615.

82. Wojtkowski, M., et al., *Ultrahigh-resolution, high-speed, Fourier domain optical coherence tomography and methods for dispersion compensation.* Optics express, 2004. **12**(11): p. 2404-2422.

83. Smith, E.D., A.V. Zvyagin, and D.D. Sampson, *Real-time dispersion compensation in scanning interferometry.* Optics Letters, 2002. **27**(22): p. 1998-2000.

84. Izatt, J.A. and M.A. Choma, *Theory of optical coherence tomography.* Optical Coherence Tomography: Technology and Applications, 2008: p. 47-72.

85. Evans, J.A., et al., *Optical coherence tomography to identify intramucosal carcinoma and high-grade dysplasia in Barrett's esophagus.* Clinical Gastroenterology and Hepatology, 2006. **4**(1): p. 38-43.

86. Evans, J.A., et al., *Identifying intestinal metaplasia at the squamocolumnar junction by using optical coherence tomography.* Gastrointestinal endoscopy, 2007. **65**(1): p. 50-56.

87. Qi, X., et al., *Image analysis for classification of dysplasia in Barrett's esophagus using endoscopic optical coherence tomography.* Biomedical optics express, 2010. **1**(3): p. 825-847.

88. Lee, H.-C., et al., *Endoscopic optical coherence tomography angiography microvascular features associated with dysplasia in Barrett's esophagus (with video).* Gastrointestinal endoscopy, 2017. **86**(3): p. 476-484. e3.

89. Ahsen, O.O., et al., *Assessment of Barrett's esophagus and dysplasia with ultrahigh-speed volumetric en face and cross-sectional optical coherence tomography.* Endoscopy, 2019. **51**(04): p. 355-359.

90. Giacomelli, M.G., et al., *Application of the T-matrix method to determine the structure of spheroidal cell nuclei with angle-resolved light scattering.* Optics letters, 2008. **33**(21): p. 2452-2454.

91. Chalut, K.J., et al., *Label-free, high-throughput measurements of dynamic changes in cell nuclei using angle-resolved low coherence interferometry.* Biophysical Journal, 2008. **94**(12): p. 4948-4956.

92. Terry, N.G., et al., *Detection of dysplasia in Barrett's esophagus with in vivo depth-resolved nuclear morphology measurements.* Gastroenterology, 2011. **140**(1): p. 42-50.

93. Terry, N., et al., *Detection of intestinal dysplasia using angle-resolved low coherence interferometry.* Journal of biomedical optics, 2011. **16**(10): p. 106002-106002-6.

94. Kim, R., et al., *Quantitative endoscopy: precise computerized measurement of metaplastic epithelial surface area in Barrett's esophagus.* Gastroenterology, 1995. **108**(2): p. 360-366.

95. Lin, B., et al., *Establishment of rules for interpreting ultraviolet autofluorescence microscopy images for noninvasive detection of Barrett's esophagus and dysplasia.* Journal of Biomedical Optics, 2012. **17**(1): p. 016013-016013.

96. Pal, R., et al., *Spectroscopic characterization of oral epithelial dysplasia and squamous cell carcinoma using multiphoton autofluorescence micro-spectroscopy.* Lasers in surgery and medicine, 2017. **49**(9): p. 866-873.

97. Nordstrom, R.J., et al., *Identification of cervical intraepithelial neoplasia (CIN) using UV-excited fluorescence and diffuse-reflectance tissue spectroscopy.* Lasers in Surgery and Medicine: The Official Journal of the American Society for Laser Medicine and Surgery, 2001. **29**(2): p. 118-127.

98. Ramanujam, N., et al., *Fluorescence spectroscopy: a diagnostic tool for cervical intraepithelial neoplasia (CIN).* Gynecologic oncology, 1994. **52**(1): p. 31-38.

99. Georgakoudi, I. and M.S. Feld, *The combined use of fluorescence, reflectance, and light-scattering spectroscopy for evaluating dysplasia in Barrett's esophagus.* Gastrointestinal Endoscopy Clinics, 2004. **14**(3): p. 519-537.

100. Redden Weber, C., et al., *Model-based analysis of reflectance and fluorescence spectra for in vivo detection of cervical dysplasia and cancer.* Journal of Biomedical Optics, 2008. **13**(6): p. 064016-064016-10.

101. Kanter, E.M., et al., *Application of Raman spectroscopy for cervical dysplasia diagnosis.* Journal of biophotonics, 2009. **2**(1-2): p. 81-90.

102. Mo, J., et al., *High wavenumber Raman spectroscopy for in vivo detection of cervical dysplasia.* Analytical chemistry, 2009. **81**(21): p. 8908-8915.

103. Teh, S., et al., *Diagnostic potential of near-infrared Raman spectroscopy in the stomach: differentiating dysplasia from normal tissue.* British journal of cancer, 2008. **98**(2): p. 457-465.

104. Chang, S.K., et al., *Combined reflectance and fluorescence spectroscopy for in vivo detection of cervical pre-cancer.* Journal of biomedical optics, 2005. **10**(2): p. 024031-024031-11.

105. Bergholt, M.S., et al., *Fiberoptic confocal raman spectroscopy for real-time in vivo diagnosis of dysplasia in Barrett's esophagus.* Gastroenterology, 2014. **146**(1): p. 27-32.

106. Almond, L.M., et al., *Endoscopic Raman spectroscopy enables objective diagnosis of dysplasia in Barrett's esophagus.* Gastrointestinal endoscopy, 2014. **79**(1): p. 37-45.

107. Mourant, J.R., et al., *Spectroscopic diagnosis of bladder cancer with elastic light scattering.* Lasers in surgery and medicine, 1995. **17**(4): p. 350-357.

108. Lovat, L. and S. Bown, *Elastic scattering spectroscopy for detection of dysplasia in Barrett's esophagus.* Gastrointestinal Endoscopy Clinics, 2004. **14**(3): p. 507-517.

109. Dhar, A., et al., *Elastic scattering spectroscopy for the diagnosis of colonic lesions: initial results of a novel optical biopsy technique.* Gastrointestinal endoscopy, 2006. **63**(2): p. 257-261.

110. Siegel, M.P., et al., *Assessment of blood supply in superficial tissue by polarization-gated elastic light-scattering spectroscopy.* Applied optics, 2006. **45**(2): p. 335-342.

111. Zhang, L., et al., *Light scattering spectroscopy identifies the malignant potential of pancreatic cysts during endoscopy.* Nature biomedical engineering, 2017. **1**(4): p. 0040.

112. Qiu, L., et al., *Multispectral scanning during endoscopy guides biopsy of dysplasia in Barrett's esophagus.* Nature medicine, 2010. **16**(5): p. 603-606.

113. Spliethoff, J.W., et al., *Improved identification of peripheral lung tumors by using diffuse reflectance and fluorescence spectroscopy.* Lung cancer, 2013. **80**(2): p. 165-171.

114. Shirkavand, A., et al., *Detection of melanoma skin cancer by elastic scattering spectra: a proposed classification method.* Iranian Journal of Medical Physics, 2017. **14**(3): p. 162-166.

115. Bigio, I.J., et al., *Diagnosis of breast cancer using elastic-scattering spectroscopy: preliminary clinical results.* Journal of biomedical optics, 2000. **5**(2): p. 221-228.

116. Grillone, G.A., et al., *The color of cancer: margin guidance for oral cancer resection using elastic scattering spectroscopy.* The Laryngoscope, 2017. **127**: p. S1-S9.

117. Carlson, K., et al., *Confocal microscopy: Imaging cervical precancerous lesions.* Gynecologic oncology, 2005. **99**(3): p. S84-S88.

118. Collier, T., et al., *Near real-time confocal microscopy of amelanotic tissue: detection of dysplasia in ex vivo cervical tissue.* Academic radiology, 2002. **9**(5): p. 504-512.

119. Tan, J., et al., *Detection of cervical intraepithelial neoplasia in vivo using confocal endomicroscopy.* BJOG: An International Journal of Obstetrics & Gynaecology, 2009. **116**(12): p. 1663-1670.

120. Shin, D., et al., *Quantitative analysis of high-resolution microendoscopic images for diagnosis of neoplasia in patients with Barrett's esophagus.* Gastrointestinal endoscopy, 2016. **83**(1): p. 107-114.

121. Grant, B.D., et al., *High-resolution microendoscopy: a point-of-care diagnostic for cervical dysplasia in low-resource settings.* European Journal of Cancer Prevention, 2017. **26**(1): p. 63-70.

122. Pierce, M.C., et al., *A Pilot Study of Low-Cost, High-Resolution Microendoscopy as a Tool for Identifying Women with Cervical PrecancerOptical Imaging for Detection of Cervical Precancer.* Cancer prevention research, 2012. **5**(11): p. 1273-1279.

123. Quinn, M.K., et al., *High-resolution microendoscopy for the detection of cervical neoplasia in low-resource settings.* 2012.

124. Hulst, H.C. and H.C. van de Hulst, *Light scattering by small particles*. 1981: Courier Corporation.

125. Zhang, H., et al. *In vivo detection of esophageal dysplasia using a/LCI light scattering with OCT image guidance*. in *Biomedical Applications of Light Scattering XII*. 2022. SPIE.

126. Steelman, Z.A., et al. *Progress in angle-resolved low-coherence interferometry for real-time detection of epithelial dysplasia (Conference Presentation)*. in *Biomedical Applications of Light Scattering X*. 2020. SPIE.

127. Steelman, Z.A., et al., *Scanning system for angle-resolved low-coherence interferometry.* Optics letters, 2017. **42**(22): p. 4581-4584.

128. Wax, A., et al., *In situ detection of neoplastic transformation and chemopreventive effects in rat esophagus epithelium using angle-resolved low-coherence interferometry.* Cancer research, 2003. **63**(13): p. 3556-3559.

129. Song, G., et al., *Spatial scanning of a sample with two-dimensional angle-resolved low-coherence interferometry for analysis of anisotropic scatterers.* Biomedical Optics Express, 2020. **11**(8): p. 4419-4430.

130. Čižmár, T. and K. Dholakia, *Shaping the light transmission through a multimode optical fibre: complex transformation analysis and applications in biophotonics.* Optics Express, 2011. **19**(20): p. 18871-18884.

131. Choi, Y., et al., *Scanner-free and wide-field endoscopic imaging by using a single multimode optical fiber.* Physical review letters, 2012. **109**(20): p. 203901.

132. Caramazza, P., et al., *Transmission of natural scene images through a multimode fibre.* Nature communications, 2019. **10**(1): p. 2029.

133. Resisi, S., S.M. Popoff, and Y. Bromberg, *Image transmission through a dynamically perturbed multimode fiber by deep learning.* Laser & Photonics Reviews, 2021. **15**(10): p. 2000553.

134. Rahmani, B., et al., *Multimode optical fiber transmission with a deep learning network.* Light: science & applications, 2018. **7**(1): p. 69.

135. Borhani, N., et al., *Learning to see through multimode fibers.* Optica, 2018. **5**(8): p. 960-966.

136. Valley, G.C., G.A. Sefler, and T.J. Shaw, *Multimode waveguide speckle patterns for compressive sensing.* Optics letters, 2016. **41**(11): p. 2529-2532.

137. Amitonova, L.V. and J.F. De Boer, *Compressive imaging through a multimode fiber.* Optics letters, 2018. **43**(21): p. 5427-5430.

138. French, R. and S. Gigan, *Snapshot fiber spectral imaging using speckle correlations and compressive sensing.* Optics express, 2018. **26**(24): p. 32302-32316.

139. Zhang, H., Z.A. Steelman, and A. Wax. *Determination of Particle Size from Reconstructed Angular Backscattering Through a Single Multimode Fiber*. in *Optical Tomography and Spectroscopy*. 2020. Optica Publishing Group.

140. Plöschner, M., T. Tyc, and T. Čižmár, *Seeing through chaos in multimode fibres.* Nature Photonics, 2015. **9**(8): p. 529-535.

141. Ju, Z., et al., *Simultaneous illumination and imaging based on a single multimode fiber.* Optics Express, 2022. **30**(9): p. 15596-15606.

142. Lan, M., et al., *Averaging speckle patterns to improve the robustness of compressive multimode fiber imaging against fiber bend.* Optics Express, 2020. **28**(9): p. 13662-13669.

143. Fan, P., T. Zhao, and L. Su, *Deep learning the high variability and randomness inside multimode fibers.* Optics express, 2019. **27**(15): p. 20241-20258.

144. Wang, P. and J. Di, *Deep learning-based object classification through multimode fiber via a CNN-architecture SpeckleNet.* Applied optics, 2018. **57**(28): p. 8258-8263.

145. Sinclair, D., *Light scattering by spherical particles.* JOSA, 1947. **37**(6): p. 475-480.

146. Zambrana-Puyalto, X., *Control and characterization of nano-structures with the symmetries of light.* arXiv preprint arXiv:1502.01648, 2015.

147. Wan, W.Y., et al., *Integration of light scattering with machine learning for label free cell detection.* Biomedical Optics Express, 2021. **12**(6): p. 3512-3529.

148. Sun, J., et al., *Deep learning-based light scattering microfluidic cytometry for label-free acute lymphocytic leukemia classification.* Biomedical Optics Express, 2020. **11**(11): p. 6674-6686.

149. Kingma, D.P. and J. Ba, *Adam: A method for stochastic optimization.* arXiv preprint arXiv:1412.6980, 2014.

150. Damania, D., et al., *Insights into the field carcinogenesis of ovarian cancer based on the nanocytology of endocervical and endometrial epithelial cells.* International journal of cancer, 2013. **133**(5): p. 1143-1152.

151. Robles, F.E., et al., *Detection of early colorectal cancer development in the azoxymethane rat carcinogenesis model with Fourier domain low coherence interferometry.* Biomedical optics express, 2010. **1**(2): p. 736-745.

152. Chu, K.K., et al., *Esophageal OCT Imaging Using a Paddle Probe Externally Attached to Endoscope.* Digestive Diseases and Sciences, 2022. **67**(10): p. 4805-4812.

153. Kimura, B.J., et al., *Distortion of intravascular ultrasound images because of nonuniform angular velocity of mechanical-type transducers.* American heart journal, 1996. **132**(2): p. 328-336.

154. Lee, J., et al., *Esophageal diameter is decreased in some patients with eosinophilic esophagitis and might increase with topical corticosteroid therapy.* Clinical gastroenterology and hepatology, 2012. **10**(5): p. 481-486.

155. Yang, Z., et al., *Connectivity-based deep learning approach for segmentation of the epithelium in in vivo human esophageal OCT images.* Biomedical optics express, 2021. **12**(10): p. 6326-6340.

156. Gu, Z., et al., *Ce-net: Context encoder network for 2d medical image segmentation.* IEEE transactions on medical imaging, 2019. **38**(10): p. 2281-2292.

157. Kendall, B.J., et al., *The risk of Barrett's esophagus associated with abdominal obesity in males and females.* International journal of cancer, 2013. **132**(9): p. 2192-2199.

158. Chalut, K.J., et al., *In situ assessment of intraepithelial neoplasia in hamster trachea epithelium using angle-resolved low-coherence interferometry.* Cancer Epidemiology Biomarkers & Prevention, 2007. **16**(2): p. 223-227.

Biography

Haoran Zhang graduated from Fudan University in 2017 with a B.S. in Physics with Honors. He earned a Master of Science degree in Biomedical Engineering from Duke University in May 2019. He then continued his Ph.D. studies in Biomedical Engineering at Duke University under the advisement of Dr. Adam Wax. At Duke, Haoran's primary project is the development of angle-resolved low-coherence interferometry (a/LCI) for early cancer detection, and have conducted multiple research projects for advancing this optical technology. In 2021, Haoran was awarded the John T. Chambers Fellowship in the Fitzpatrick Institute for Photonics, and the BME Fellowship Award in Biomedical Engineering.

He will graduate in Summer 2023, with a Doctor of Philosophy in Biomedical Engineering, and will be joining KLA as an Optical Research Scientist in Aug 2023.